BSD-TR-66-355

7741-3-Q

Copy___

~~SECRET~~

CONF-4

THE UNIVERSITY OF MICHIGAN

COLLEGE OF ENGINEERING

DEPARTMENT OF ELECTRICAL ENGINEERING

Radiation Laboratory

Investigation of Re-Entry Vehicle Surface Fields (U)

Quarterly Report No. 3
18 June - 18 September 1966

by

R. F. GOODRICH, B. A. HARRISON, E. F. KNOTT,
T. B. A. SENIOR and V. H. WESTON

September 1966

7741-3-Q = RL-2163

Contract AF04(694)-834

<u>Distribution Statement:</u> In addition to security requirements which apply to this document and must be met, this document is subject to special export controls and each transmittal to foreign governments or foreign nationals may be made only with prior approval of Ballistic Systems Division (BSYDF) Norton AFB, Calif. 92409.

Contract With:
Ballistic Systems Division
Deputy for Ballistic Missile Re-entry Systems
Air Force Systems Command
Norton AFB, California

Administered through:

CONF-4

OFFICE OF RESEARCH ADMINISTRATION • ANN ARBOR

~~GROUP 4~~
~~Downgraded at 3-year intervals;~~
~~declassified after 12 years.~~

~~SECRET~~

~~This document contains information affecting the National Defense of the United States within the meaning of the Espionage Laws, Title 18 U.S.C., Sections 793 and 794. Its transmission or the revelation of its contents in any manner to an unauthorized person is prohibited by law.~~

BSD-TR-66 -355

Investigation of Re-entry Vehicle Surface Fields (U)

Quarterly Report No. 3

18 June 1966 - 18 September 1966

AF 04(694)-834

by

R. F. Goodrich, B. A. Harrison, E. F. Knott, T. B. A. Senior and V. H. Weston

September 1966

Prepared for
BALLISTIC SYSTEMS DIVISION
DEPUTY FOR BALLISTIC MISSILE RE-ENTRY SYSTEMS
AIR FORCE SYSTEMS COMMAND
NORTON AFB , CALIFORNIA

In addition to security requirements which apply to this document and must be met, this document is subject to special export controls and each transmittal to foreign governments or foreign nationals may be made only with prior approval of BSD (BSYDF), Norton AFB, California 92409.

FOREWORD

This report was prepared by the Radiation Laboratory of the Department of Electrical Engineering of The University of Michigan under the direction of Dr. Raymond F. Goodrich, Principal Investigator and Burton A. Harrison, Contract Manager. The work was performed under Contract AF04(694)-834, "Investigation of Re-entry Vehicle Surface Fields (SURF)". The work was administered under the direction of the Air Force Ballistic Systems Division, Norton Air Force Base, California 92409, by Major A. Aharonian BSYDF and was monitored by Mr. Henry J. Katzman of the Aerospace Corporation.

The studies presented herein cover the period 18 June through 18 September 1966.

The publication of this report does not constitute Air Force approval of the report's findings or conclusions. It is published only for the exchange and stimulation of ideas.

BSD Approving Authority

William J. Schlerf BSYDR
Contracting Officer

MISSING
PAGE

TABLE OF CONTENTS

MISSING
PAGE

ABSTRACT

(Secret)

This is the Third Quarterly Report on Contract AF04(694)-834 and covers the period 18 June to 18 September 1966. Progress on the SURF program is discussed. This program has as its objective the determination of the radar cross section of cone-sphere shaped re-entry vehicles by means of a study of the fields induced on the surface of vehicle models by incident radar energy. During this reporting period, surface field measurements were made on metallic cone-spheres, cone-spheres covered with various coating materials and perturbed cone-sphere shapes. The perturbations included a study of the effect of a nose-tip antenna, a concave rear termination similar to the Mark 12 re-entry vehicle and representations of flush mounted slot antennas. Radar backscattering measurements were made of models with the nose-tip antenna and the concave termination. The investigation of the radar cross section of the re-entry vehicle in the plasma environment concentrated on determining which cases would be of practical importance so that they might be analyzed in depth.

INTRODUCTION

The SURF program is aimed at providing a sound basis for computing the radar cross section of metallic and coated re-entry bodies which are cone-sphere-like shapes and at determining the effect on radar cross section of the plasma re-entry environment and of perturbations such as slot antennas and non-spherical terminations at the rear of the vehicle. An understanding of the basic physics of the scattering of radar energy by these metallic bodies and the materials with which they are coated is the only effective and cost-effective means of designing the best re-entry vehicles and realistic decoy representations. Where this understanding does not exist, a guessing method or a trial-and-error approach with its costly delays and uncertainties is the only alternative.

At this phase of the investigation, a good theoretical foundation has been worked out for computing the radar cross section of metallic cone-spheres. It has been developed with the assistance of surface field and backscatter experiments and a body of prior work by many investigators and is confirmed by comparison with such measurements as are available for the cross section of metallic models. This is particularly true for the case of nose-on incidence. The investigation increases in difficulty as the cases of oblique incidence, the effect of coatings, the effect of antennas and other perturbations, the effect of plasma environment and the effect of combinations of these parameters is attacked. However, the value of the results for these cases also increases in importance. These are areas of investigation in which little work had been done prior to the SURF program.

This Quarterly Report summarizes the results of three months of investigation (18 June to 18 September 1966) undertaken at the Radiation Laboratory for the Ballistic Systems Division. The work reported in the report is of experiments and analysis in an intermediate stage of progress, rather than of completed studies.

TASK 2.0: EXPERIMENTAL INVESTIGATIONS

"I got heartaches by the numbers,
Troubles by the score. . . . "
Country Ballad

In this second of this quarterly, we shall describe the experimental work 'by the numbers', which is to say, Task by Task.

Experimental work has continued approximately on schedule and emphasis has been placed upon learning more about absorbers when applied to re-entry shapes. The surface distributions of magnetic and electric fields have been explored for bodies wrapped in absorbers and it appears that an impedance boundary condition can be approximated for the more lossy materials. A limited number of backscatter measurements have been performed. Our stock of uncoated models has been augmented with a nose-tip antenna simulation model and with models having indented terminations; surface field data and backscatter patterns have been obtained for these objects. The effects of perturbations in both the illuminated and shadowed portions of a cone sphere have been measured.

Below, we present a detailed account of the experimental work. The data presented is representative of typical results and is chosen for illustrative reasons only.

2.1.1: Continuation of Measurements and Extension to Coated Bodies

This task is concerned with the measurement of surface fields upon conducting cone-sphere models enveloped in a layer of absorbing material or dielectric. The measured surface field quantities are shown in Fig. 2-1. They were obtained along surface trajectories lying in the plane containing the body axis and the incident electric field or in the plane containing the body axis and the incident magnetic field. The components measured were the circumferential fields H_ϕ and E_ϕ, each measured along a different trajectory, and the longitudinal field, E_s, measured along the same trajectory used for H_ϕ. Not all three components were measured for all the coatings because we either encountered experimental difficulties or because there was little theoretical interest in them. Generally, E_s was obtained only for the materials which had substantial losses: a summary of the measurements appears in Table II-1.

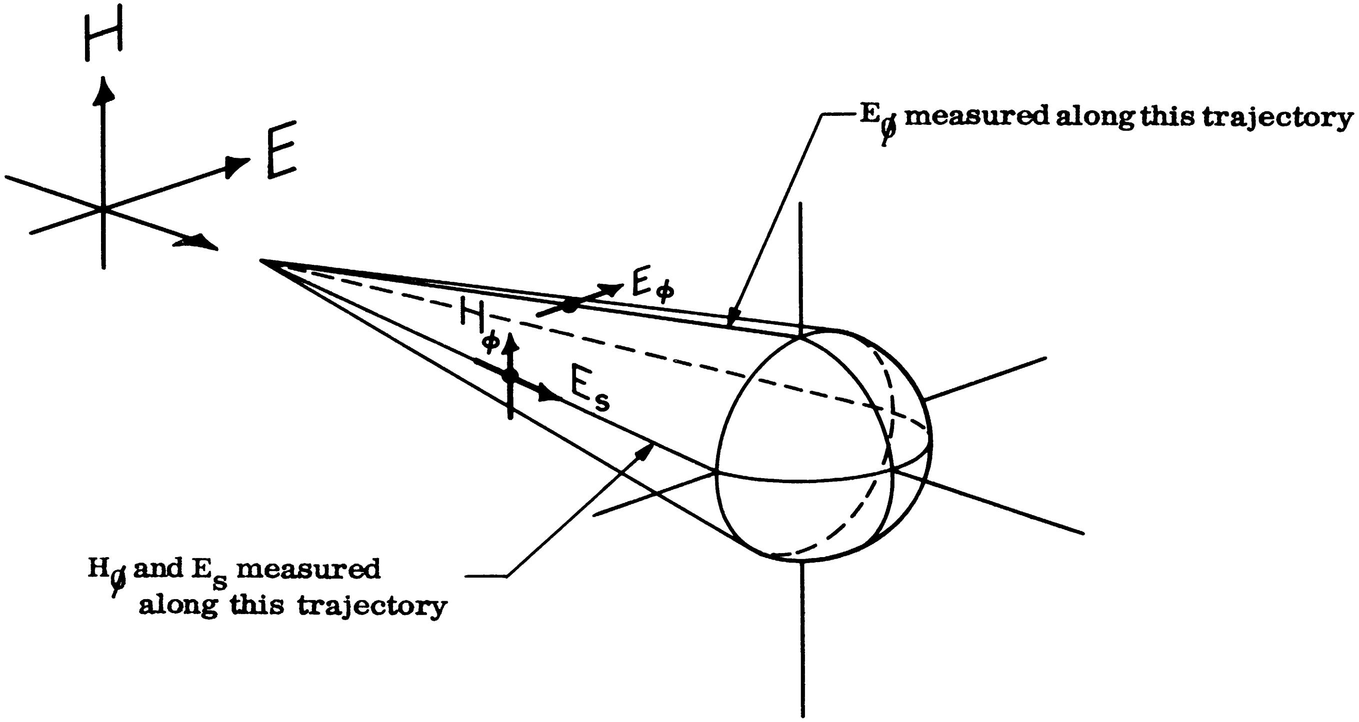

FIG. 2-1: BOTH ELECTRIC AND MAGNETIC FIELDS WERE MEASURED ALONG PRINCIPAL TRAJECTORIES

TABLE II-1: EIGHT MATERIALS STUDIED UNDER A VARIETY OF CONDITIONS

Base Dia. (inches)	Coating Thickness (inches)	Coating Material	Cone Half-angle (degrees)	ka	Quantity Measured
2.024	0.375	Lucite	7 1/2	1.6	H_ϕ, E_ϕ
2.024	0.375	Lucite	10	1.6	H_ϕ, E_ϕ
2.024	0.375	Lucite	11 1/4	1.6	H_ϕ, E_ϕ
3.852	0.375	Lucite	12 1/2	3.0	H_ϕ, E_ϕ
3.852	0.375	"3.01"	12 1/2	3.0	H_ϕ, E_ϕ
3.000	0.375	Air	7 1/2	1.6	H_ϕ, E_ϕ
3.000	0.294	LS-22	7 1/2	1.0, 3.0, 5.0	H_ϕ, E_ϕ
4.420	0.305	LS-22	7 1/2	8.0	H_ϕ, E_ϕ
4.420	0.290	LS-26	7 1/2	8.0	H_ϕ, E_ϕ
3.000	0.280	LS-26	7 1/2	1.0, 3.0, 8.0	H_ϕ, E_ϕ
3.000	0.280	LS-24	7 1/2	1.0, 3.0, 5.0	H_ϕ, E_ϕ, E_s
4.420	0.280	LS-24	7 1/2	8.0	H_ϕ, E_ϕ, E_s
4.420	0.062	RS-X	7 1/2	1.0, 3.0, 5.0, 8.0	H_ϕ, E_ϕ, E_s
3.000	0.374	Eccosorb CR	7 1/2	1.0, 3.0, 5.0	H_ϕ, E_ϕ, E_s
3.000	0.374	Eccosorb CR	7 1/2	8.0	H_ϕ

The absorber coatings, whose properties are briefly discussed in Task 2.1.6, were sewn into the conducting models with high strength dacron cord. The coatings were applied in this fashion because the adhesives available would not hold the seams together and they required much more time than the sewing process. The effects of the seams are clearly present in the high frequency measurement runs, but are not felt to be deleterious to data analysis. One coating, the Eccosorb CR material, was cast onto a basic cone-sphere and was then machined on a lathe to a uniform thickness and thus has no visible seams. There are, however, interfaces in this particular coating because the material was applied in several batches and we cannot assume the properties of one batch are identical to that of another. But the effects of these interfaces, as determined from several measurements of surface fields, are negligible.

Photographs of three of the coated objects are shown in Figs. 2-2 through 2-4 which illustrate the physical appearances of the coatings. All the LS series of absorbers look alike and it can be observed from Fig. 2-2 that the tip is not sharp. This is because the coating was originally a sheet of finite thickness and cannot be wrapped about a surface whose radius of curvature vanishes as it does near a perfect cone tip. The RS-X material in Fig. 2-3 is much thinner than the LS series but the tip coverage is still not perfect. There is a spiral seam about 1/3 the body length from the tip and seams appear on the spherical base. Inspection of Figure 2-4 confirms that the Eccosorb CR coating is by far the most uniform of the three models shown. A scale marked on transparent tape is fastened to each model; these are very thin dielectric ribbons and have no measurable effect upon the observed surface distributions.

2.1.2: Frequency Variation

The study of surface fields on objects whose electrical sizes encompass "Rayleigh physical optics, and resonance regions" is carried out under this Task. Emphasis is on nose-on incidence. The resonance region has been covered and the measurements have been extended to a ka value of 8.0 into the physical optics region. Oblique

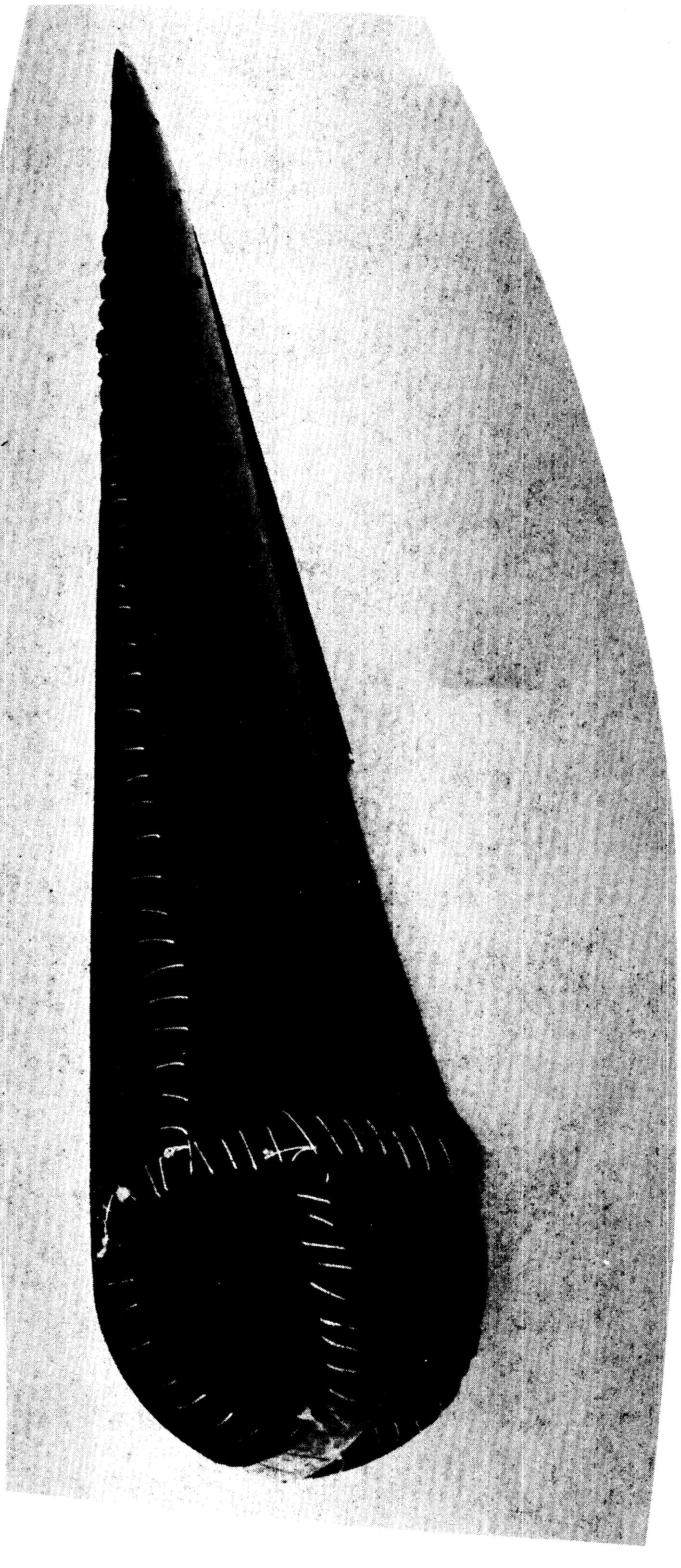

FIG. 2-2: COATING LS-24 WRAPPED ABOUT 3.00" BASE DIAMETER, 7 1/2° HALF ANGLE CONE-SPHERE.

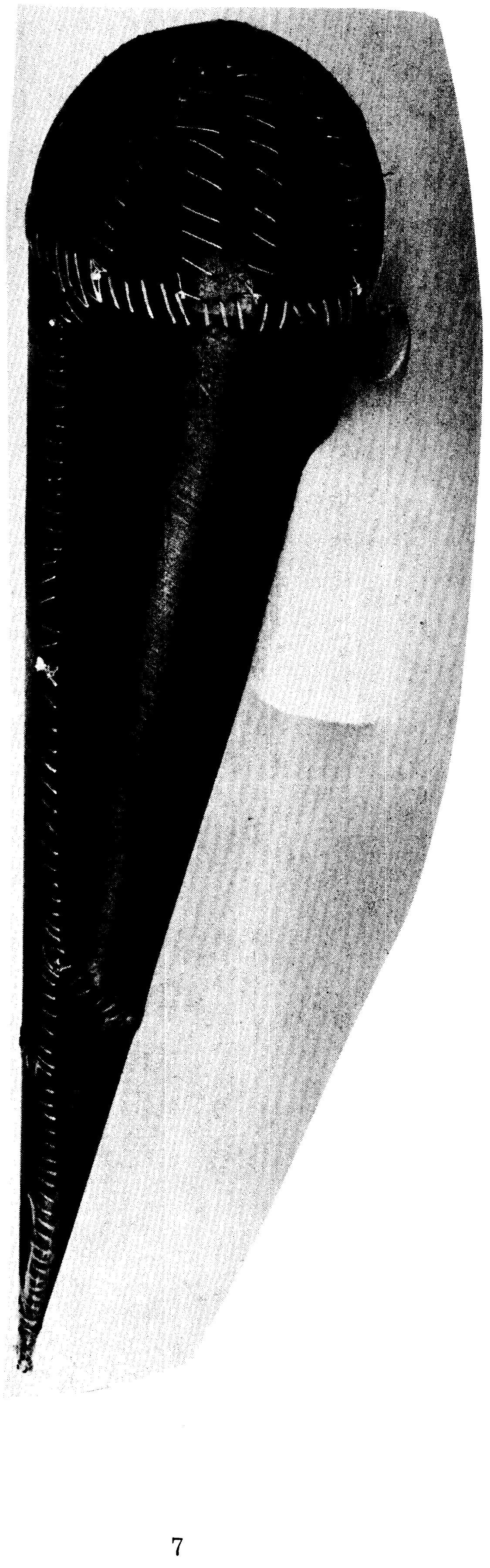

FIG. 2-3: RS-X COATING COVERING 4.42" BASE DIAMETER, 7 1/2° HALF ANGLE CONE-SPHERE.

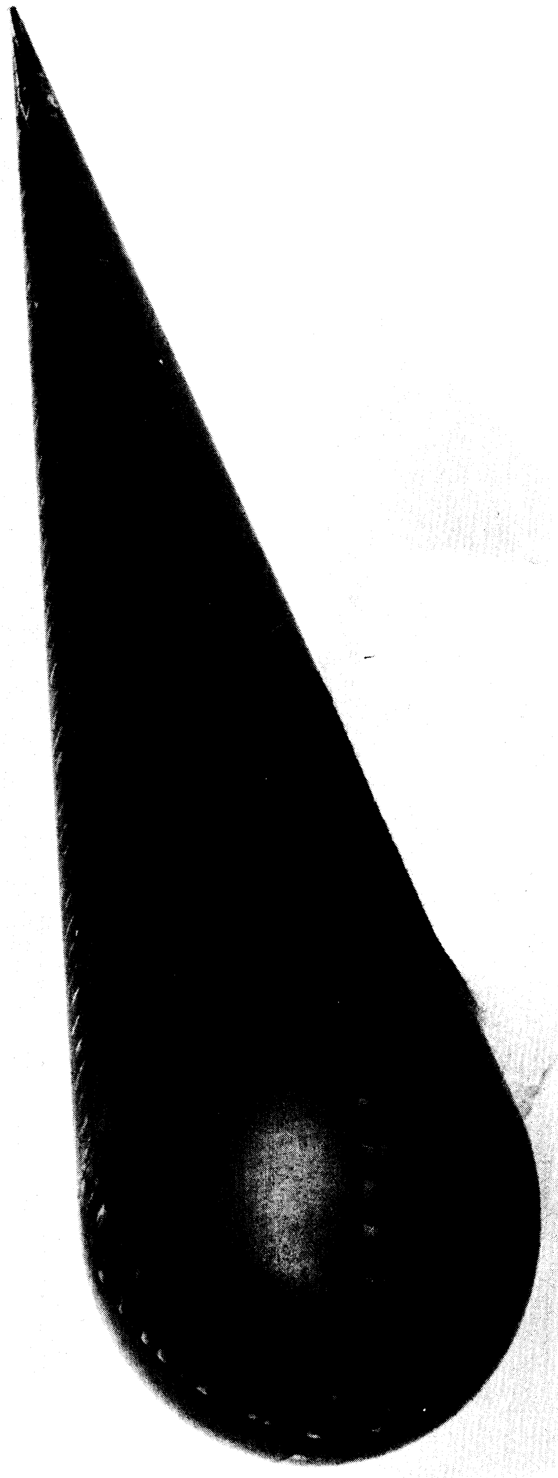

FIG. 2-4: ECCOSORB CR COATING CAST UPON 3.00" BASE DIAMETER, 7 1/2° HALF ANGLE CONE-SPHERE AND MACHINED TO UNIFORM THICKNESS.

incidence has not yet been examined for coated objects but will soon be initiated. Task 2.1.2 is approximately 80 per cent complete.

2.1.3: Body Parameter Effects

This task defines the ranges in nose-to-base radii ratio, cone angle, electrical size and the physical thickness of the coating material under investigation. Previous work has shown that the effect of finite nose radius is completely understood on the conducting object and although the present work with coatings is confined to sharp tips, a coated, blunted nose should likewise be straightforward. We therefore anticipate little or no need for measurements of coated blunt noses. The effect of cone angle in the perfectly conducting case is understood and we have confined our attention in the coated case to $7\frac{1}{2}^{\circ}$ half angle; a few measurements have been made for varying cone angle, but these have been for low loss coatings (c.f. Table II-1). The electrical sizes examined have been for $1.0 \leq ka \leq 8.0$ and the theory seems exact enough for $ka > 8.0$ that there has been no need for measurements for $8.0 < ka \leq 15.0$. The task is about 75 per cent complete.

2.1.4: Effect of Discontinuities

This task has been partially completed. One of the discontinuities studied is that of the cone-sphere join. The effect of the discontinuity due to a nose-tip antenna is described under Tasks 2.1.8 and 3.1.1. This task is about 85 per cent complete.

2.1.5: Shadow Boundary Effects

Indented base models have been acquired to carry out measurements under this task and under Task 2.1.10. The basic form of the base was presented in the Second Quarterly Report (page 23) and sketches of the entire models are presented approximately to scale in Fig. 2-5 of this report. Each of the three models shares a common front end, the conical part, and only the bases are different. The depth of

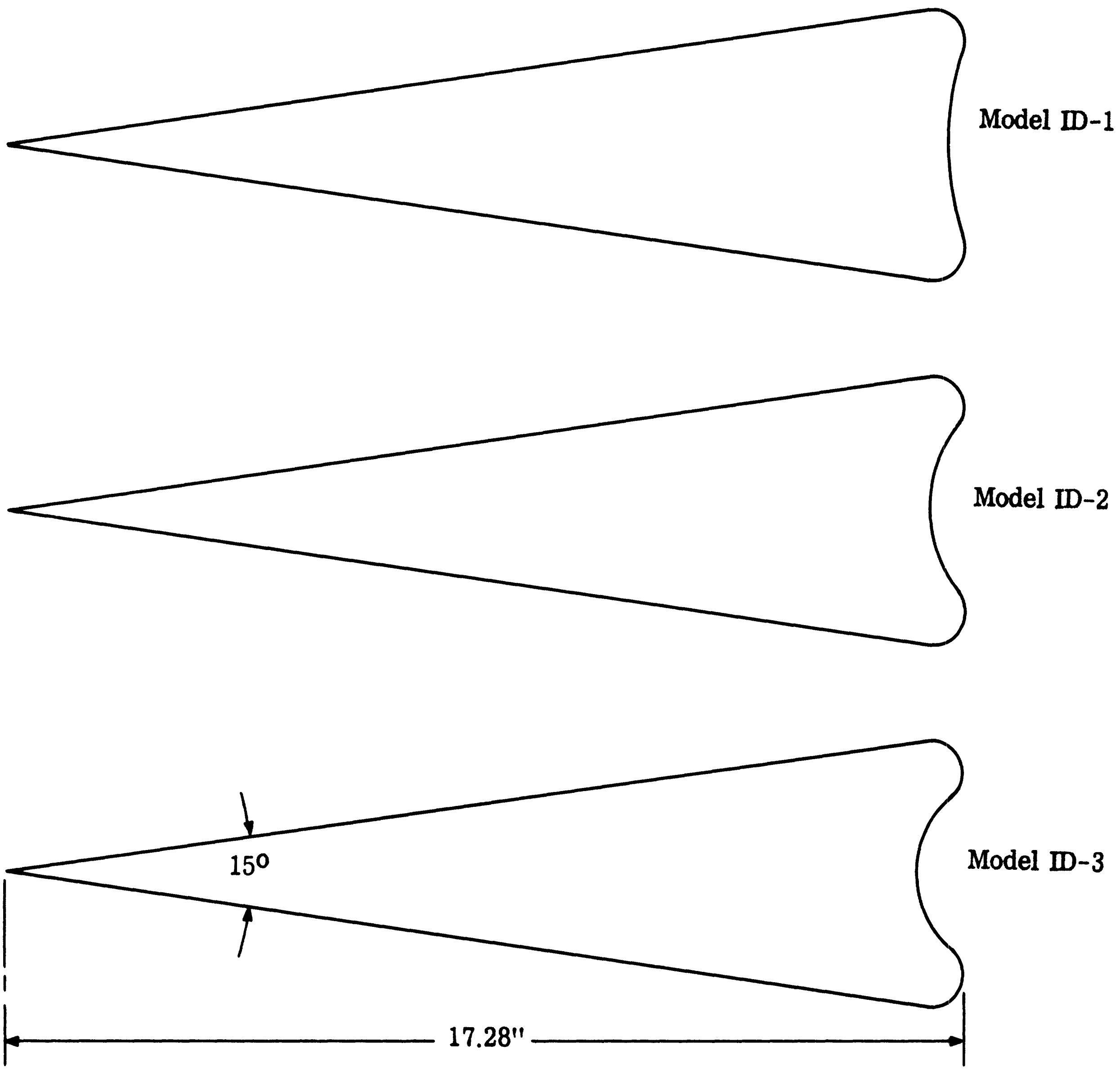

FIG. 2-5: THE THREE INDENTED BASE MODELS HAVE INDENTATION DEPTHS FROM MODEL TO MODEL WHICH VARY AS 1:2:3.

indentation among the three forms the ratios 1 : 2 : 3 , thus the indentation of Model ID-3 is three times that of ID-1.

The surface field H_ϕ has been probed on Models ID-1 and ID-2 for ka = 1.1, 3.0, 5.0 and 8.0 and some backscatter patterns have been obtained for Model ID-1. Because the magnetic probe must be bent or curved to reach into the indentation (Fig. 2-6), there is the increasing likelihood that the probe output contains an error voltage due to radial electric fields. This is because the increased horizontal portion of the probe lead is excited by the radial electric field and currents are induced on the load which find their way to the probe loop, and consequently induce voltages across the probe gap. Fortunately, these error voltages have phase differences of 180° from one side of the body to the other, and by virtue of the target symmetry, a data averaging process removes much of the error.

A typical plot of the surface field is displayed in Fig. 2-7. In this plot the conical portion of the data has been separated from the data taken around the base; the measured values of H_ϕ have been normalized with respect to the incident field intensity. On the forward portion of the objects the mean field intensity is approximately the same for both but there is a slight increase in the amplitude of the oscillations about this mean accompanied by a small shift in the period for the indented base model. The increased oscillation, of course, implies its radar cross section is greater than that of the cone sphere, in spite of a reduction of the intensity of the creeping wave around the base. The distance around the base of the indented model is less than that of a cone sphere and the data does not extend as far. The characteristic 'bright spot' at the rear dead center is some 5 db below that of the cone sphere and around the base the intensity falls off much faster.

The data is typical for indented terminations, but for the purposes of data analysis a different form of presentation is used. The normalized field intensities are deduced from the logarithmic values and are plotted as a function of distance in wavelengths from the tip. Measurements have been obtained for Models ID-1 and ID-2, but not ID-3. For this last model we anticipate some difficulty because of

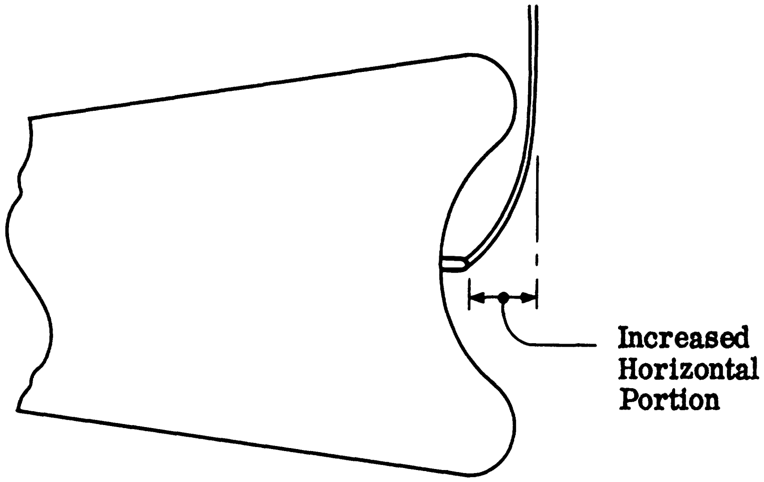

FIG. 2-6: A PROBE BENT TO SAMPLE FIELDS IN AN INDENTATION.

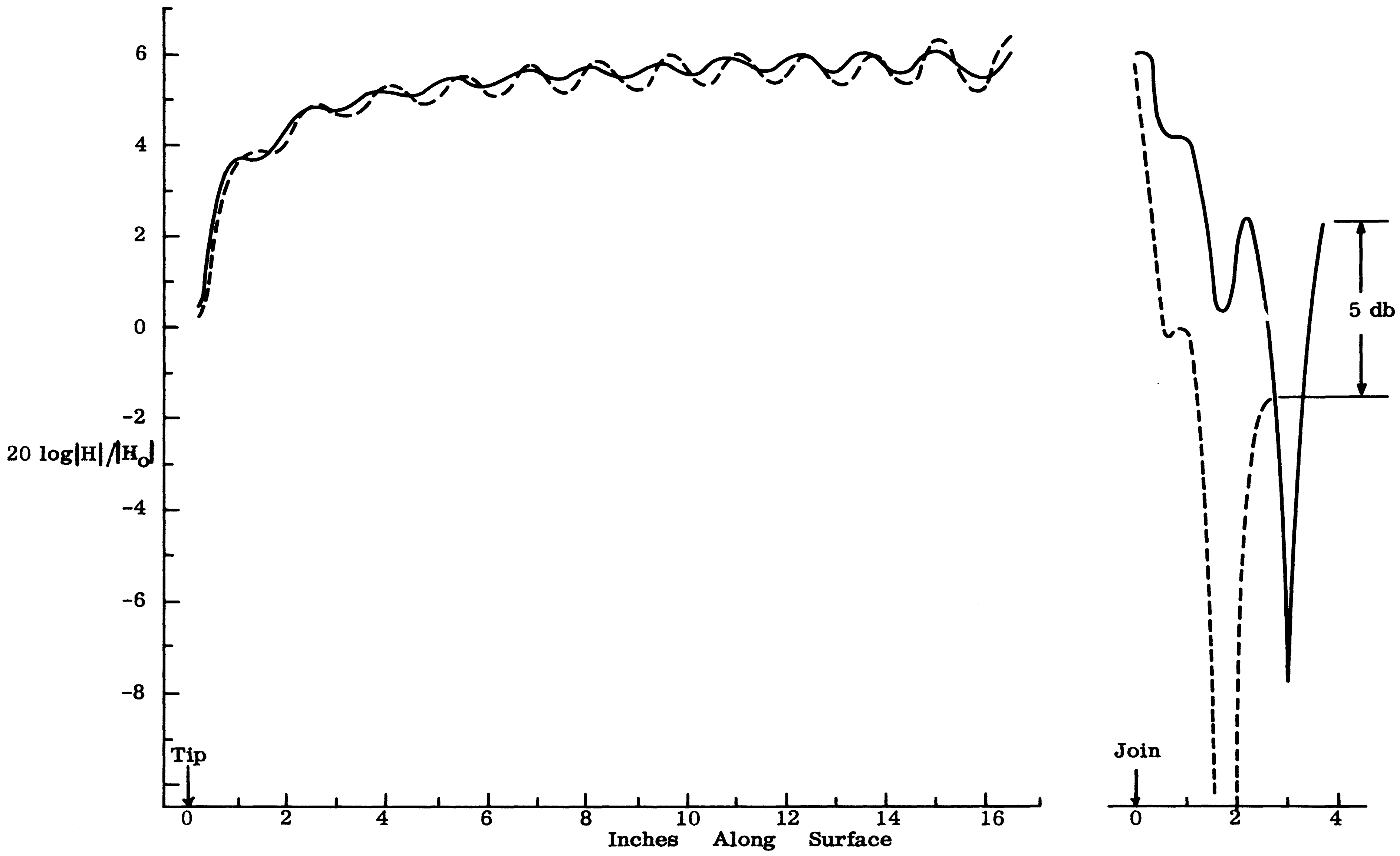

FIG. 2-7: COMPARISON OF SURFACE FIELD DATA OF A CONE-SPHERE (SOLID TRACE) WITH THAT OF INDENTED BASE MODEL ID-1 (DASHED TRACE) FOR ka = 5.0.

the great depth of indentation and the relatively long horizontal component the probe must have to reach into the depression.

In addition to surface field data, backscatter measurements have been made for Model ID-1. Representative ka values have been examined. The task is 75 per cent complete.

2.1.6: Study of Coating Materials

As reported in the Second Quarterly Report, we have evaluated absorbing materials by transmission line techniques instead of by free space scattering measurements of absorber-coated plates and cylinders, because more information is obtained about absorber properties from these kinds of data. The tentative values of μ_r, ϵ_r (relative to those of free space) listed in the previous report have now been finalized by the inclusion of data for the casting resin absorber, Eccosorb CR. The data are presented for convenience in Table II-2 of this report and it will be observed that some of the values show variations among otherwise identical samples. These we attribute to sample inhomogeneities and inherent limitations of the simple techniques we used. Nonetheless, as we shall later show, the data can be extremely useful in analysis of surface field measurements.

It should be noted that in the measurements we assumed the complex permittivities to have the form

$$\epsilon_r = \epsilon_r' - j\epsilon_r'' = |\epsilon_r| e^{-j\delta} , \qquad (2.1)$$

and similarly for the complex permeabilities. Therefore the loss tangents indicated in Table II-2 describe a number lying in the fourth quadrant of the complex plane when $\delta > 0$, or when $\tan\delta > 0$. By reason of conservation of energy this must be so, but we did obtain negative values in a few cases and these must be taken as representative of the typical measurement errors. Note that the discrepancies usually occur for small dielectric or small magnetic losses, which are difficult to determine accurately, while the substantial losses are always in the proper quadrant.

TABLE II-2: MEASURED ELECTROMAGNETIC PROPERTIES OF SELECTED SAMPLES.

Material and Number	2.5GHz				3.0 GHz				3.5 GHz			
	ϵ_r		μ_r		ϵ_r		μ_r		ϵ_r		μ_r	
	mag.	tanδ	mag.	tanδ	mag.	tanδ	mag.	tanδ	mag.	tanδ	mag.	tanδ
LS-22 I	3.1	1.1	1.0	.04	2.7	1.1	1.1	.03	2.3	.92	1.0	.06
LS-22 II	3.3	1.0	1.0	.05	3.2	1.1	1.0	.02	2.4	.92	1.1	.09
LS-22 III	3.0	1.05	1.0	0	2.4	.88	1.0	.12	2.2	.92	1.1	.02
LS-24 I	7.6	1.5	1.0	0	6.7	1.7	1.0	.04	6.1	.68	1.0	.36
LS-24 II	8.2	1.7	1.0	.05	6.9	1.5	1.0	1.0	6.4	1.4	1.0	.10
LS-24 III	7.8	1.7	1.0	.01	6.9	2.5	1.1	-.03	5.9	.84	.94	.09
LS-26 I	7.4	1.6	.97	.02	6.5	1.8	1.0	.04	5.4	1.5	1.0	.01
LS-26 II	8.0	1.7	1.0	.05	6.3	2.2	1.1	.03	5.7	.73	1.1	.07
LS-27 III	7.9	1.8	1.0	.02	6.8	2.5	1.2	-.02	5.4	1.2	1.0	.09
AN-72 I	5.7	1.0	.94	-.06	5.9	1.6	1.0	-.16	4.9	1.4	.95	-.18
AN-72 II	5.6	1.2	.94	-.09	4.9	1.5	1.0	-.12	4.2	1.1	.95	-.13
AN-72 III	5.6	1.0	.97	-.08	5.4	1.3	1.0	-.13	4.4	1.0	1.0	.10
AN-73 I	5.4	2.4	1.0	.27	4.2	5.9	1.2	-.36	3.5	2.3	1.1	-.35
AN-73 III	4.5	1.8	1.0	-.23	3.7	3.3	1.1	-.36	3.0	1.9	1.1	-.31
AN-73 IV	4.9	2.0	1.0	-.24	4.1	3.0	1.1	-.31	3.3	2.5	1.1	-.33
RS-S I	8.6	.01	1.8	.37	10.4	.08	2.4	.33	7.1	-.11	2.0	.58
RS-S II	8.7	.01	1.8	.39	9.2	1.4	1.8	-.55	6.9	-.06	2.1	.55
RS-S III	8.2	-.01	1.9	.38	9.1	0	1.7	.38	6.5	-.14	2.1	.64
RS-X I	8.3	.02	2.8	.33	8.9	.01	2.5	.36	8.3	.04	2.4	.40
RS-X II	8.3	..02	2.8	.32	8.6	.03	2.6	.38	7.8	.39	3.2	.29
RS-X III	8.4	.02	2.8	.33	8.8	.03	2.6	.01	7.7	.04	2.6	.39
Ferrite II	7.7	1.2	14.0	-.31	7.1	-.01	2.9	3.6	4.6	.05	3.4	2.1
Ferrite III	9.2	1.1	15.0	-.41	6.2	-.014	2.7	3.1	5.8	.08	2.6	5.6
Radite I	10.2	.004	3.4	.45	9.7	.08	3.4	.39	10.6	.02	2.9	.52
Radite II	11.5	-.04	3.2	.51	9.8	.04	3.1	.36	11.0	.11	3.1	.44
Radite III	10.5	.01	3.4	.44	9.4	.08	3.5	.39	10.4	.08	3.2	.46
CR I	11.7	.03	3.9	.49	12.5	.03	3.5	.53	11.2	0	3.7	.62
CR II	13.9	.03	3.9	.52	12.6	0	3.7	.59	12.6	-.02	3.7	.67
CR III	12.0	.04	3.9	.48	14.7	-.35	3.0	.40	11.0	0	3.9	.40

TABLE II-2: (continued)

Material and Number		4.0 GHz				4.5 GHz				5.0 GHz			
		ϵ_r		μ_r		ϵ_r		μ_r		ϵ_r		μ_r	
		mag.	tanδ	mag.	tanδ	mag.	tanδ	mag.	tanδ	mag.	tanδ	mag.	tanδ
LS-22	I	2.5	.75	.93	-.07	2.3	.78	.93	.09	2.0	.85	1.1	-.02
LS-22	II	2.7	1.0	.94	-.09	2.2	.75	1.0	.06	2.1	1.0	1.1	-.07
LS-22	III	2.4	.75	.93	.02	2.1	.63	1.0	.09	2.1	.80	1.0	-.002
LS-24	I	5.7	1.4	1.0	-.01	4.9	1.2	1.0	.04	4.7	2.1	1.2	-.08
LS-24	II	6.1	1.2	1.0	-.11	5.2	1.4	1.0	.01	5.6	1.7	1.2	-.01
LS-24	III	5.9	.68	1.6	.31	4.7	1.3	1.0	.004	4.8	2.0	1.2	-.05
LS-26	I	5.8	1.6	.90	-.12	3.7	1.3	1.3	-.17	4.4	2.2	1.3	-.12
LS-26	II	6.2	2.2	.92	-.16					4.8	1.9	1.2	-.06
LS-26	III	5.7	1.7	.90	-.11	3.9	1.2	1.2	-.12	4.5	2.0	1.3	-.11
AN-72	I	5.6	1.2	.82	-.24	4.4	1.6	.96		3.7	2.7	1.1	-.41
AN-72	II	5.0	1.2	.86	-.23	4.1	1.5	.83	-.22	3.5	2.8	1.1	-.36
AN-72	III	5.2	.83	.86	-.22	4.2	1.5	1.0	.27	3.9	1.8	1.0	-.34
AN-73	I	3.0	1.4	1.5	-.60	2.5	2.9	1.4	.43	2.0	2.6	1.8	-.34
AN-73	III	3.1	3.4	1.2	.52	2.5	2.4	1.4	.39	1.7	1.9	1.8	-.31
AN-73	IV	3.1	5.2	1.2	-.59	2.3	2.6	1.4	.42	1.9	2.5	1.8	-.36
RS-S	I	9.8	.05	1.6	.35	8.7	.02	1.7	.42	8.6	.15	1.7	.20
RS-S	II	9.2	.23	1.6	.18	8.7	.05	1.6	.40	8.4	.07	1.7	.27
RS-S	III	10.6	.07	1.3	.35	8.2	.04	1.8	.43	8.3	.10	1.7	.26
RS-X	I	8.9	.02	2.4	.39	8.7	.04	2.4	.47	10.3	.04	2.2	.45
RS-X	II	8.5	.01	2.3	.34	8.5	.03	2.3	.47	10.1	.06	2.1	.39
RS-X	III	9.1	.03	2.4	.36	8.7	.04	2.4	.47	10.6	.04	2.1	.46
Ferrite	II	8.0	-.11	2.1	2.7	6.1	.02	2.0	5.9	6.7	-.23	1.9	.03
Ferrite	III	6.2	.08	1.9	4.1	6.1	.07	1.8	3.4	6.8	.01	1.6	.05
Radite	I	10.4	.08	2.8	.47	10.3	.12	2.9	.51	10.0	.20	2.7	.43
Radite	II	10.5	.07	2.9	.48	10.9	.03	2.8	.57	10.5	.16	2.6	.39
Radite	III	11.5	2.6	10.1	.82	10.7	.11	2.9	.50	10.0	.21	2.8	.42
CR	I	12.1	.01	3.6	.55	12.2	.05	3.4	.63	13.2	.21	3.2	.43
CR	II	15.2	.12	3.3	.48	14.4	.05	3.0	.66	16.3	.20	3.1	.40
CR	III	10.7	0	3.6	.70	9.7	-.06	3.8	.95	13.2	.19	3.4	.40

TABLE II-2: (concluded)

Material and Number		5.5 GHz				6.0 GHz			
		ϵ_r		μ_r		ϵ_r		μ_r	
		mag.	tanδ	mag.	tanδ	mag.	tanδ	mag.	tanδ
LS-22	I	2.1	.59	1.0	-.01	2.2	.55	.93	.12
LS-22	II	1.7	1.4	1.1	-.47	2.2	.64	.94	.07
LS-22	III	2.0	.79	1.0	-.05	1.9	.61	1.0	.05
LS-24	I	4.2	.99	.94	.03	4.3	1.2	1.0	-.002
LS-24	II	4.6	1.8	.63	-.23	4.4	1.4	1.0	-.07
LS-24	III	4.5	.91	.90	.09	4.3	1.1	.97	.05
LS-26	I	4.2	1.2	.85	.01	4.4	1.3	.91	.04
LS-26	II	4.3	1.3	.90	.03	4.3	1.5	.96	-.04
LS-26	III	4.2	1.4	.93	.08	4.1	1.9	1.3	-.16
AN-72	I	3.5	1.1	.96	-.25	3.3	1.6	1.1	-.34
AN-72	II	3.5	1.5	.97	-.34	3.1	1.7	1.1	-.39
AN-72	III	3.6	1.1	.94	-.26	3.4	1.4	1.0	-.33
AN-73	I	2.0	1.6	1.5	-.29	1.85	1.3	1.6	-.21
AN-73	III	1.7	.14	1.5	-.28	1.7	1.1	1.6	-.16
AN-73	IV	2.0	.79	1.1	-.08	1.7	1.3	1.7	-.20
RS-S	I	12.4	.06	1.1	.54	9.8	.02	1.3	.44
RS-S	II	12.0	.06	1.1	.55	9.4	.08	1.4	.39
RS-S	III	11.9	.07	1.1	.45	9.6	.02	1.3	.45
RS-X	I	7.6	.01	2.2	.57	7.6	.01	2.3	.64
RS-X	II	7.4	.02	2.3	.53	7.8	.01	2.2	.62
RS-X	III	7.5	.01	2.2	.57	8.3	.02	2.2	.63
Ferrite	I	5.8	.18	.93	4.3	6.6	.02	1.2	6.0
Ferrite	II	5.3	.07	1.2	3.8	5.7	.02	1.2	5.7
Radite	I	11.8	-.13	2.2	1.1	12.2	-.10	2.1	1.0
Radite	II	11.1	-.20	2.5	1.2	11.0	-.17	2.4	1.4
Radite	III	11.7	-.16	2.3	1.1	10.7	-.22	2.4	1.3
CR	I	12.6	-.08	2.7	1.04	12.1	-.13	2.8	1.36
CR	II	15.6	-.06	2.6	1.0	15.0	-.09	2.6	1.2
CR	III	12.2	-.10	2.8	1.2	12.0	-.07	2.7	1.3

From the values presented in Table II-2, practically any desired quantity characterizing the material can be calculated. The normalized intrinsic material impedance is easily computed from

$$\eta = \left(\frac{\mu_r}{\epsilon_r}\right)^{1/2} , \tag{2.2}$$

and the propagation constant can be computed from

$$\gamma = j\frac{2\pi}{\lambda}(\mu_r \epsilon_r)^{1/2} . \tag{2.3}$$

The losses encountered by a wave propagating through an infinite block of material are represented by the real part of γ. Using the measured values, this attenuation has been calculated and is displayed in Figs. 2-8 and 2-9. Only the points on these plots were derived from μ_r and ϵ_r, the interconnecting lines being added to guide the eye from point to point. Note that the magnetic materials have more loss than the purely dielectric ones and that the Eccosorb CR performance is roughly that of a ferrite.

We regard the materials evaluation program as 99 per cent complete reserving the other 1 per cent for further study of other materials if the theoretical work calls for further information.

The impedance boundary condition which will characterize absorbing materials must relate the tangential electric and magnetic fields on the absorber surface. A simple statement of the impedance boundary condition we seek to use is (see Fig. 2-1)

$$E_\phi = -\eta Z_0 H_s \tag{2.4}$$

where

$$Z_0 = \sqrt{\mu_0/\epsilon_0}$$

is the characteristic impedance of free space.

Equivalently, by normalization with respect to the incident field intensities

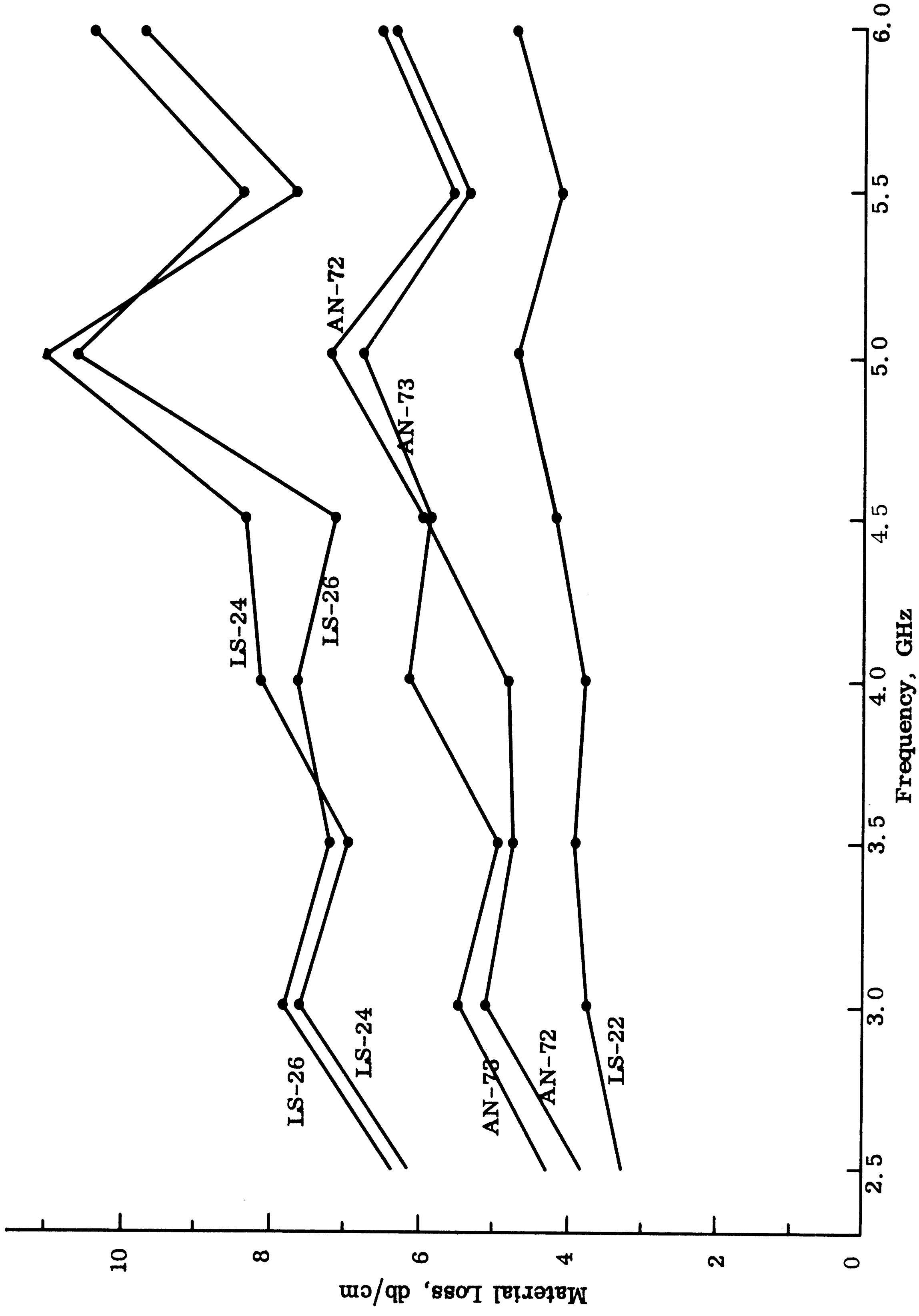

FIG. 2-8: DIELECTRIC ABSORBERS HAVE RELATIVELY MODEST LOSSES.

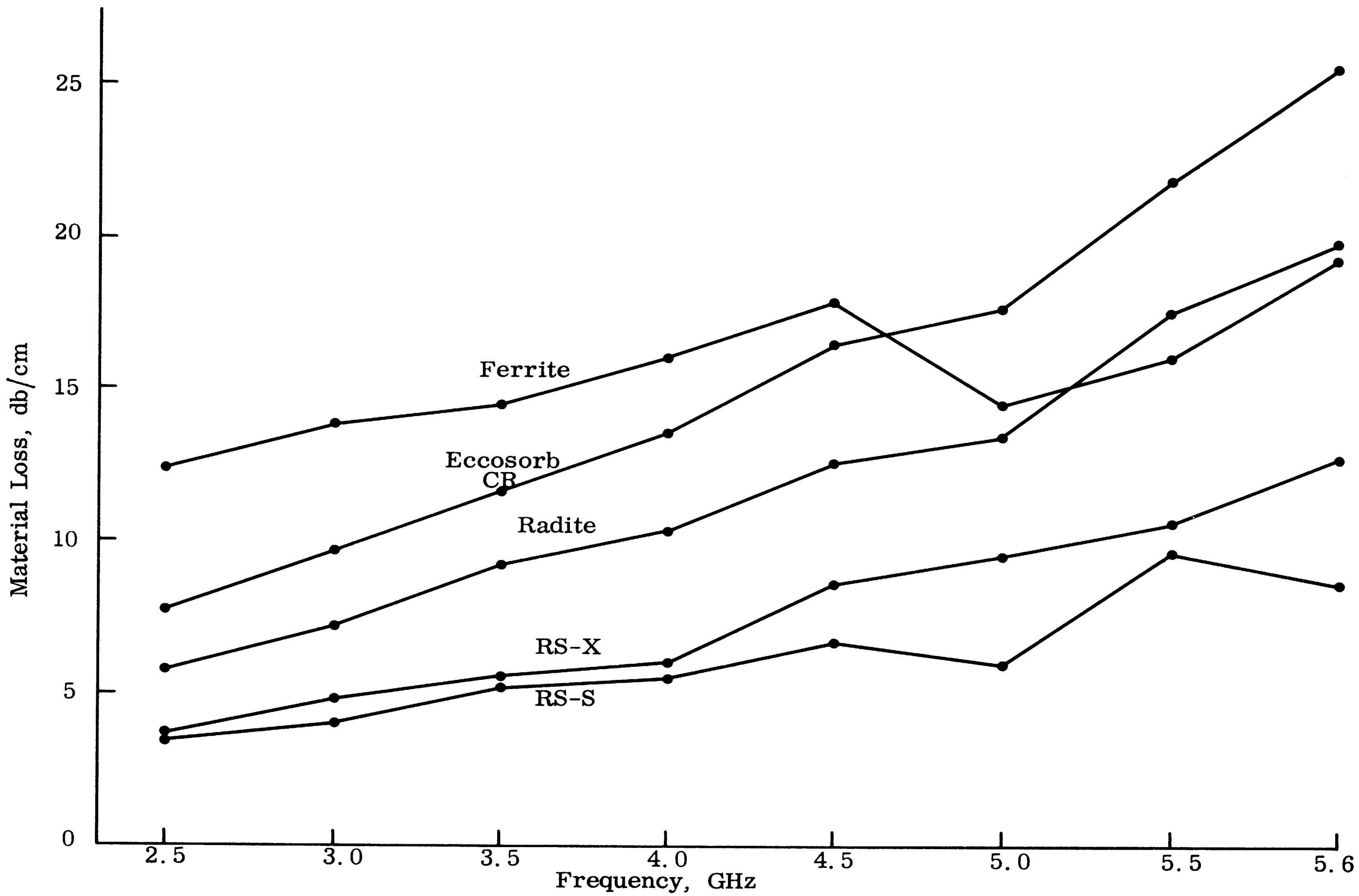

FIG. 2-9: LOSSES OF MAGNETIC MATERIALS ARE GREATER THAN THOSE OF THE DIELECTRIC MATERIALS.

E_o and H_o (which would be measured in the absence of any obstacle),

$$\frac{E_\phi}{E_o} = -\eta \frac{H_s}{H_o} \quad . \tag{2.5}$$

Taking magnitudes only, we have

$$\frac{|E_\phi|}{|E_o|} = |\eta| \frac{|H_s|}{|H_o|} \quad . \tag{2.6}$$

Hence, if the boundary condition is valid, then the magnitudes of the normalized field intensities will be related by a constant, and this constant is determined by the intrinsic impedance of the absorber,

$$|\eta| = \left|(\mu_r/\epsilon_r)^{1/2}\right| \quad . \tag{2.7}$$

With this in mind, consider the plot of Fig. 2-10. Observe that the two curves, one being electric and the other magnetic field, seem to be separated by a constant number of decibels, suggesting that (2.6) is satisfied. If we proceed to find the difference between the curves in db and plot the ratio of

$$\frac{|E_s|}{|E_o|} \Bigg/ \frac{|H_\phi|}{|H_o|}$$

in db as a function of distance along the surface, we obtain the gentle undulation described by the dots of Fig. 2-11. Note that after some initial excursions have been damped out, the dots trace out a sinusoid along the conical surface, oscillating about some mean value. As we progress around the spherical base in the shadow region we find a sudden rise then a rapid fall to the value at the rear of the object. The 'constant' ratio between E_s and H_ϕ is good along the cone side but not in the shadow region.

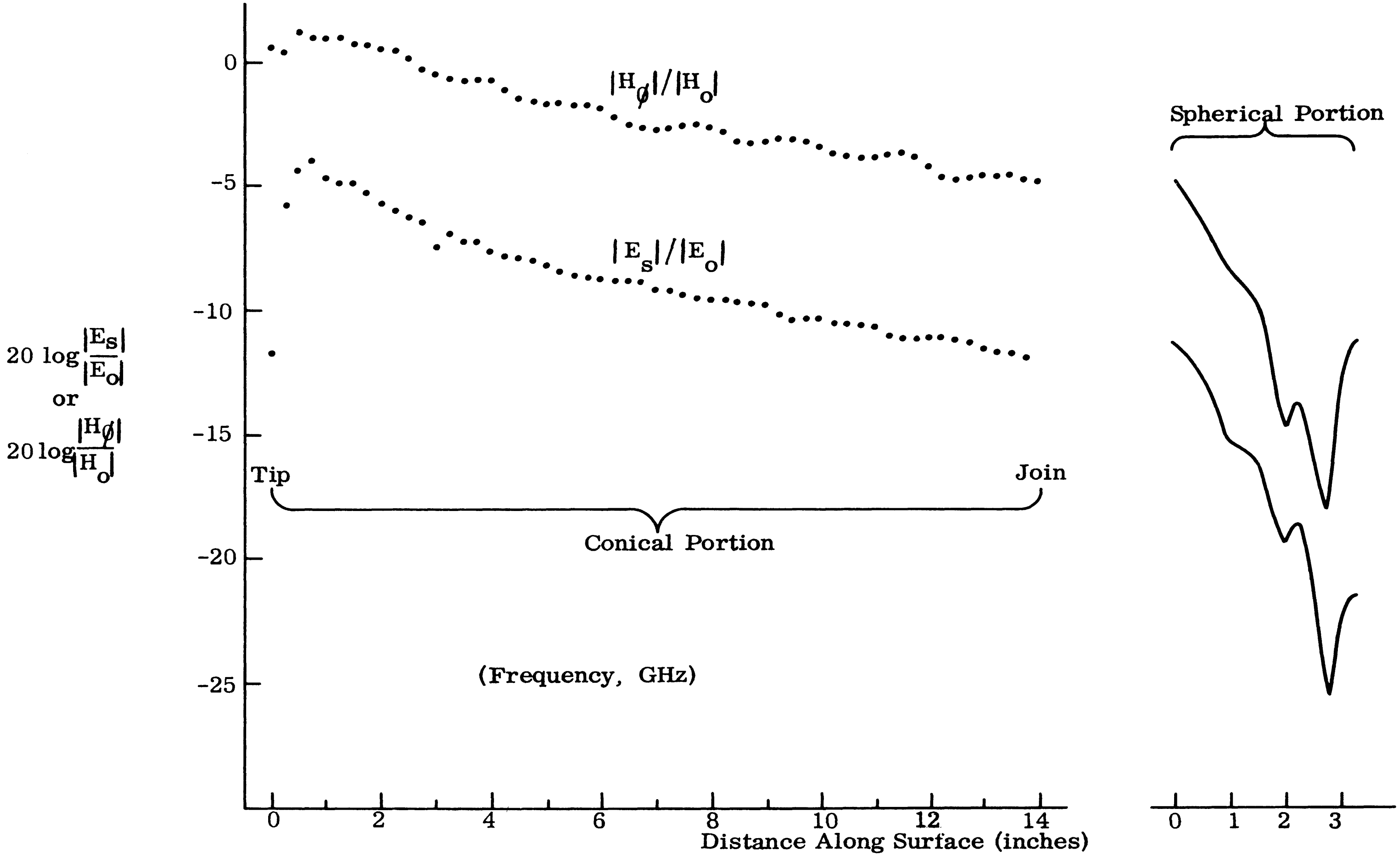

FIG. 2-10: THE MEASURED FIELDS ON A COATED CONE-SPHERE (ECCOSORB CR, ka=5.0, kb=6.25) SEEM TO BE RELATED BY A CONSTANT.

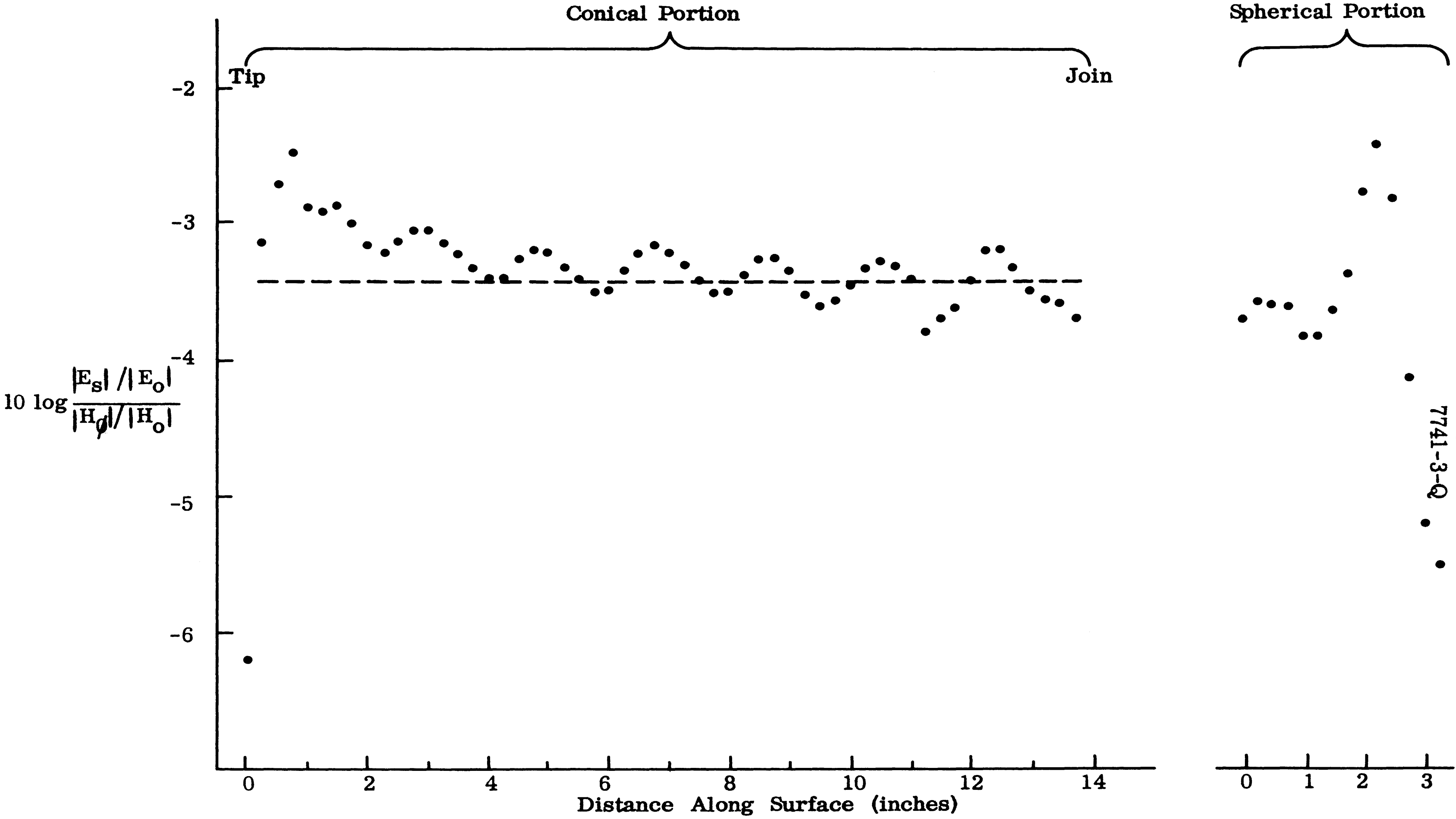

FIG. 2-11: THE RATIO OF ELECTRIC TO MAGNETIC FIELD VARIES ABOUT SOME MEAN ALONG THE CONICAL SURFACE (Data derived from Fig. 2-10).

We now turn to the electromagnetic properties listed in Table II-2 for Eccosorb CR at 6.0 GHz (we would like values for 6.25 GHz, corresponding to the frequency of the surface field measurements, but 6.0 GHz was the maximum frequency). Taking average values of the three samples measured, we find the impedance

$$\eta = (\mu_r/\epsilon_r)^{1/2} = 0.456 = -3.41\,\text{db}.$$

This value is the dashed line appearing in Fig. 2-11 and it agrees well with the mean value the oscillating datum points tend to approach. For low loss materials this advantageous behavior may not appear, and our efforts have been devoted largely to absorbers with substantial loss. On the basis of comparisons such as those presented above, we expect to successfully employ the impedance boundary condition concept.

2.1.6.1 Frequency Variation

In addition to the stated L-, S- and C-band frequencies, a few measurements have been made for the smaller models at X-band frequencies. This subtask is complete.

2.1.6.2 Glancing Incidence

Data have been obtained on cylinders using a 'home-made' absorber which we applied on one particular cylinder. The impedance boundary condition seems to hold even better than that on the coated cone-sphere data described above. This statement is based upon observations of the ratio of electric to magnetic field intensity, which was relatively constant around the cylinder except for a small sector in the shadow. Unfortunately, we do not have an independent value for the η of the material and thus cannot compare the surface field measurements with, say, values obtained by transmission line techniques.

As a matter of course, the cone-spheres have been regularly measured with the incident wave impinging on the cone surface at glancing incidence. These measurements are described under Tasks 2.1.1, 2.1.3 and 2.1.6. This subtask is 80 per cent complete.

2.1.6.3 Typical Re-entry Shapes

The model shapes which are being studied are based upon the LORV-8 and Mark XII re-entry vehicles. The cone-angle and the base termination of the models approximates that of each of these 'typical' shapes. We plan to make measurements on a double coating applied to a cone-sphere. We currently have a model coated with a good magnetic absorber and a low loss coating will be found with which to cover it. Tentative plans are for a thin sheet of teflon to be secured to the model ($\epsilon_r \cong 2.0$) or for a layer of wax dielectric to be molded or dipped on. The latter could be parafin, bees wax or the like but their losses may be more than that of teflon.

2.1.7 Far Field Measurements

Some of the model support problems which accompany backscatter measurements of low cross section shapes have been solved by the use of strings while others, mainly that of systems sensitivity conflicting with far field range requirements, have not. A Scientific Atlanta Model 5103-1 Antenna Positioner is needed and steps are being taken toward procuring one for measurements to be made in continuing phases of the SURF program. In spite of difficulties, radar cross section patterns have been obtained for a range of ka values and absorbers as outlined in Table II-3. Figures 2-12 through 2-15 show typical patterns for the bare cone-sphere and the cone-sphere covered by each of three coatings. The measurement frequency in these cases was 8.43 KHz. Task 2.1.7 is regarded as being 95 per cent complete, with the other 5 per cent being reserved for measurements which may be required for the theoretical analysis.

TABLE II-3: BACKSCATTER MEASUREMENTS OF 15° CONE-ANGLE CONE-SPHERE

ka	Base Diameter, a (in.)	Coatings Used
6.73	3.00	LS-22, LS-24, LS-26
4.65	3.00	
3.01	3.00	
6.75	4.42	LS-22, LS-24, LS-26
4.51	4.42	
3.96	4.42	
2.98	4.42	

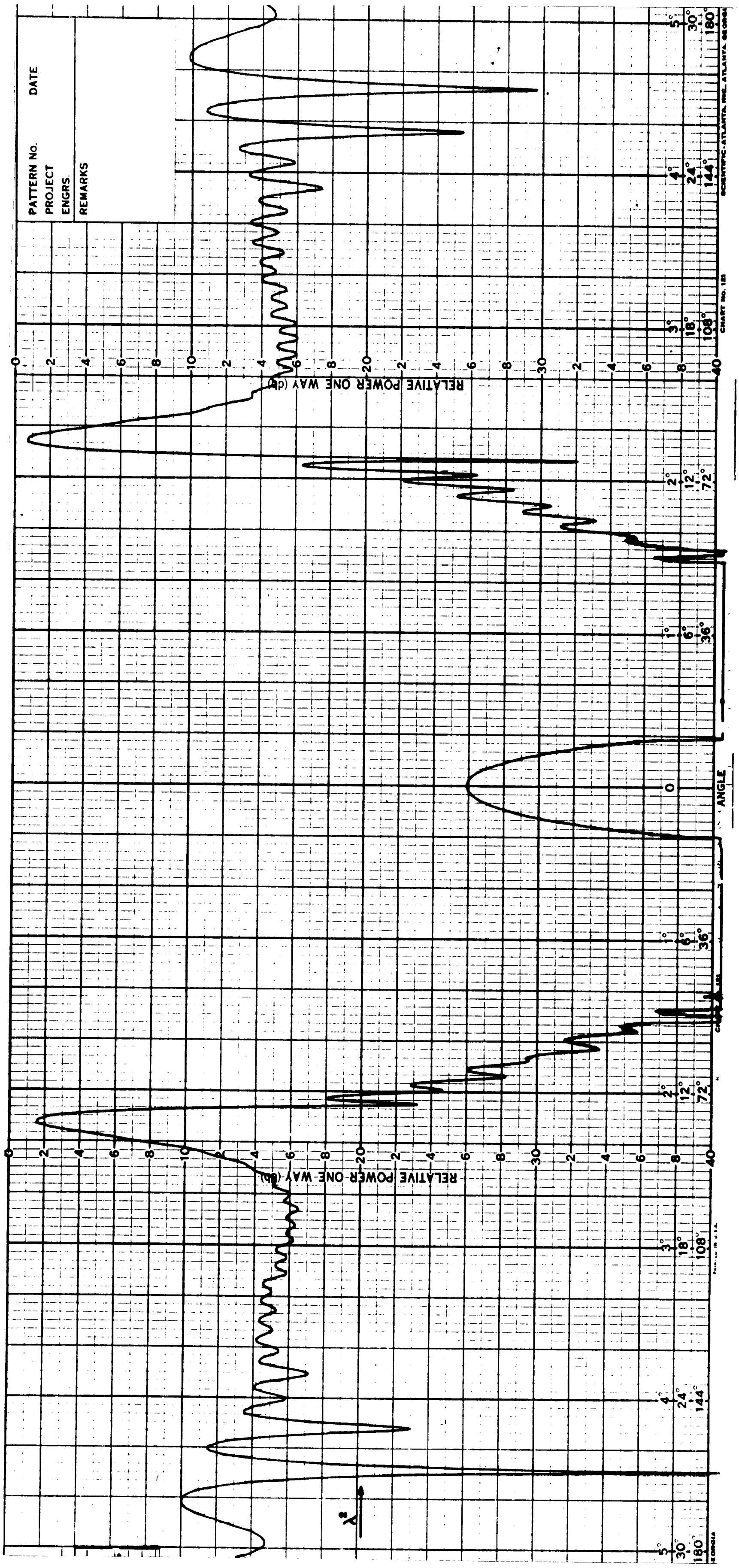

FIG. 2-12: RADAR BACKSCATTERING CROSS SECTION FOR AN UNCOATED 15° CONE-SPHERE.

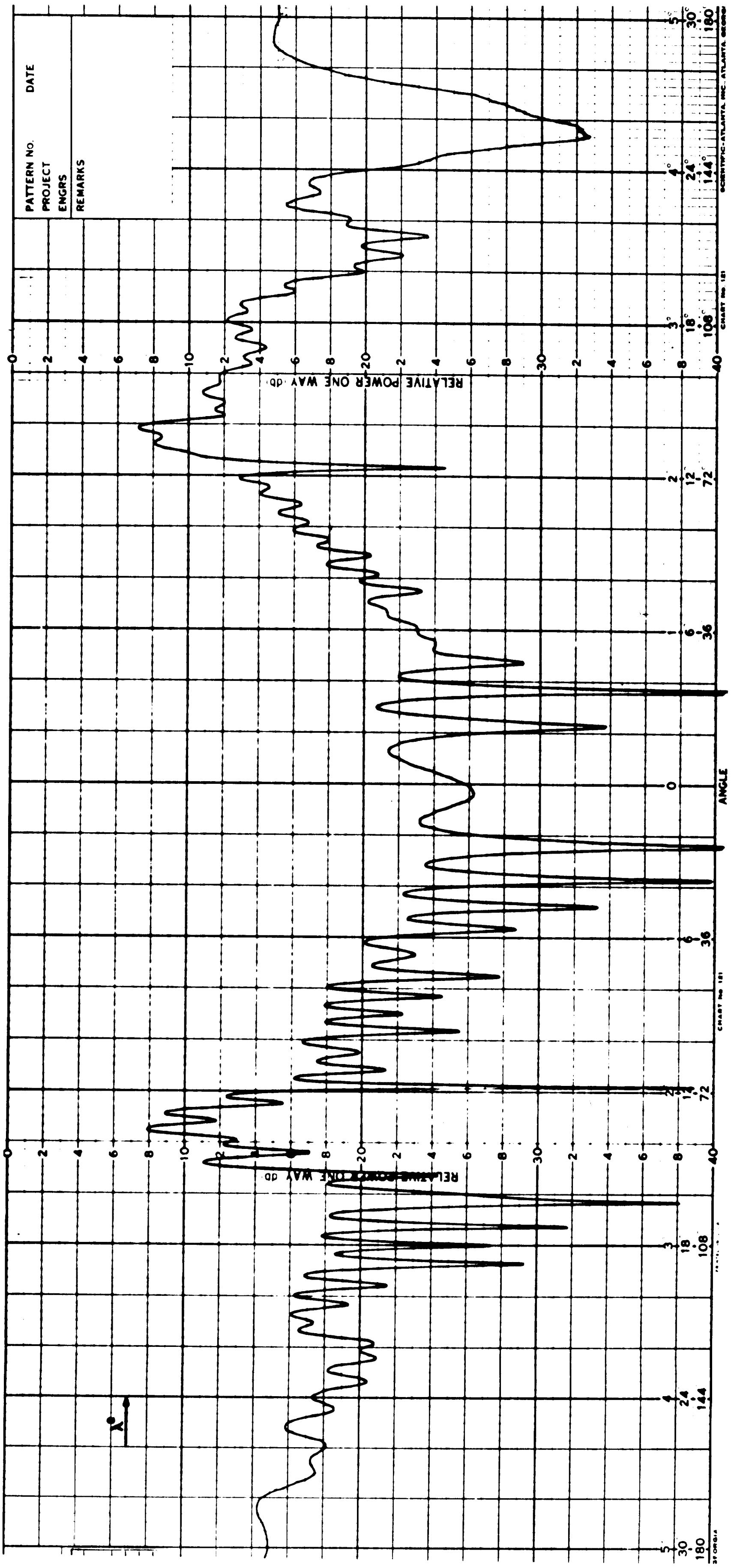

FIG. 2-13: RADAR BACKSCATTERING CROSS SECTION FOR A 15° CONE-SPHERE COATED WITH LS-22.

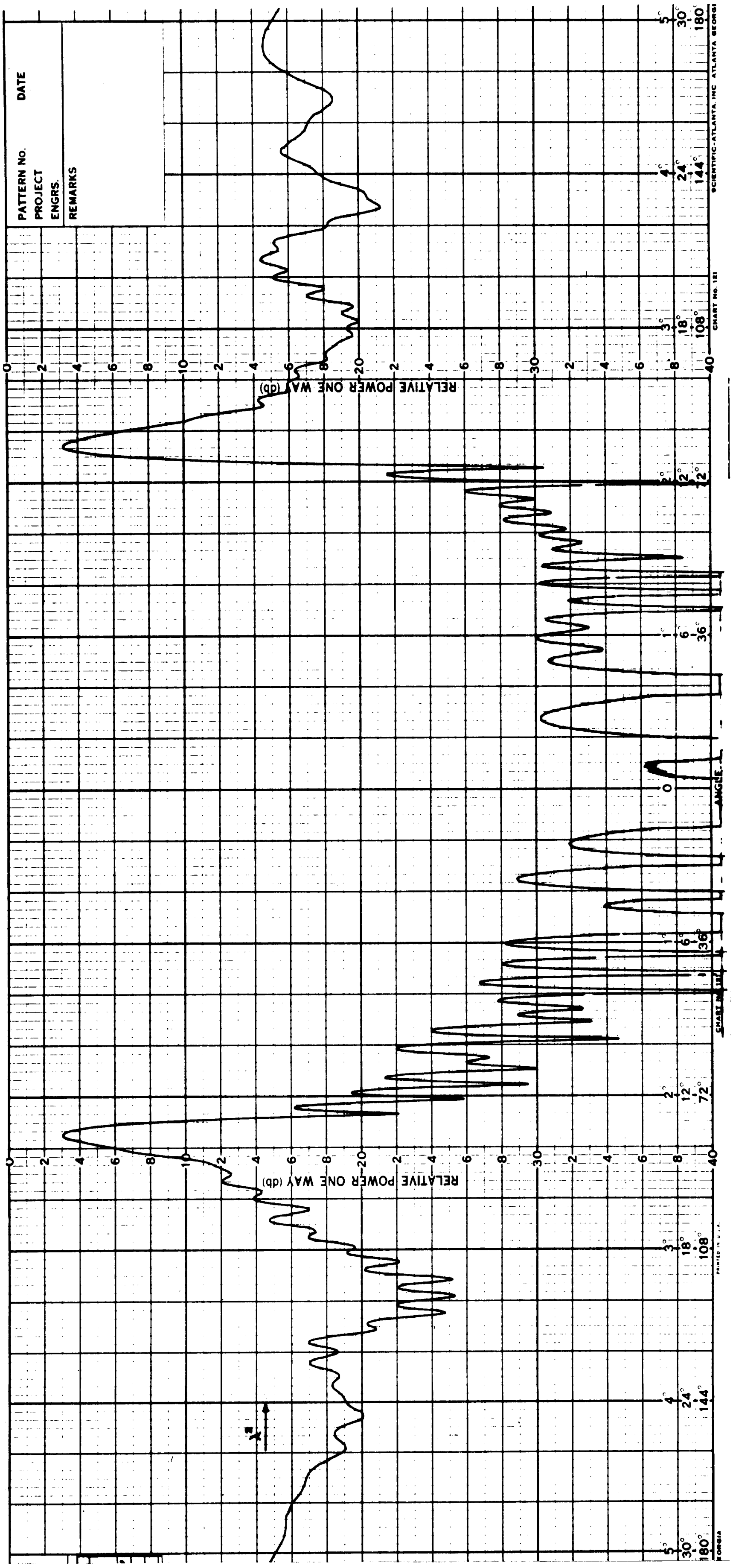

FIG. 2-14: RADAR BACKSCATTERING CROSS SECTION FOR A 15° CONE-SPHERE COATED WITH LS-26.

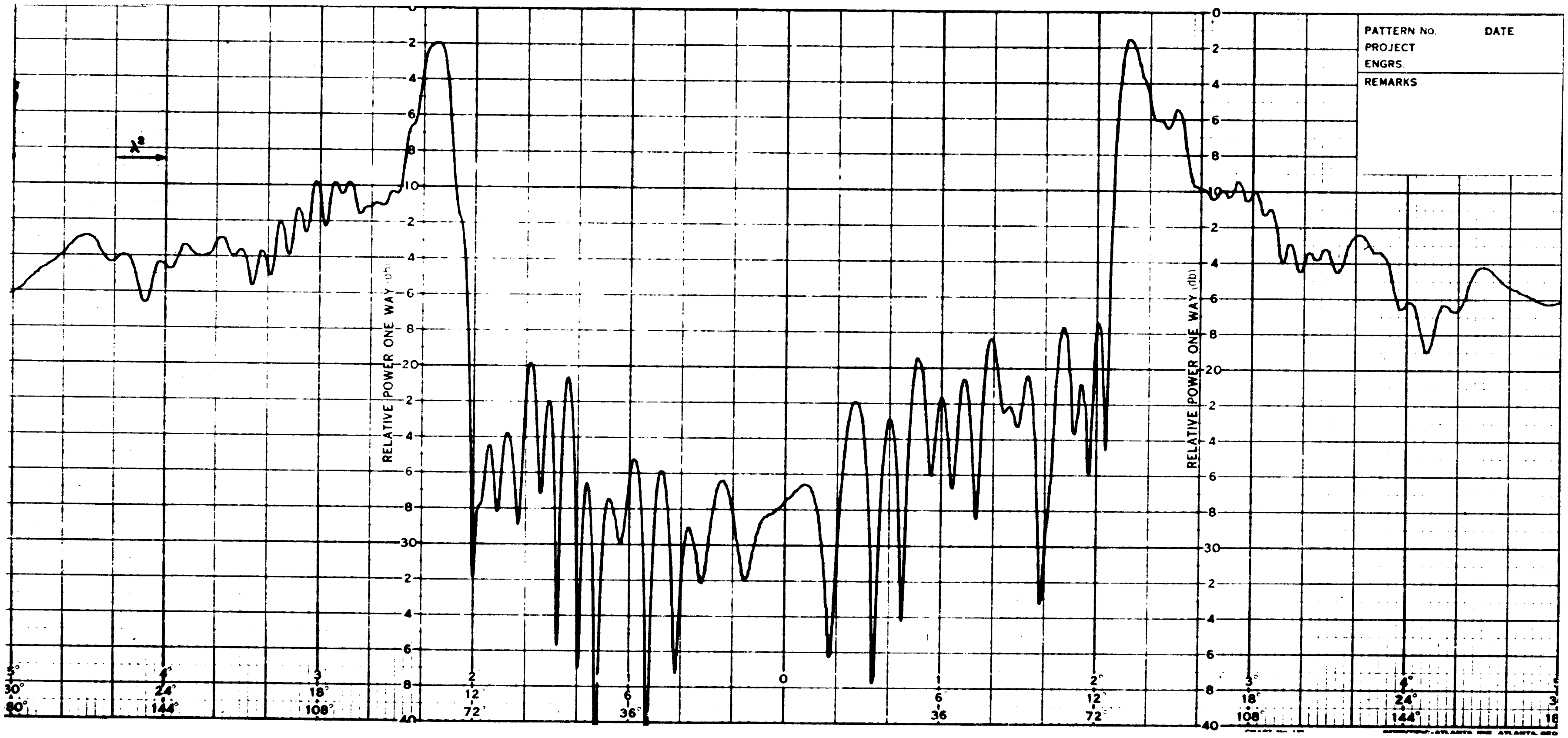

FIG. 2-15: RADAR BACKSCATTERING CROSS SECTION FOR A 15° CONE-SPHERE COATED WITH LS-24 AND V-58.

2.1.8 Antenna and Rocket Nozzle Perturbations

We approached the experimental study of perturbations by adding loops and dipoles to the surface of a perfectly conducting cone-sphere in an attempt to simulate slot antennas and rocket nozzles. Theoretical considerations indicate that to simulate a slot, one must use a loop and a dipole. In the preliminary experiments described below loops or dipoles alone were used.

The dipoles which were used were either $\lambda/4$ or $3/8\lambda$ in length and by cutting the leads of 1/4 watt carbon resistors to the proper length we were able to vary the electrical load of the elements without changing their lengths. The elements were mounted perpendicular to the surface of the conical part of a cone-sphere, as in Fig. 2-16, and the local surface currents were probed. One end of the resistor body was coated with silver paint to improve contact with the cone surface and the resistor was held in place with transparent tape of the office supply variety. The rf resistances of these loaded monopoles are not the same as the nominal dc values, but nonetheless, the data follows a definite trend as the nominal resistance is varied.

For example, in Fig. 2-17 , we observe that a monopole erected normal to the cone surface has a small perturbing effect, nearly indistinguishable from the unperturbed case, when it is open-circuited and that effect grows larger with decreasing resistance, reaching its maximum effect for short circuit. The monopole was located 18 1/2 inches from the tip and it can be seen that the effect is much stronger forward of the monopole (toward the tip) than it is to the rear of it. If the monopole length is increased to $\ell = 3/8\ \lambda$, it can be seen (Fig. 2-18) that the perturbations do not die out as they did for the $\lambda/4$ case. They are strong for all loads and attain their greatest effect for open circuit, whereas the $\lambda/4$ monopoles show a small effect for this load value.

We also attached loops to the surface of the conical portion of the cone-sphere in such a way that the wire of the loop touched the surface at a 90° angle. By virtue of the geometry of the 'ground plane' formed by the cone surface, the loops were not complete circles, nor were they half-circles, as might be the case if a flat ground plane were used. Four loop diameters were studied, and the

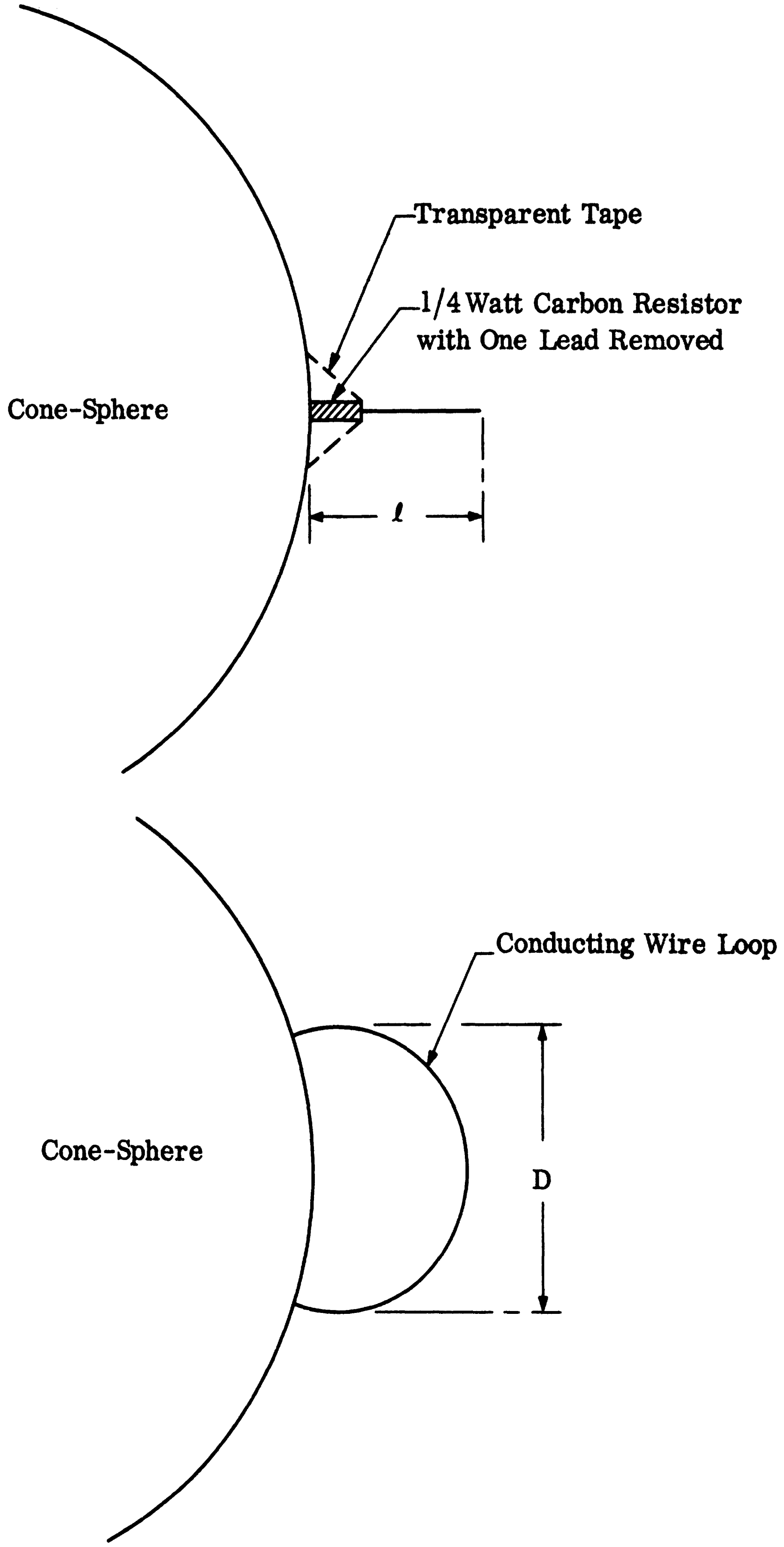

FIG. 2-16: LOAD VARIATIONS WERE AVAILABLE BY THE USE OF CARBON RESISTORS; FOUR LOOP DIAMETERS WERE USED IN A RELATED STUDY

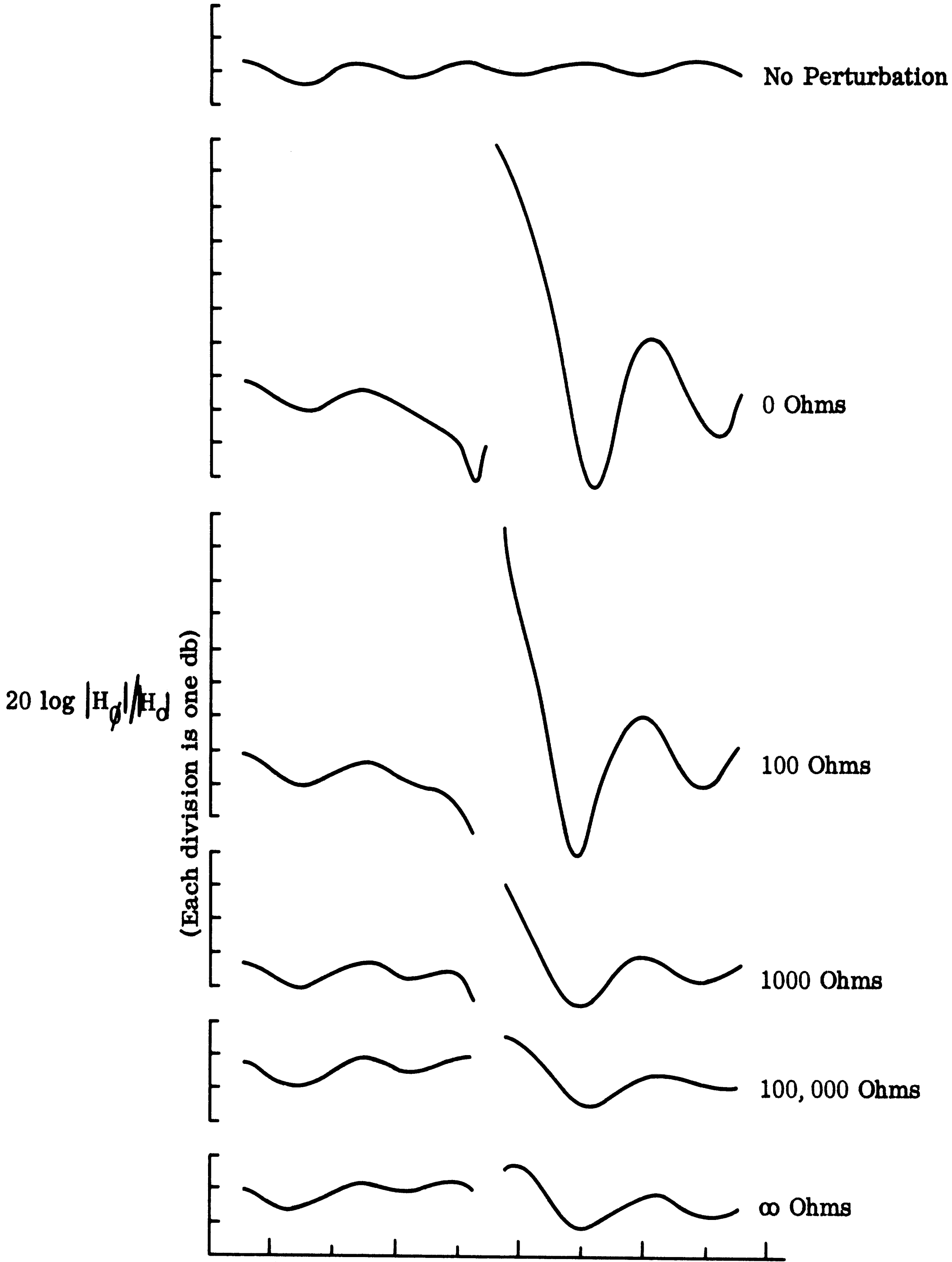

FIG. 2-17: LOCAL FIELDS OF A $\lambda/4$ LOADED MONOPOLE ON A CONE-SPHERE STRONG OR WEAK PERTURBATIONS, DEPENDING ON THE RESISTANCE VALUE.

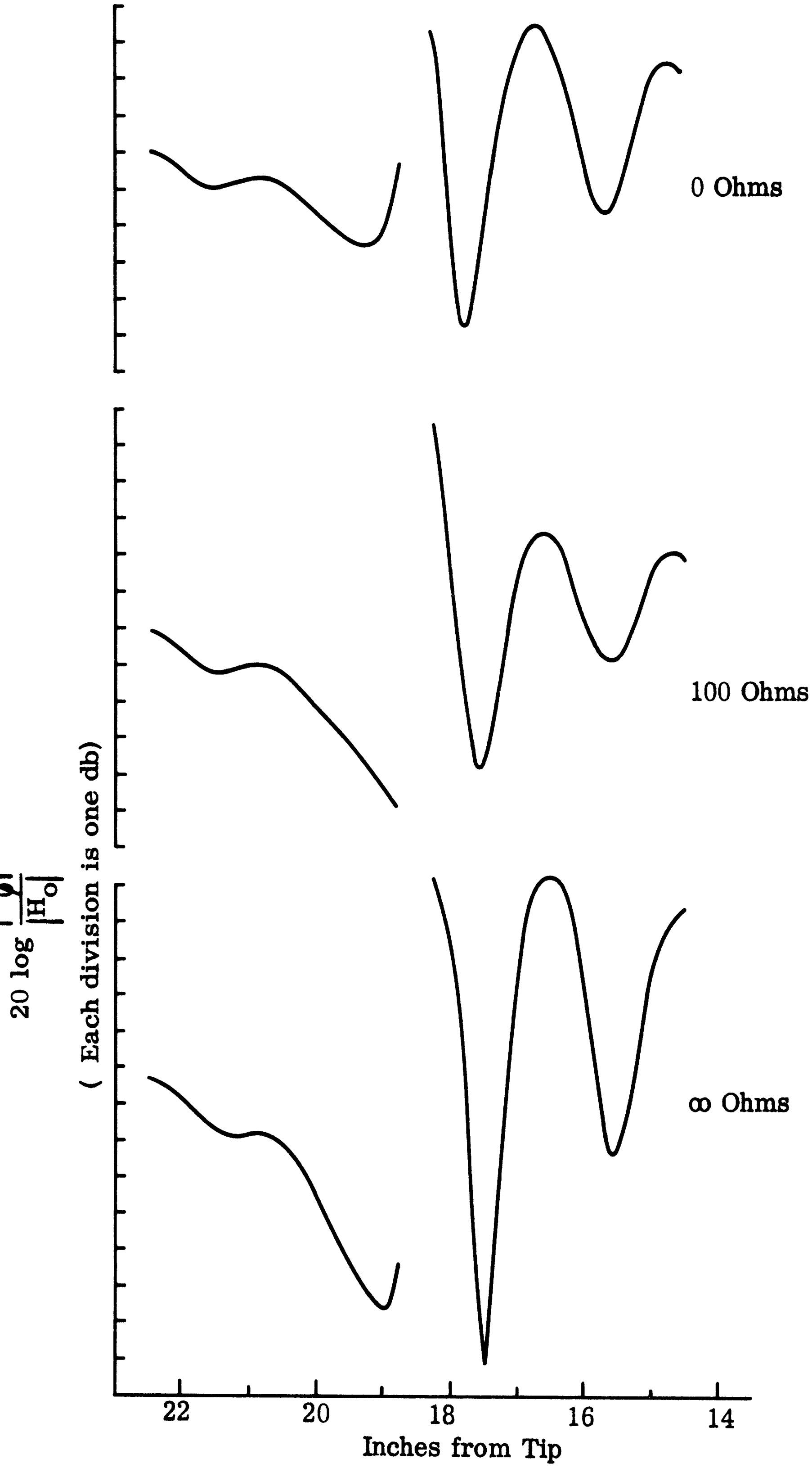

FIG. 2-18: LOCAL FIELDS OF A 3/8λ MONOPOLE ARE LESS LOAD-DEPENDENT THAN THOSE OF A λ/4 MONOPOLE AND ARE RELATIVELY STRONGLY PERTURBED.

circumferences C = π D were calculated as if the loops were perfect, complete circles. The data, shown in Fig. 2-19, exhibits strong dependence upon loop circumference (or diameter) and the effect is very small for a 0.42 λ loop circumference. The maximum perturbation occurs for C = 0.83λ and, as with the monopoles, the disturbance to the local field occurs in front of the loop (toward the tip side). There also appears to be a slight shift in the positions of the maxima and the minima as loop size is varied.

For an exact representation of a slot, we intend to have a model constructed containing a single slot. We hope to design the slot so that its electrical depth, and hence the impedance it presents, will be variable to some degree. For typical values of ka, a (full scale) C-band beacon slot will have a small, and probably unmeasurable, effect but a low- frequency telemetry slot should have a large effect. For typical full scale re-entry shapes , such as the Rex I and II, a typical telemetry slot is about 17 per cent as long as the vehicle itself. We shall attempt to model such a slot and a C-band slot may be included. The monopoles discussed above were also positioned in the shadow region of the cone-sphere, and there they turned out to have a much smaller effect, presumably because of the much weaker field intensities.

Nozzles are electrically very much smaller than the monopoles. After determining their sizes on full scale vehicles, we discovered that the exposed portions of typical nozzles are very small in relation to the cone-sphere radius; a sketch of their approximate relative size appears in Fig. 2-20. From theoretical considerations we felt the effects of such small protuberances would be small, and subjected this expectation to the test of experiment. A basic cone-sphere was fitted with small button-like studs scaled to represent nozzles (Fig. 2-20) and the fields were measured with and without the studs for ka = 3.0 and 5.0. The results showed the effects of the studs were not measurable within the limits of experimental error (less than 0.1 db) and it is probable that even larger perturbations would have very small effects. We conclude that typical rocket nozzles have no effect because of their small size relative to that of the re-entry object itself.

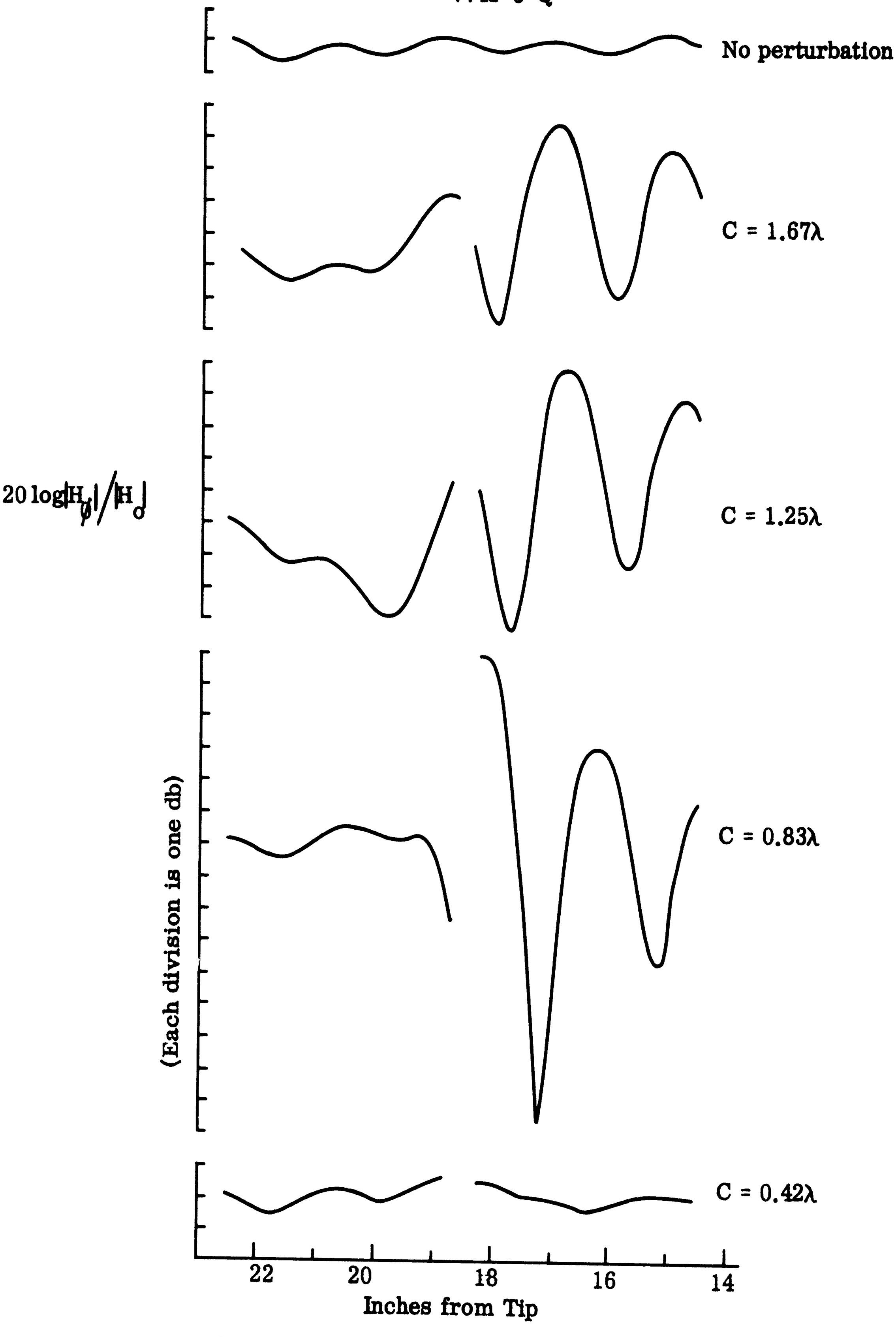

FIG. 2-19: PERTURBATIONS DUE TO A LOOP MOUNTED ON THE SURFACE PRACTICALLY DISAPPEAR WHEN THE LOOP CIRCUMFERENCE IS 0.42λ.

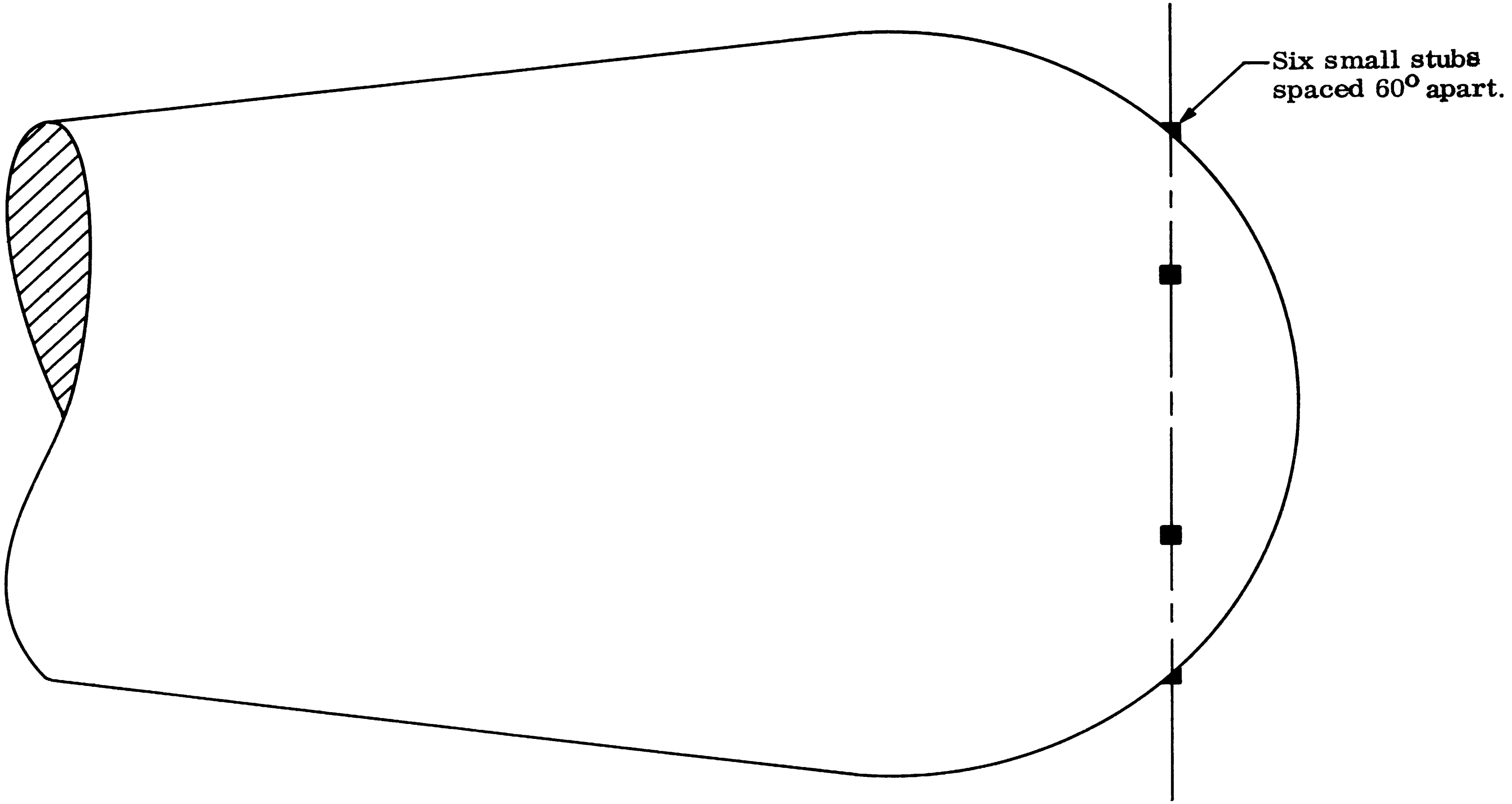

FIG. 2-20: THE SMALL SIZE OF ROCKET NOZZLES IS ILLUSTRATED IN THIS APPROXIMATELY SCALED SKETCH OF THE LORV - 8

Another perturbation studied was that of a nose antenna characteristic of those found on the LORV - 8 . We modified the front portion of an existing cone-sphere by fitting the nose with a Lucite Disk 1/4 inch thick, as in Fig. 2-21. The disk was sandwiched inbetween the tip and the cone body proper and was held in place with epoxy resin glue. The surface currents were measured for ka = 1.0, 3.0, 5.0 and 8.0 and the backscatter patterns were also obtained.

As shown in Fig. 2-22, the surface fields near the tip are extraordinarily different from those found on an undisturbed cone-sphere. In this figure, for which ka = 5.0, the tip antenna simulation data are represented by the dashed line, while those of a plane cone-sphere are the solid trace. For this particular frequency the circumference of the Lucite disk is almost exactly one wavelength, which corresponds to a strongly anti-resonant condition, and it can be seen that the surface currents forward of the dielectric are severely changed compared to that of the plain cone-sphere. Aft from the disk the currents approach those ordinarily found on a plain cone-sphere so rapidly that the curves are indistinguishable 7 inches beyond the tip. On the basis of data in Fig. 2-22, we would expect the backscatter from the antenna simulation model to be larger than that from its plain counterpart, and the recorded backscatter patterns confirm this expectation. It is observed that the surface field to the rear of the dielectric spacer is exactly the same as that on a plain cone-sphere. This is similar to the observation during the first year's work on blunted noses; the changes in nose (tip) geometry had no effect on the creeping wave.

The work on this task has been more extensive than anticipated in the Program Plan. We still plan to look at actual slots as well as dipole and loop representations and we therefore estimate this task to be 75 per cent complete.

2.1.9 Probe Design

We have developed probes with which to measure tangential and radial electric fields and have described them in previous Quarterly Reports. Phase measuring capability has long since been demonstrated. This task is considered to be complete.

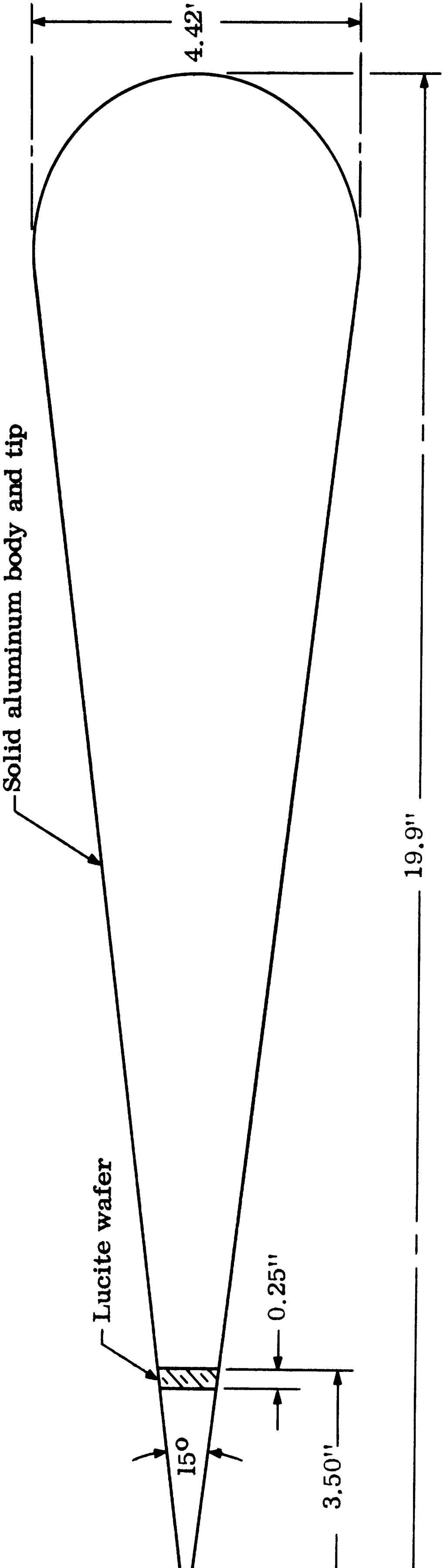

FIG. 2-21 : A NOSE-TIP ANGENNA WAS SIMULATED BY THE USE OF A LUCITE WAFER.

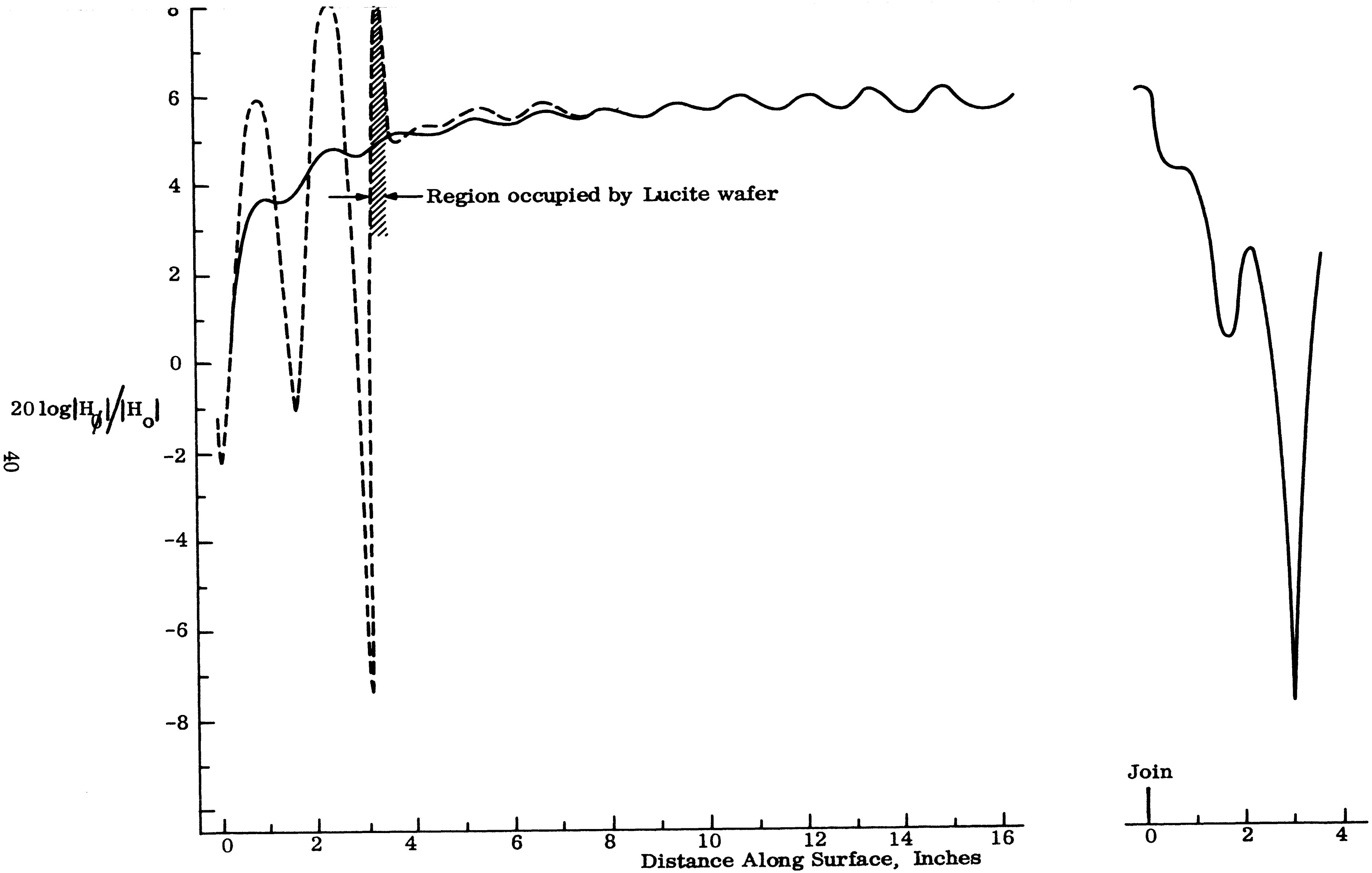

FIG. 2-22: SURFACE CURRENTS OF NOSE ANTENNA (DASHED LINE) APPROACH THOSE OF PLAIN CONE-SPHERE (SOLID LINE) RAPIDLY BEYOND THE DIELECTRIC WAFER.

2.1.10 Concave Surfaces

Concave surfaces provided by the indented base models ID-1, -2, and -3 were discussed under Task 2.1.5. The indented models were of interest in that task since the sharp radius of curvature near the join brings about a confluence of the join and shadow boundaries. Hence the models are suited for both Tasks 2.1.5 and 2.1.10. Task 2.1.10 is about 75 per cent complete.

2.1.11 Absorber Fairings

This task is concerned with studies of incomplete coatings. If partial coatings are used upon re-entry shapes and the coating is abruptly terminated, the discontinuity so formed may give rise to a strong echo. One way to suppress this echo is to fair the absorber from finite thickness to zero thickness and another way is to serrate the terminating edge to reduce the singularity. The latter is the easiest to model in the laboratory and this condition will be examined first. Actual measurements have not been performed, but soon will be. Preliminary fairing design has been done under this task which may be considered to be 5 per cent complete.

2.1.12 Plasma Sheath Experiments

No measurements are planned for this year. Factors which require experimental data are being selected from theoretical examinations involving typical meaningful plasma parameters. This work is described under Task 3.1.7.

2.1.13 Design and Construction of Models.

During this quarter several models were modified and a new one was constructed. Sketches or photographs of the new or modified models have been intoduced in this report under the appropriate tasks. The reader may refer to the following figures for approximate model shape and size (only new or modified models are considered): Figures 2-4, 2-5 and 2-21.

In addition to the above models, one having a slot antenna will be constructed. The slot configuration will be approximately that shown in Fig. 2-23.

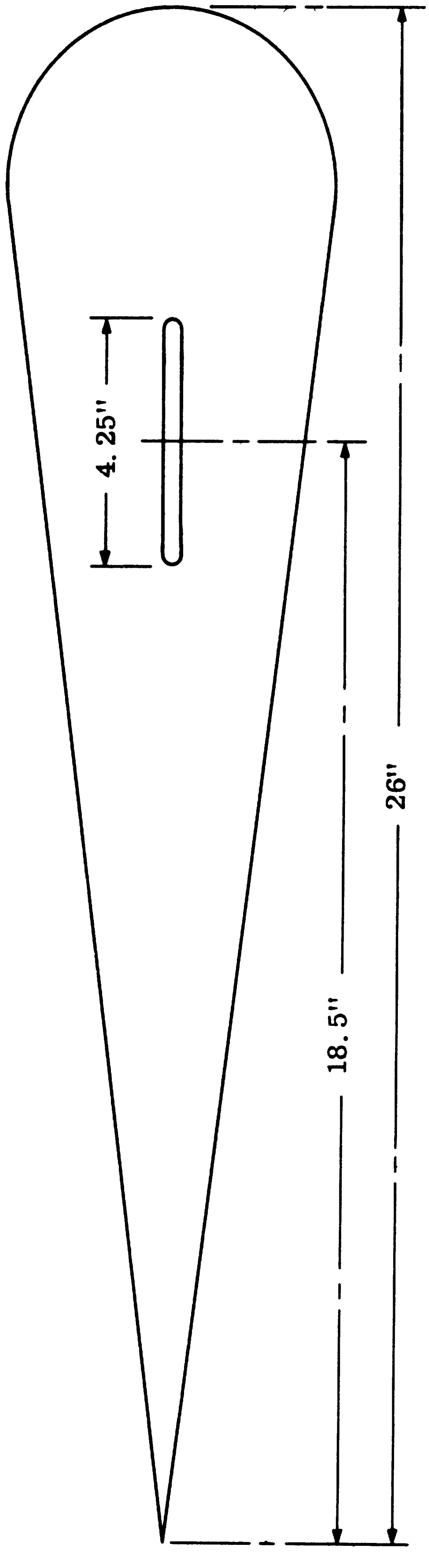

FIG. 2-23 : PROPOSED SLOT DESIGN AS BASED UPON RELATIVE DIMENSIONS FOUND ON REX I AND II VEHICLES.

TASK 3.0: THEORETICAL INVESTIGATIONS

3.1.1 Analysis of Data and Computer Programming

A. Computer Program for Surface Currents and Radar Cross Section of Rotationally Symmetric Metallic Bodies.

Work on the digital computer programming of the computation of the surface currents induced on a rotationally symmetric metallic body such as a cone-sphere and of the resulting radar cross section is progressing through four steps: 1) The numerical algorithm has been checked, 2) Each section of the machine program has been hand-checked or independently programmed, 3) The matrix inversion routine has been tested, and 4) The synthesis of the programming is being checked.

Preliminary computer runs indicate that discrepancies still exist between the manual and machine programs. When they are resolved, it is planned to run the program for a standard metallic rotationally symmetric shape (the sphere) to check the results computed by the program with known numerical values of surface currents before proceeding to the cone-sphere. Figure 3-1 shows the status of the programming in diagrammatic form.

B. Analysis of Surface Field Measurements and of Backscatter Data

The analysis of the surface field measurements and of the radar backscatter measurements made during this quarter is described in the sections which follow. Much of the analysis relies on a comparison of the data obtained on coated shapes with the analysis made on bare metallic shapes. A considerable theoretical groundwork now exists for describing the surface currents and the backscatter obtained with bare metallic cone-spheres.

B.1: Estimating Scattering from Surface Field Data.

From studies of surface data it is important to try to make some deductions about the behavior of the scattered field. To this end we shall here confine our attention to bodies of revolution at nose-on incidence.

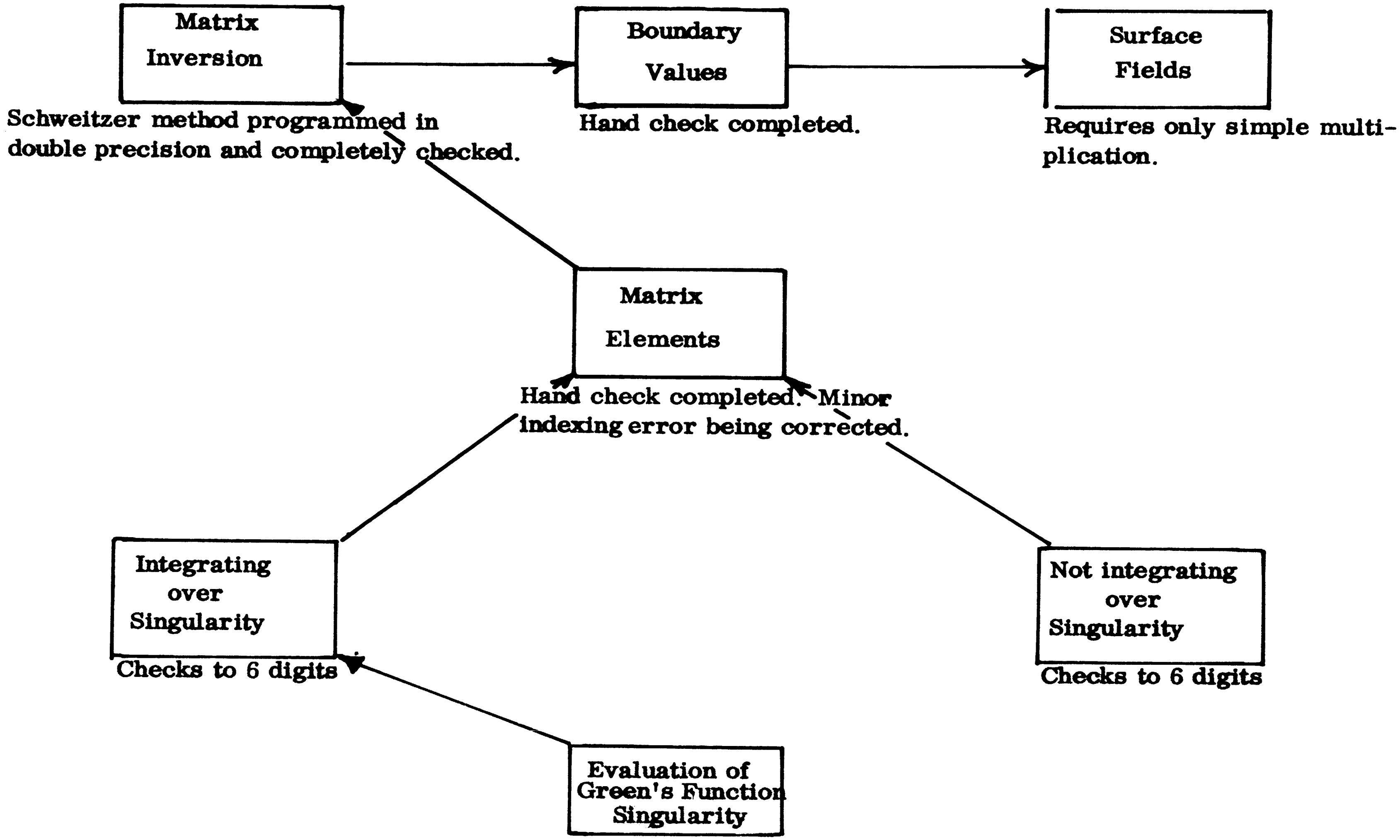

FIG. 3-1: STATUS OF DIGITAL COMPUTER PROGRAMMING OF ROTATIONALLY SYMMETRIC BODY.

Consider first the case of a perfectly conducting sphere. Let $T_2(\theta)$ be the "dominant" component of the surface field, i.e.

$$T_2(\theta) = Z \sec\phi \, H_\phi$$

where Z is the intrinsic impedance of free space. If we examine the oscillations of the surface field in the vicinity of the shadow boundary, the amplitude should be attributable, for sufficiently large ka, to the effect of the major creeping wave having circumscribed the sphere. The (complex) amplitude of the wave at this point is

$$T_2(3\pi/2) = \left\{ 1 + \frac{e^{i\frac{\pi}{3}}}{60\beta_1^2\tau^2} (13\beta_1^3 + 9) + O(\tau^{-4}) \right\} \frac{1}{\beta_1 \mathrm{Ai}(-\beta_1)} \exp\left\{ i\pi ka \left(1 + e^{i\frac{\pi}{3}} \frac{\beta_1}{2\tau^2} - e^{-i\frac{\pi}{3}} \frac{1}{120\tau^4} \left(\beta_1^2 - \frac{9}{\beta_1} \right) + O(\tau^{-6}) \right) \right\}$$

where $\beta_1 = 1.01879\ldots.$

$\mathrm{Ai}(-\beta_1) = 0.535656\ldots.$

$\tau = (ka/2)^{1/3}$

and a time factor $e^{-i\omega t}$ has been suppressed. By comparing the above expression with that for the creeping wave contribution to the far field amplitude in the back scattering direction, we have

$$S^{cw}(0) = \frac{\tau^4 e^{i\frac{\pi}{3}}}{Ai(-\beta_1)} \left\{ 1 + e^{i\frac{\pi}{3}} \frac{19\beta_1}{60\tau^2} + O(\tau^{-4}) \right\} T_2(3\pi/2)$$

and hence, to the first order,

$$S^{cw}(0) = ka \cdot \frac{\tau e^{i\frac{\pi}{3}}}{2Ai(-\beta_1)} T_2(3\pi/2) . \qquad (3.1)$$

The first factor we recognize as a focussing one. The second factor has a modulus which is close to unity for ka in the range 1 to 10, and is slowly varying as a function of ka.

Similarly, from a consideration of the creeping wave expression for the surface field at the caustic, $\theta = \pi$, we have

$$S^{cw}(0) = \frac{\beta_1 \tau}{4\pi} e^{5i\frac{\pi}{6}} \left\{ T_2(\pi) \right\}^2 . \qquad (3.2)$$

It would therefore appear that for a metallic cone-sphere we may use the amplitude of the measured surface field oscillations near the shadow boundary, or the measured strength of the surface field at the caustic, to determine the creeping wave contribution to the back scattering amplitude. To the first order we may seek to compare results for bodies of differing radius by ignoring the variation of the explicit factor τ in (3.1) and (3.2) between the two bodies; and even if the bodies (or the caps of cone-spheres) are not spherical, there is some evidence to suggest that (3.1) and (3.2 are still of value providing we write

$$\frac{\beta_1 \tau}{4\pi} = ka \cdot \frac{\beta_1}{8\pi\tau^2}$$

in (3.2), and then associate the explicit factor a with the transverse radius of curvature (as befits a focussing factor), and adopt the longitudinal radius for use in τ. Note that though these results are, nominally at least, valid only for high frequencies, experiment suggests the results should remain accurate even down to values of ka comparable to unity.

If the body is not perfectly conducting, the formulae are, of course, changed to the extent that the birth and launch weights, B and L respectively, of the creeping waves are modified by the nature of the surface. It is important that these modifications should be determined, but meanwhile, noting that (3.1) and (3.2) can be written:

$$S^{cw}(0) = ka\, L\, T_2(3\pi/2) \;,$$

$$S^{cw}(0) = ka \frac{L}{B} \left\{ T_2(\pi) \right\}^2 \;,$$

equation(3.1) should remain valid for a non-metallic surface if only the birth weight of the creeping wave is affected by the material of the surface, whilst (3.2) should remain valid if L and B are modified by the same factor.

Equation (3. 1) implies

$$\frac{\sigma}{\pi a^2} = \left| \frac{\tau}{Ai(-\beta_1)} \right|^2 A^2 \;,$$

where A is the amplitude (half the difference in levels of the maxima and minima) of the surface field oscillations near the shadow boundary. Is there some analogous formula which would enable us to deduce the back scattering from the spacer of the nose tip antenna model whose surface field data is presented in Section C under Task 3. 1. 2? A possible approach is as follows:

For a flat-backed cone of base radius a and half-angle α, the expression for the far field amplitude in the back scattering direction for axial incidence as derived from circular wedge theory is

$$S(0) = -\frac{\pi a}{n\lambda}\,\mathrm{cosec}\,\frac{2\pi}{n}\,e^{-2ika\cot\alpha}$$

(Kleinman and Senior, 1963) where $n = \frac{3}{2} + \frac{\alpha}{\pi}$. For $\alpha \ll \pi$ we can take $n \simeq 3/2$, and hence

$$S(0) = \frac{2}{3\sqrt{3}}\,ka\,e^{-2ika\cot\alpha} ,$$

giving

$$\frac{\sigma}{\pi a^2} = \frac{16}{27} .$$

If we now seek to identify a with the radius a_s of the spacer, and thereby regard the portion of the cone-sphere ahead of the spacer as a flat-backed cone, it is necessary to take into account the characteristics of the spacer itself, and this we can do by using the measured amplitudes of the surface field oscillations. By virtue of the circular wedge approximation, the theoretical surface field behavior along one generator of the flat-backed cone in the vicinity of the rim is the same as on a wedge of the appropriate angle $\frac{\pi}{2} - \alpha$, and this in turn is almost identical to the behavior of the surface field on a half-plane viewed at an angle α to grazing incidence. The surface field component of interest is H_z, where the z axis is along the edge of the half-plane, and the required expression for this component is

$$H_z = 2\,\frac{e^{-i\frac{\pi}{4}}}{\sqrt{\pi}}\,e^{-iks\cos\alpha}\,F\left[-\sqrt{2ks}\,\cos\frac{\alpha}{2}\right] ,$$

where s is here the distance from the edge, and $F(\gamma)$ is the Fresnel integral

$$F(\gamma) = \int_{\gamma}^{\infty} e^{i\mu^2}\,d\mu .$$

$|H_z|$ has been computed for $\alpha = \pi/2$ and the results are shown in Fig. 3-2. Simple scaling of the abscissa enables the graph to be applied for any value of α .

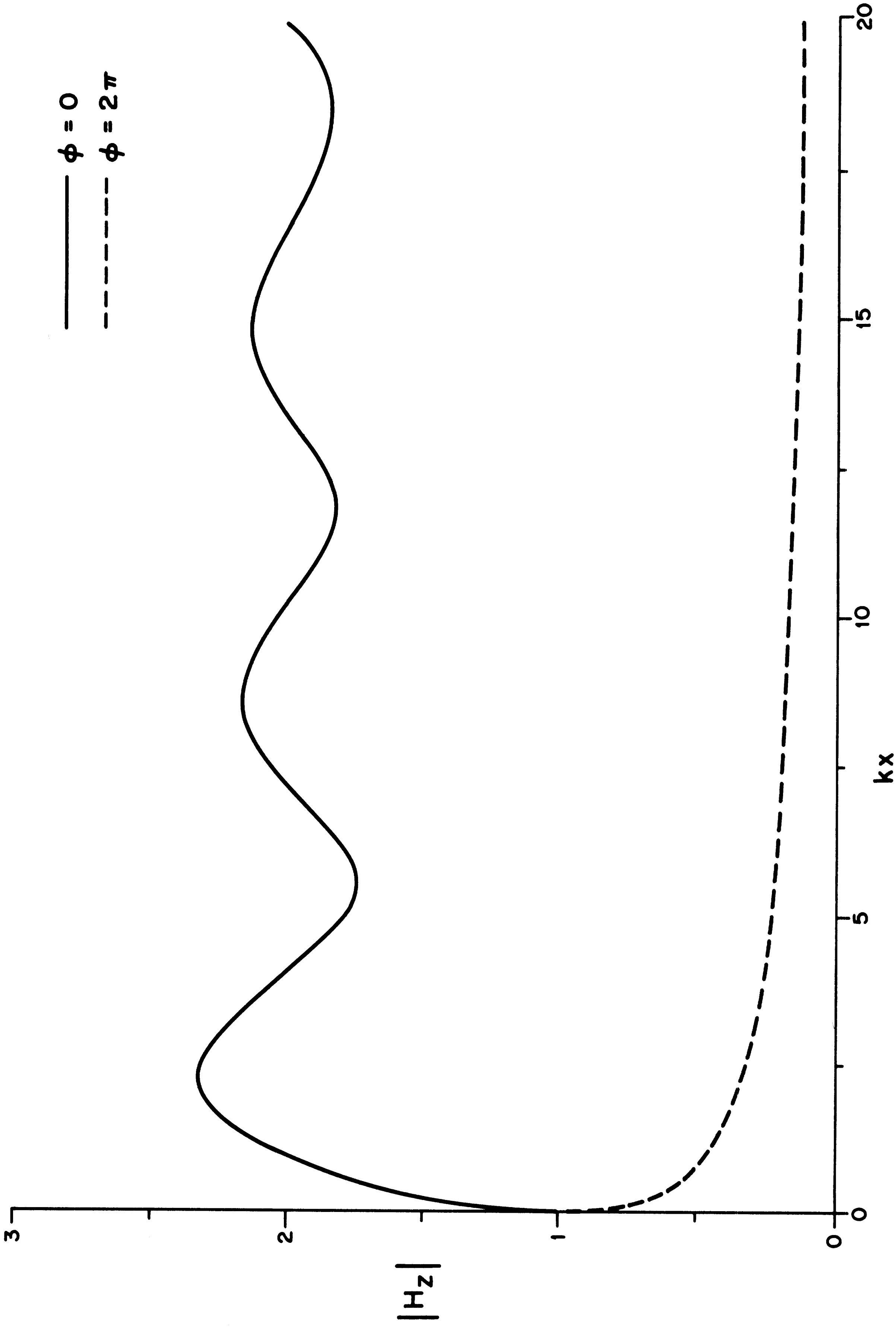

FIG. 3-2: AMPLITUDE OF THE SURFACE FIELD.

If the mean amplitudes of the measured oscillations of the surface field on the cone-sphere ahead of the spacer are compared with the amplitudes of the corresponding oscillations on the half-plane, the effective strength of the spacer, regarded as a ring source, can now be determined. Denoting this ratio of amplitudes by the symbol Γ, the contribution to the back scattering amplitude provided by the spacer is

$$S(0)=\frac{2}{3\sqrt{3}}\,ka_s\,e^{-2ika_s\cot\alpha}\,\Gamma e^{i\phi}$$

where ϕ is some unknown phase, and hence

$$\frac{\sigma}{\pi a_s^2}=\frac{16}{27}\Gamma^2 \quad . \tag{3.3}$$

It is conceivable (and indeed probable) that the parameter Γ will account for some (or perhaps most) of the resonance effects of the spacer, and lead to (3.3) being applicable for quite small values of ka_s .

Using the measured data in Section C, Task 3.1.2, we arrive at the following estimates for the cross section of the spacer on the nose tip antenna model.

Frequency (Gc)	Γ	$\sigma/\pi a_s^2$
6.799	1.29	0.98
4.2499	3.00	5.33
2.5499	0.32	0.06
0.935	~0	0

These are in reasonable agreement with the deductions from the measured far field data described in Section B.3, under Task 3.1.1.

B. 2: Back Scattering from Uncoated and Coated Cone-Spheres

A series of measurements of the back scattering cross sections of uncoated and coated cone-spheres has been carried out. In all cases the cone half-angle was 7 1/2°, and the back scattering was measured for horizontal polarization as the cone-sphere was rotated 0° - 360° about a vertical axis. From these curves the cross sections in the nose-on and specular flash (left and right) directions have been read. It is the purpose of this section to summarize the results of this preliminary analysis of the data, and to compare the values obtained with theoretical predictions.

Uncoated Cone-Spheres. Two cone-spheres were used having base radii 1.500" and 2.210". The former was measured at four frequencies and the latter at eleven. Six of the patterns were duplicates and the net effect was to provide data at nine values of ka spanning the range $2.98 < ka < 6.74$. The nose-on cross sections were deduced in the form σ/λ^2 and compared with the theoretical estimate based on the simple concept of a join contribution and an unenhanced creeping wave. A comparison of the measured data[*] with the theoretical curve is shown in Fig. 3-3, and it will be observed that the curves tends to under-estimate the cross section by anything from 2 - 4 db. This is consistent with earlier findings that indicated the existence of a creeping wave enhancement.

---

[*] The data pointed labelled 'modified experimental' have been obtained from the measured nose-rocks rather than from the actual patterns.

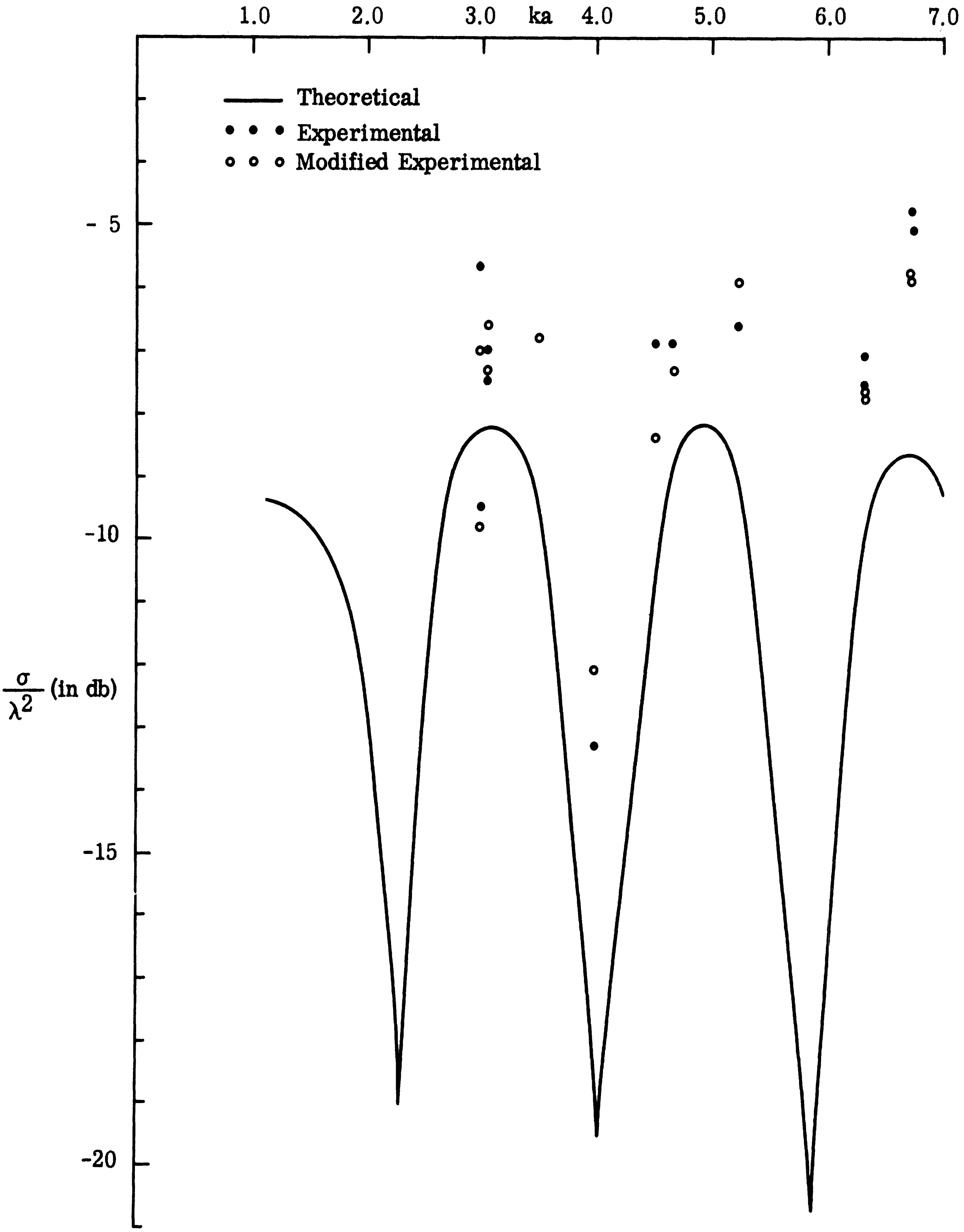

FIG. 3-3: NOSE-ON UNCOATED CONE-SPHERE CROSS SECTIONS.

In Fig. 3-4 the experimental nose-on cross sections are compared with the theoretical prediction in which the creeping wave has been enhanced by the theoretically derived factor. The form of presentation here is the more normal one of $\sigma/\pi a^2$ vs ka. Bearing in mind the asymptotic nature of the expression for the enhancement factor, and the known failure of the expression for small ka, the cross section assuming no enhancement of the creeping wave has been computed for the lower end, $2.5 < ka < 3.2$, of the desired range. The broken curve for $3.2 < ka < 3.8$ indicates a possible transition between the two formulae. We note that the resulting curve for the entire range $2.5 < ka < 7.5$ is in good agreement with the measured data.

For most of the measured patterns, the magnitudes of the left and right specular flashes are in excellent agreement with one another. In general the discrepancies are less than 1 db, but in one case (pattern No. 3946) there is a difference of 2.7 db. The magnitudes of the measured flash cross sections σ/λ^2 are plotted in Fig. 3-5, and compared with the physical optics value

$$\sigma/\lambda^2 = K(ka)^3 \tag{3.4}$$

where

$$K = \frac{\operatorname{cosec}^2\alpha \sec\alpha}{9\pi^2} \tag{3.5}$$

(Senior, 1966). Based on studies of measured data for right circular cones, an empirical correction factor to the theoretical value (3.4) has been derived, and for $\alpha = 7\text{-}1/2^{\circ}$, this factor is given in Fig. 8b of Senior (1966). The "corrected" theoretical behavior is shown as the broken curve in Fig. 3-5. It will be observed that the two curves bracket most of the experimental data.

Coated Cone-Spheres. The back scattering cross sections of six coated cone-spheres were measured at several frequencies spanning the range 2.53 - 8.43 Gc. The models used, together with their internal (metal) radii a and external (surface) radii b are as follows. The material of the coating is indicated in the last column.

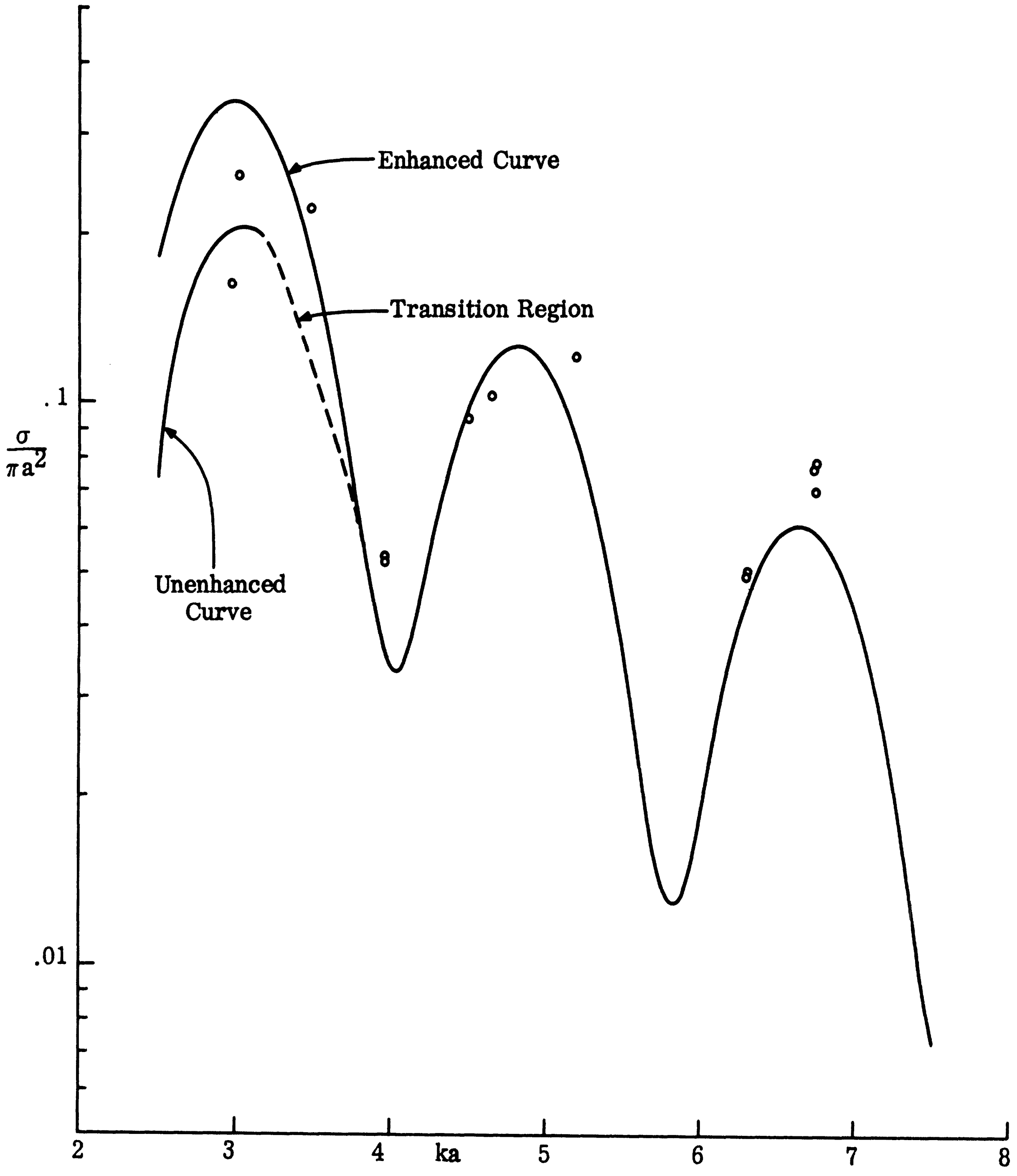

FIG. 3-4: COMPARISON OF THEORETICAL ENHANCED CROSS SECTION WITH MEASURED DATA.

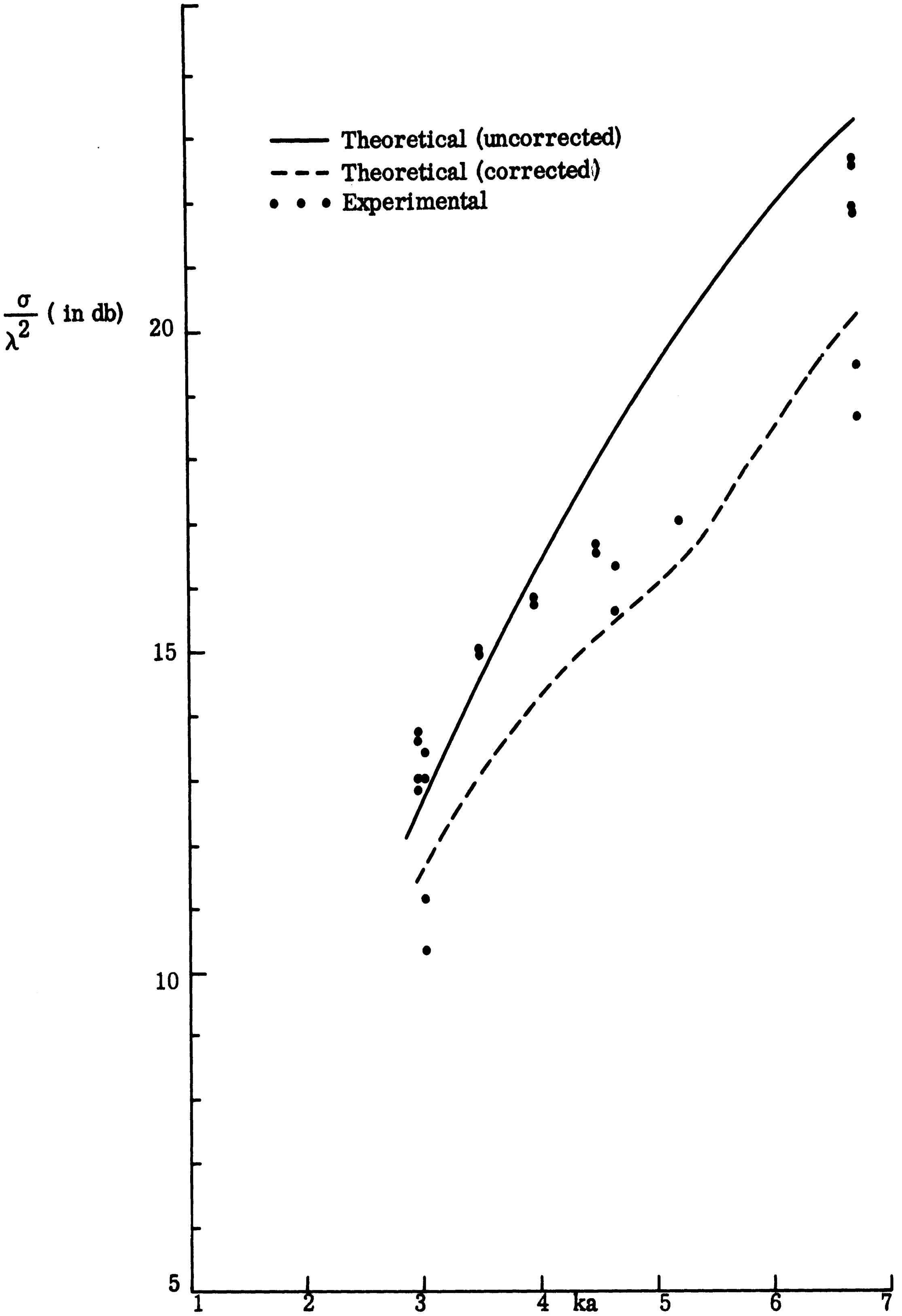

FIG. 3-5: SPECULAR FLASH UNCOATED CONE-SPHERE CROSS SECTION.

D-7	a = 1.500 in.	b = 1.839 in.	LS-22
D-8	a = 2.210 in.	b = 2.498 in.	LS-22
D-9	a = 2.210 in.	b = 2.498 in.	LS-26
D-10	a = 1.500 in.	b = 1.692 in.	LS-26
D-11	a = 1.500 in.	b = 1.692 in.	LS-24
D-12	a = 2.210 in.	b = 2.428 in.	LS-24

The cross sections in the nose-on and specular flash directions were again read from the measured patterns, and compared with the theoretical values associated with metal cone-spheres of the same outer radius. In Fig. 3-6 the ratios of measured specular flashes to the theoretical values derived from (3.4) with a replaced by b are plotted as functions of kb. The somewhat irregular nature of the results would seem to indicate a variation of the behavior of the material with changing frequency (and, hence, kb) and, in particular, the peaks in the data for all three coatings for kb near 5.0 are suggestive of a resonance effect in the coating.

For the nose-on direction a meaningful comparison with the results for metallic bodies is more difficult to perform owing to the rapid variation of the cross sections for each body as a function of frequency, and to the fact that the period of the oscillation is affected by the <u>material</u> of the coating and not merely by the outer dimension of the body. The measured values of σ/λ^2 for the six coated models are listed in Table III-1, and when these are compared with the cross sections of the uncoated cone-spheres of base radius b, the characters of the two curves are sufficiently distinct to make questionable the usefulness of the comparison. For completeness, however, the results are given, and in Fig. 3-7 the measured data points are superimposed on the theoretical curve, for the nose-on cross section σ/λ^2 of a metal cone-sphere of the same outer radius. For simplicity the formula has been computed without any enhancement of the creeping wave contribution. The agreement is at best qualitative, but is still somewhat better than if the theoretical curve for a cone-sphere of radius a had been employed.

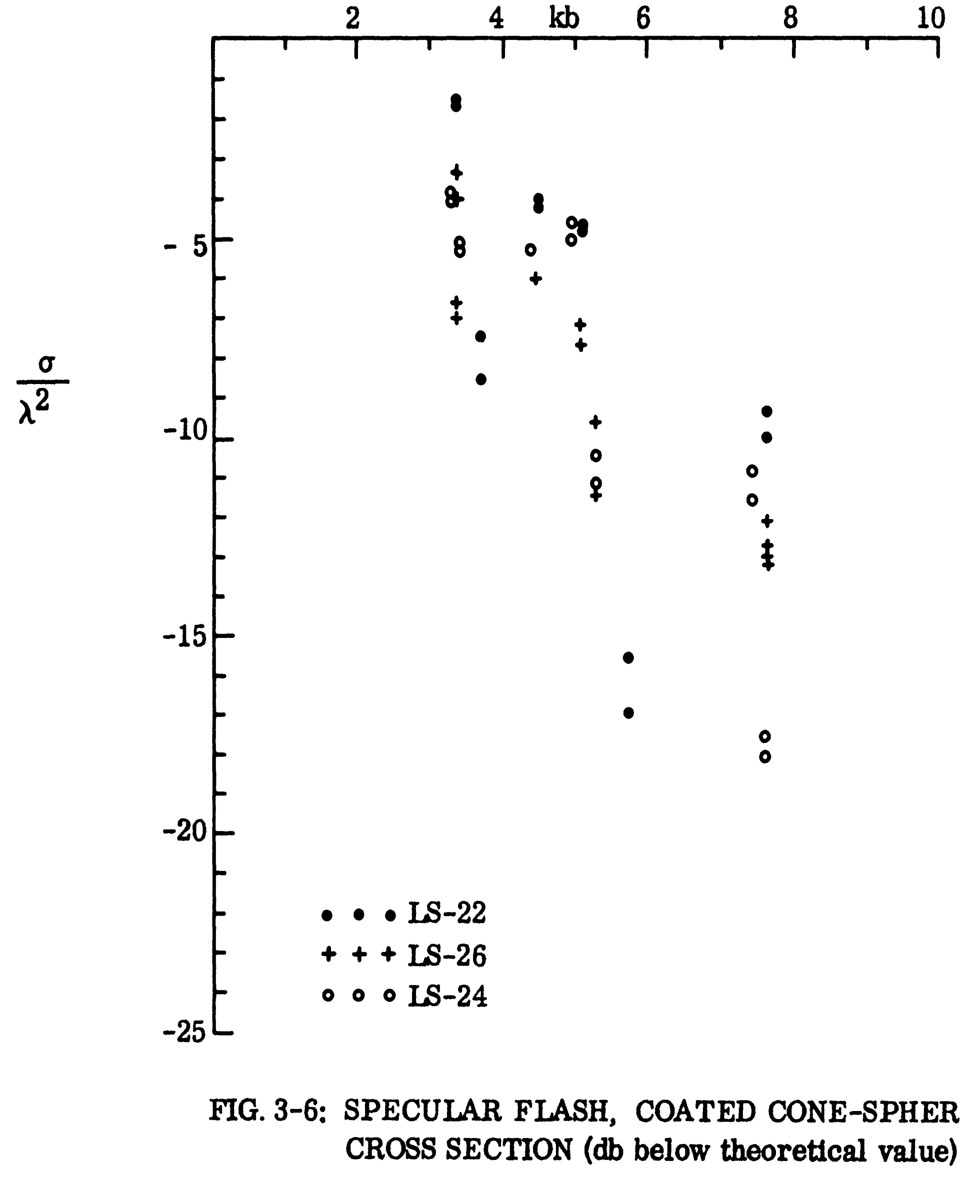

FIG. 3-6: SPECULAR FLASH, COATED CONE-SPHERE CROSS SECTION (db below theoretical value).

TABLE III-1: EXPERIMENTAL NOSE-ON COATED CONE-SPHERE CROSS SECTION

Freq (Gc)	Model	kb	σ/λ^2 (db)	Model	kb	σ/λ^2 (db)	Model	kb	σ/λ^2 (db)
2.53	D-8	3.3644	- 8.2	D-9	3.3644	- 4.0	D-12	3.2700	- 7.0
3.37	D-8	4.4814	-16.0	D-9	3.4814	-17.7	D-12	4.3558	-12.9
3.77	D-7	3.6908	-16.4	D-10	3.3957	-11.5	D-11	3.3957	-10.8
3.83	D-8	5.0931	-26.0	D-9	5.0931	-11.8	D-12	4.9504	-11.8
5.73	D-8	7.6197	-14.1	D-9	7.6197	-10.7	D-12	7.4062	-19.1
5.83	D-7	5.7075	-22.9	D-10	5.2513	-15.9	D-11	5.2513	-15.8
8.43	D-7	8.2528	-18.9	D-10	7.5931	+	D-11	7.5931	-18.9

+Data off-scale.

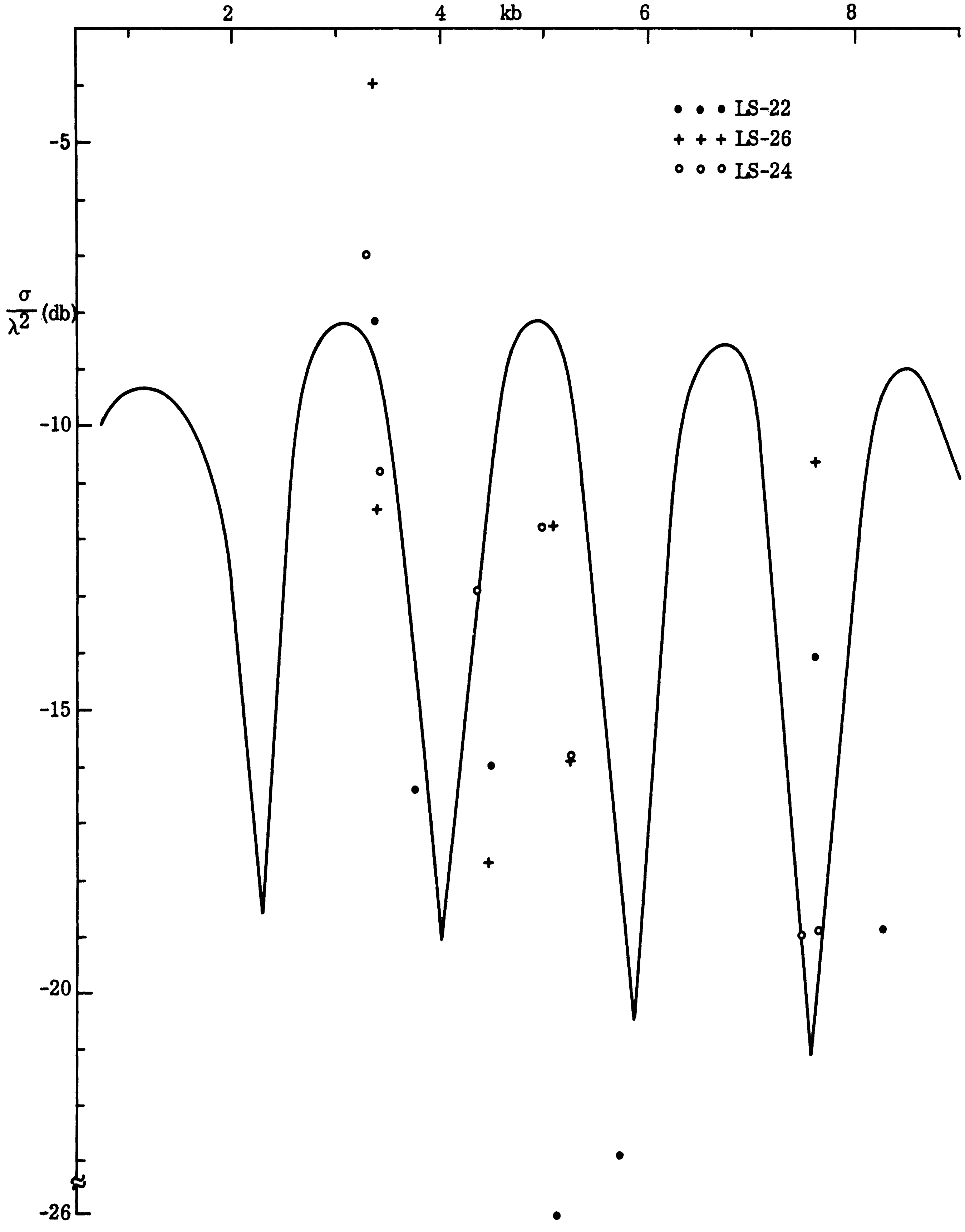

FIG. 3-7: NOSE-ON CROSS SECTIONS VERSUS kb (b= metal + coating radius).

B. 3 Preliminary Analysis of Back Scatter Data for the Nose-Tip Antenna Model

A set of measurements of the back scattering cross sections was made of a modified metallic cone-sphere. The half-angle was 7 1/2° and the back scattering was measured for horizontal polarization of the incident field for a 360° span of incident angles as the model was rotated about a vertical axis. The nose-on and the right- and left-side specular flash cross sections were determined from the curves. In addition, the nose-on lobe half-width (defined as that angular displacement either side from nose-on, $\theta=0^{\circ}$, where the cross section has dropped 10 db from its nose-on value) was obtained from the data.

The nose-tip antenna model consists of a metallic cone-sphere of base radius 2.210" out of which a segment 1/4" thick centered 3 3/8" from the tip has been deleted and replaced by a Lucite insert of the same dimensions. The backscattering patterns were measured at four values of the frequency: 2.53, 3.37, 3.83 and 5.73 Gc, corresponding to values of ka = 2.98, 3.96, 4.51 and 6.74 respectively.

For the two lowest frequencies visual comparison of the scattering patterns with those for a pure metallic cone-sphere of the same ka shows a large measure of similarity, the patterns being virtually indistinguishable except at aspects near nose-on where the nose-tip antenna model's lobe structure shows departures from the simpler model. However, for most other aspect angles the agreement is very good and even the specular flash cross sections agree within ± 0.5 db with those measured for the cone-sphere.

For the two highest frequencies the situation is less clear-cut. Although the specular flash cross sections agree within (about) ± 1.5 db with those of the pure metallic cone-sphere, and although the general levels as well as the lobe structure are comparable for aspect angles $90^{\circ}-\alpha \leq \theta \leq 180^{\circ}$, the similarity is not as great as formerly. In addition, the nose-tip antenna model's nose-on cross sections are about 4 db greater than for the cone-sphere and the nose-on lobe structure shows far less similarity.

Tables III-2 and III-3 list some of the relevant data for the nose-tip antenna and the cone-sphere models respectively, with the latter taken from the previous discussion "Backscattering from Uncoated and Coated Cone-spheres".

TABLE III-2: NOSE-TIP ANTENNA MODEL BACK SCATTER DATA

Pattern No.	Freq. (Gc)	ka	Measured Cross Section (σ/λ^2, db) Nose-on	Specular Flash Left	Specular Flash Right	Nose Lobe Half-width (degrees)
3967	2.53	2.98	-10.0	+12.7	+12.5	24
3976	3.37	3.96	- 9.3	+16.6	+16.4	17
3983	3.83	4.51	- 0.5	+18.4	+18.1	19
3965	5.73	6.74	- 2.2	+23.3	+23.6	37

TABLE III-3: PURE METALLIC CONE-SPHERE BACK SCATTER DATA

Pattern No.	Freq.	ka	Measured Cross Section(σ/λ^2, db) Nose-on	Specular Flash Left	Specular Flash Right	Nose Lobe Half-width (degrees)
3970	2.53	2.98	- 9.5	+13.0	+12.8	22
3905	2.53	2.98	- 5.7	+13.7	+13.6	20.5
3898	3.37	3.96	-12.9	+16.0	+16.1	27
3904	3.83	4.51	- 8.4	+16.5	+16.5	25.5
3903	3.83	4.51	- 6.9	+16.6	+16.5	21.5
3891	5.73	6.74	- 4.3	+22.2	+22.1	12
3892	5.73	6.74	- 5.1	+22.5	+22.6	11

By comparing the nose-on back scattering cross sections of the nose-tip antenna model with those of the corresponding cone-sphere, it is possible to deduce the maximum and minimum values of the additive cross section attributable to the spacer on the assumption that the other major contributors to the cone-sphere return are unaffected. The resulting bounds on $\sigma_{sp.}$ are as follows:

Freq. (Gc)	ka	ka_s	$\frac{\sigma_{\text{nose tip}}}{\sigma_{\text{cone-sphere}}}$ (in db)*	A		$\sigma_{sp}/\pi a_s^2$ min	max
2.53	2.98	0.60	-2.4	0.241	1.759	0.388	20.62
3.37	3.96	0.79	+3.6	0.514	2.514	0.273	6.53
3.83	4.51	0.90	+7.1	1.265	3.265	4.07	28.8
5.73	6.74	1.35	+2.5	0.334	2.334	0.262	12.8

where a_s = radius of the tip side of the Lucite spacer insert and the asterisk (*) for the cone-sphere measurements refers to the fact that an average of the two measured nose-on cross sections (listed in Table III-3) was used.

B. 4 A Preliminary Analysis of the Radar Backscattering from Model ID-1

A set of measurements was made of the radar cross section of the shallowest of the ID models. These models are cone-spheres with the spherical rear termination modified by a concavity in the rear termination. The termination is then representative of the re-entry vehicle typified by the Mark 12 vehicle. The half-angle of the model is 7 1/2°. The backscattering was measured for the horizontal polarization of the incident field for a 360° span of the incident angles as the model was rotated about a vertical axis. The nose-on and right- and left-side specular flash cross sections were determined from the measured data. In addition, the nose-on lobe half-width (defined as the angular displacement either side from nose-on where the cross section has dropped 10 db from its nose-on value) was obtained from the data.

Model ID-1 consists of a metallic cone-sphere of base radius 2.210", the rear spherical cap of which has a concave indentation formed by the removal of a spherical portion of radius 4.588" centered on the cone axis to the rear of the antipode. This model is illustrated in Fig. 2-5. In order that the concave indentation will have a continuous tangent at the intersection with the remaining cone-sphere surface, the portion of the surface between the cone-sphere join and the concavity is now a portion of a torus whose inner radius is 0.553". Backscattering measurements were made at the same four frequencies as the nose-tip antenna model (i.e. 2.53, 3.37, 3.83 and 5.73 Gc) and the associated values of ka are also equal: 2.98, 3.96, 4.51 and 6.74.

Visual inspection of the data does not reveal the same degree of similarity between patterns for ID-1 and those of the cone-sphere , but some correspondence remains. The nose-on cross section is down by 3 db at the lowest frequency (2.53 Gc) but at each of the others it is increased by from 4 - 8 db. The specular flash cross sections, however, are quite comparable: for three of the frequencies, the ID-1 values are within ± 1 db of those of the cone-sphere, and even for the fourth (3.83 Gc) the ID-1 cross sections are within ± 2 db of the cone-sphere. As one might expect, the concave back indentation considerably alters the scattering patterns at angles of incidence beyond the specular flash. Table III-4 lists some of the deduced values for Model ID-1 in more detail.

TABLE III-4: MODEL ID-1 BACK SCATTER DATA

Pattern No.	Freq. (Gc)	ka	Measured Cross Sections (σ/λ^2, db)			Nose-lobe Half-width (degrees)
			Nose-on	Specular Flash Left	Specular Flash Right	
3969	2.53	2.98	-11.8	+14.3	+14.1	8
3978	3.37	3.96	- 4.8	+17.1	+16.8	23
3980	3.83	4.51	- 3.6	+18.8	+18.3	13
3963	5.73	6.74	- 0.4	+23.0	+23.3	15

At this point it is perhaps pertinent to note that a direct comparison of the nose-on back scattering cross sections for Model ID-1 (Table III-4) and for a cone-sphere (Table III-3) must be made with some caution. If the nose-on cross section of a pure cone-sphere is at or near a relative minimum for a particular value of ka, it is entirely possible (by a mere change in the relative phase of the major contributors, without any significant change in their magnitudes), to effect a substantial increase in the back scattering cross section. In particular, this may explain some or all of the increase of 8.1 db observed in the measured cross section of Model ID-1 relative to a cone-sphere at the frequency of 3.37 Gc and, indeed, a phase difference in the creeping wave component is to be expected due to the indented back of Model ID-1.

3.1.2 Effect of Surface Perturbations

The effect on radar cross section of perturbations of the surface caused by flush mounted slot antennas, nose-tip antennas and concavities in the rear of the re-entry vehicle is being investigated. The concave surface work is reported in the discussion under Task 3.1.5.

The effect of slot antennas is being approached by modelling the slot by dipoles or loops. A preliminary theoretical analysis of the scattering by small obstacles such as dipoles and loops mounted on a perfectly conducting plane is discussed in the following pages. A more detailed Technical Report is being written and an abstract of the report is given at the end of this analysis.

A. Scattering by Small Obstacles Mounted on a Perfectly Conducting Plane.

A.1 Monopole Above an Infinite, Perfectly Conducting Plane.

The scattered field of a monopole in the region above a perfectly conducting plane can be obtained by using image theory. Figure 3-8 displays a plane wave incident at angle θ_i. The boundary condition $n \times \underline{E} = 0$ on the plane can be reproduced when the conducting plane is removed by an image wave coming from below at angle $\pi - \theta_i$. The image wave in the region above the plane is then identified as the reflected wave. The field above the plane can be obtained by placing an image monopole symmetrically below the plane and calculating the field of a dipole of twice the monopole

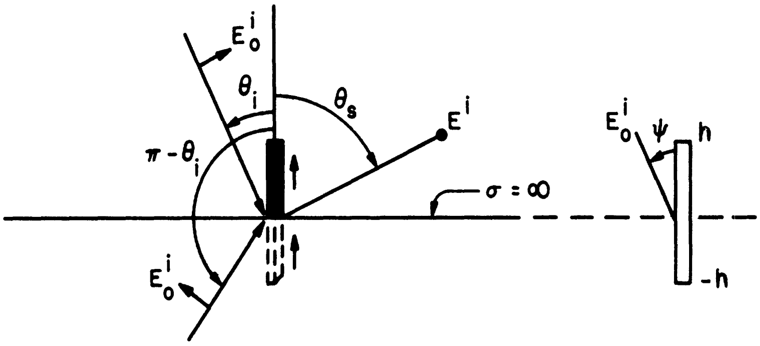

FIG. 3-8: MONOPOLE ABOVE CONDUCTING PLANE.

length in free space, i.e.

$$E^s(\theta_s)=E_i(\theta_i)R(\theta_i,\theta_s)+E^i(\pi-\theta_i)R(\pi-\theta_i,\theta_s) \qquad (3.6)$$

where $R(\theta_i,\theta_s)$ is the bistatic reflection coefficient of a dipole which transforms an incident field at θ_i to a scattered field at θ_s.

When a cylindrical wire is located along the z-axis and a plane wave is incident at an arbitrary angle θ_i the tangential component of the incident electric field on the surface of the cylinder is

$$E^i_z = E_o \cos\psi \sin\theta \, e^{-jkz\cos\theta + j\omega t} \qquad (3.7)$$

where E_{io} makes an angle ψ with the plane containing the incidence direction and the axis of the wire . Introducing this value of E^i_z in the expression for the scattered field vector potential will yield to the usual integro-differential equation. This equation can be solved for by variational or iterative procedures. The current distribution depends on k and θ, but its dependence on ψ is simply that of $\cos\psi$. In general, the current along a dipole with end points at $z = \pm h$ that is used as a transmitting antenna is well approximated by a sinusoidal distribution. However, the same dipole used as a receiving antenna has a current distribution that varies with the direction of the incident wave and is usually different from sinusoidal unless it is of resonant length. At oblique incidence the induced current does not have symmetry with respect to the center of the wire. When a plane wave is used to excite a wire there is a phase shift along the antenna as the incident wave passes. Only for broadside incidence where the E vector is parallel to the wire are all points of the wire excited in equiphase. For broadside incidence the current is symmetric, i.e. $I_z(d)=I_z(-d)$. For arbitrary incidence a symmetric as well as an asymmetric current $I_z(d)=-I_z(-d)$ is excited in the antenna. Since these induced currents radiate, the scattered far-zone fields produced by them are (King, 1956)

$$E_\theta = \frac{j\omega\mu_o}{4\pi}\sin\theta_s \frac{e^{-j\beta R_o}}{R_o}\int_{-h}^{h}\left[I^s(z')+I^a(z')\right] e^{j\beta z'\cos\theta_s} dz' \quad . \qquad (3.8)$$

The current most go to zero at the end points: I ($\pm$h)=0. This also implies that the symmetric or asymmetric part alone must vanish at the ends of the wire. For example, on a cylinder with resonant length ($h \approx \lambda/4$) the symmetric component of the induced current dominates, whereas for cylinders with antiresonant length ($h \approx \lambda/2$) the asymmetrical current dominates. The asymmetric current is also characterized by a zero at the center of the wire, whereas the symmetric component has a maximum there.

For wires small with respect to wavelength the incident wave cannot produce enough phase shift as it travels past the wire to excite an asymmetrical component of current. Hence for small wires the current induced by a plane wave at arbitrary angles of incidence is predominantly symmetric. We therefore conclude that for dipoles not much longer than $2h=\lambda/2$ the symmetric current excited by an incident field from any direction predominates. In general this current is well approximated by a triangular distribution for short antennas, a sinusoidal distribution for resonant antennas, and a constant distribution for long antennas. The dependence on the incident wave is simply $E_0^i \cos \psi \sin \theta$, which has been experimentally verified (King, 1956; Chen and Liepa, 1964) for receiving and transmitting antennas. Such studies also indicate that for antennas such as the short dipole and the half-wave dipole the receiving and transmitting currents of the antennas are nearly identical.

A. 2 Resonant and Short Dipoles

Assuming a symmetric sinusoidal current

$$I=I_m \begin{cases} \sin\left[k(h-z)\right] & z > 0 \\ \sin\left[k(h+z)\right] & z < 0 \end{cases} \qquad (3.9)$$

is induced in the wire and that the asymmetric component is zero (we will confine ourselves to wire length $h < \lambda/4$), equation (3. 8) becomes, after integration

$$E_\theta = \frac{j\eta I_m}{2\pi r}\, e^{-jkr} \left[\frac{\cos(kh\cos\theta_s)-\cos kh}{\sin\theta_s}\right] \tag{3.10}$$

where $\eta = \sqrt{\mu/\epsilon} = 120\pi\,\Omega$ for free space. Total $\underline{E}$ and $\underline{H}$ at long distances from the antenna are at right angles to each other and the direction of propagation, in time phase, and related by η, i.e. $E_\theta = \eta H_\phi$.

Assuming a triangular current distribution

$$I = I_m \begin{cases} k(h-z) & z > 0 \\ k(h+z) & z < 0 \end{cases} \tag{3.11}$$

we obtain

$$E_\theta = \frac{j\eta I_m}{2\pi r}\, e^{-jkr} \tan\theta_s \sec\theta_s \left[1-\cos(kh\cos\theta_s)\right] . \tag{3.12}$$

In the limit of $kh \ll 1$, (3.10) and (3.12) yield

$$E_\theta = \frac{j\eta I_m}{4\pi r}\, e^{-jkr} (kh)^2 \sin\theta_s \quad . \tag{3.13}$$

In the last expression one should note that the assumed current is $I = I_m kh(1-|z|h)$.

If more accurate (but still approximate) solutions to the induced currents are desired, the methods of Chen and Liepa (1964), King (1956), Tai (1952), Harrison and Heinz (1963), Harrison (1962), Vainshtein (1959) and Ufimtsev (1962) can be used.

Now we must relate the magnitude of the current I_m to the incident field. This will be done by applying the law of conservation of energy as follows. The total energy radiated by the induced currents in the antenna can be computed by integrating over a closed surface which coincides with the antenna surface or alternately, choosing a surface of a large sphere of radius R. Equating these two expressions a solution for I_m is obtained.

The tangential component of the incident field is given by (3.7). Since the total tangential field is composed of the incident and the induced field, and since this field must be zero on the surface of the wire we have

$$E_{total} = E^i + E_{ind} = 0$$

which gives for the induced field

$$E_{ind} = -E^i \tag{3.14}$$

The energy radiated from the antenna is

$$W = \frac{1}{2} \mathrm{Re} \int_{-h}^{h} \underline{E} \cdot I^* dz$$

$$= -\frac{1}{2} \mathrm{Re} \int_{-h}^{h} E_0 \sin\theta_i \cos\psi \, e^{jkz\cos\theta_i} I_m \sin k(h-|z|) dz$$

$$= -\frac{1}{2} E_0 \sin\theta_i \cos\psi \, I_m \int_{-h}^{h} \cos(kz\cos\theta_i) \sin k(h-|z|) dz \tag{3.15}$$

for a sinusoidal antenna current. Performing the integration we obtain

$$W=E_o\cos\psi I_m\,\frac{\cos(kh\cos\theta_i)-\cos kh}{k\sin\theta_i}\quad . \tag{3.16}$$

Recalculating the power radiated by the Poynting method we have

$$W=\oiint \underline{P_r}\cdot\underline{dA}=\oiint\frac{1}{2}\left|E_\theta\right|\left|H_\phi\right|\,dA=\frac{\pi}{\eta}\int_0^\pi\left|E_\theta\right|^2r^2\sin\theta\,d\theta\ . \tag{3.17}$$

Using (3.10) for E_θ, (3.17) becomes

$$W=\frac{\eta I_m^2}{4\pi}\int_0^\pi\frac{\left[\cos(kh\cos\theta)-\cos kh\right]^2}{\sin\theta}\,d\theta\quad . \tag{3.18}$$

Equating this to (3.16) we can solve for I_m

$$I_m=\frac{4\pi\,E_o\cos\psi\,(\cos kh\cos\theta_i-\cos kh)}{\eta k\sin\theta_i\displaystyle\int_0^\pi\frac{\left[\cos(kh\cos\theta)-\cos kh\right]^2}{\sin\theta}\,d\theta}\quad . \tag{3.19}$$

The integration when performed yields

$$C=\int_0^\pi\cdots=.5772\ldots+\ell n\,2kh-Ci(2kh)+\frac{1}{2}\sin 2kh\left[Si(4kh)-2Si(2kh)\right]+$$

$$+\frac{1}{2}\cos 2kh\left[.5772+\ell n\,kh+Ci(4kh)-2Ci(2kh)\right]\quad , \tag{3.20}$$

where the sine and cosine integrals

$$\mathrm{Si}(x) = \int_0^x \frac{\sin x}{x}\, dx \quad .$$

$$\mathrm{Ci}(x) = -\int_x^\infty \frac{\cos x}{x}\, dx$$

are tabulated.

The scattered field is then

$$E_\theta^s = j2E_0 \cos\psi \, \frac{\cos(kh\cos\theta_i)\cos kh}{\sin\theta_i} \cdot \frac{\cos(kh\cos\theta_s) - \cos kh}{\sin\theta_s} \, \frac{e^{-jkr}}{Ckr} \, . \qquad (3.21)$$

A. 3 Dipoles Short with Respect to Wavelength

For small kh (3. 21) becomes

$$\lim_{kh \to 0} E_\theta^s = j3E_0 \cos\psi \sin\theta_i \sin\theta_s \, \frac{e^{-jkr}}{2kr} \quad . \qquad (3.22)$$

It is apparent that this does not give the correct kh dependence in the limit. The trouble arises from the following: In the emf approach to the power calculation (3. 15), it was assumed that the induced current is in phase with the forcing incident field. This is a valid assumption for resonant wire length. However, short dipoles are capacitive, i. e. the induced current leads the voltage by 90°. This can be easily seen from the near field expression for a Hertzian dipole which is

$$E_\theta = \frac{-j\eta I d\ell \sin\theta}{4\pi kr^3}\, e^{-jkr} \quad . \qquad (3.23)$$

Let us then assume a triangular current which for short dipoles has the form

$$I=I_o\left(1-\frac{|z|}{h}\right)\exp\left\{j\left[\frac{\pi}{2}-(kh)^n\right]\right\} \tag{3.24}$$

where n is an integer yet to be determined. This current has the correct behavior, namely when $kh \to 0$, $I=jI_o\left(1-\frac{|z|}{h}\right)$, i.e. current leads the voltage by $\pi/2$. Using this current in the emf calculation for power (3.15) we obtain

$$W=\frac{1}{2}\operatorname{Re}\int_{-h}^{h} E_0\sin\theta_i\cos\psi\, e^{jkz\cos\theta_i}\, I_o^*\left(1-\frac{|z|}{h}\right)\exp\left\{-j\left[\frac{\pi}{2}-(kh)^2\right]\right\}dz$$

$$=\frac{1}{2}E_0\sin\theta_i\cos\psi\, I_o^*\int_{-h}^{h}\cos(kz\cos\theta_i)\left(1-\frac{|z|}{h}\right)(kh)^n dz$$

$$=E_0\sin\theta_i\cos\psi\, I_o^*\left[1-\cos(kh\cos\theta_i)\right]\frac{(kh)^n}{k^2h\cos^2\theta_i}=\frac{1}{2}E_0\sin\theta_i\cos\psi\, I_o^*\, h(kh)^n\,. \tag{3.25}$$

The radiated far field from a short wire with an assumed triangular current distribution as in (3.24) is from (3.13)

$$E_\theta=\frac{j\eta kh\sin\theta_s}{4\pi r}I_o\exp\left\{j\left[\frac{\pi}{2}-(kh)^n-kr\right]\right\}\quad. \tag{3.26}$$

The radiated power using the Poyntings method (3.17) is then

$$W=\frac{\pi}{\eta}\int_0^{\pi}\left|E_\theta\right|^2 r^2\sin\theta_s d\theta_s=\frac{\eta k^2h^2}{12\pi}I_oI_o^*\quad. \tag{3.27}$$

Equating (3.27) and (3.25) we obtain for the current

$$I_o=\frac{6\pi E_o\sin\theta_i\cos\psi\,(kh)^n}{\eta k^2h}\quad. \tag{3.28}$$

Therefore, the scattered field using (3.26) is

$$E_\theta^s = j3E_0 \cos\psi \sin\theta_i \sin\theta_s (kh)^n \; \frac{\exp\left\{j\left[\frac{\pi}{2} - (kh)^n - kr\right]\right\}}{2kr} \; . \tag{3.29}$$

In order to determine n we need another condition. To avoid a lengthy discussion, let us use an expression for the back scattering cross section for small kh as given by Van Vleck, Bloch and Hamermesh (1947) and Mack and Reiffen (1964)

$$\sigma = \frac{\lambda^2 (kh)^6 \cos^4\psi \sin^4\theta}{9\pi \left[\log 4h/a - 1\right]^2} \; . \tag{3.30}$$

This expression is valid for $kh < .3$ and $ka \ll 1$, where a is the radius of the wire. It becomes more accurate as the ratio h/a gets larger. In any case this ratio should be chosen such that $2h/a > 100$. Using (3.28), n is established as $n = 3$, and the scattered field as

$$E_\theta^s = \frac{E_o k^3 h^3 \cos\psi \sin\theta_i \sin\theta_s}{\log 4h/a - 1} \; \frac{e^{-jkr - j(kh)^3}}{kr} \; . \tag{3.31}$$

The $(kh)^3$ term in the phase can be ignored as being small.

That the kh dependence is correct can also be verified from recent results for the radiating antenna (King and Wu, 1965). For $kh \ll 1$ the current is found to be

$$I = \frac{j2\pi V_o^e}{\eta\psi(0)} kh \left(1 - \frac{|z|}{h}\right) \tag{3.32}$$

where $\psi(0)$ is a constant and V_o^e is the applied voltage $E_z = -V_o^e \, \delta(z)$ at the center of the antenna. It is here again seen that I and V are out of phase by 90°. For the scattering problem, V_o^e becomes the induced voltage due to the incident field as given by (3.7), i.e.

$$V_o^e = \int_{-h}^{h} E_o \cos\psi \sin\theta_i e^{-jkz\cos\theta_i} dz = E_o \cos\psi \sin\theta_i 2h \ . \qquad (3.33)$$

Using (3. 13), the scattered field then becomes

$$E_\theta^s = -\frac{E_o k^3 h^3 \cos\psi \sin\theta_i \sin\theta_s}{\psi(0)} \frac{e^{-jkr}}{kr} \qquad (3.34)$$

which agrees with (3. 31) above.

A. 4 Monopole over Perfectly Conducting Ground

The scattered field of a monopole of length h above a perfectly conducting plane can then be written using (3. 6) and (3. 21) as

$$E_\theta^s = 2E_\theta^s \quad \text{of} \ (3.21). \qquad (3.35)$$

The total electric field above the infinite plane is then given by the incident field, the image field and the scattered field. The image field is interpreted as the principal reflected wave from the plane in the absence of any obstacle. For example, when the E-vector is in the plane of incidence (ψ=0) which is taken as the zx plane, the total field for a short monopole is given by

$$\underline{E} = E_o(\cos\theta_i \hat{i} + \sin\theta_i \hat{k}) e^{jk(x\sin\theta_i - z\cos\theta_i)} + E_o(-\cos\theta_i \hat{i} + \sin\theta_i \hat{k}) \cdot$$

$$\cdot e^{jk(x\sin\theta_i + z\cos\theta_i)} - \frac{2E_o k^3 h^3 \sin\theta_i \sin\theta_s}{\log 4h/a-1} \frac{e^{-jkr}}{kr} \ . \qquad (3.36)$$

It can also be concluded that asymmetric currents are not excited in a monopole above ground. The induced currents are always symmetric, i. e. I(z)=I(-z). This comes about since the total tangential field at the wire due to the incident and image waves is an even function of z, i. e.

$$(E^{i}+E^{im})\hat{k}=\hat{k}2E_{o}\sin\theta_{i}\cos(kz\cos\theta_{i})e^{jkx\sin\theta_{i}} \quad . \qquad (3.37)$$

Since this tangential E field is the total forcing function for small dipoles we conclude that the induced currents are symmetric .

B. Technical Report on Scattering by Slots on a Conical Surface

A Technical Report on scattering by slots is being prepared. The report will cover two main subjects, 1) scattering from resonant slots on a cone and 2) scattering from a half-loop on a conducting plane. An abstract of the report is as follows:

B. 1 Scattering from Resonant Slots on a Cone.

The scattered field when a plane wave is incident along the axis of a slotted, perfectly conducting, semi-infinite cone is obtained by superposition of the scattered field from an unslotted cone and the radiation field from the slot on the cone. The slot is a finite, thin circumferential slot backed by a cavity which is characterized by an admittance. The induced voltage is represented by a sinusoidal distribution. The amplitude of the induced voltage is then related to the incident field by expressing it in terms of the radiating and load admittance of the slot. Expressions for the radiation admittance and the scattered far fields are derived. The case of a circumferential slot is a special case of this treatment.

B. 2 Scattering from a Half-loop on a Conducting Plane

It is shown that the scattered field from a small loop in free space can be identified with three dipole contributions. The equivalent scattering dipole moments which are induced by the incident field are expressed in terms of the loop geometry, the orientation and polarization of the incident wave. The scattered field of the loop shows a wavelength dependence which is $E^{s}\sim k^{2}d^{3}$.

Scattering for a half-loop, mounted on a conducting plane, is similar to that for the free space loop. The magnetic dipole field is not changed. The normal electric dipole contribution is present in altered form, but the electric dipole term which is parallel to the plane vanishes. These changes, in addition to identifying the image wave with the reflected field from the plane, account for the presence of the conducting plane and the arbitrary direction of incidence.

C. Surface Field Measurements of the Nose-tip Antenna Model.

The amplitude of the surface field component $H_\phi (\equiv J_s)$ has been measured for a plane wave at nose-on incidence on the nose-tip antenna model. This model is a metallic cone-sphere of half angle $7 \, 1/2^{\circ}$ and base radius 2.210", having a disk of Lucite 1/4" thick centered 3.375" from the tip (and therefore 13.412" from the join). The resulting tip and spacer are meant to simulate a nose-tip antenna.

Measurements were made at the four frequencies (0.935, 2.5499, 4.2499 and 6.799 Gc) corresponding to ka = 1.100, 3.000, 5.000 and 7.999 respectively, where a is the base radius of the cone-sphere. At these four frequencies the thickness in wavelengths of the spacer was 0.0198, 0.0540, 0.0900 and 0.1440 respectively and the distance in wavelengths along the surface of its center from the tip was 0.267, 0.729, 1.215 and 1.944 respectively. Only at the highest frequency were the measurements carried out over the whole cone-sphere; at the other frequencies probing was stopped at some point beyond the rear edge of the spacer, but well short of the cone-sphere join. The distance in wavelengths from the tip of the last probe position at 0.935, 2.5499 and 4.2499 Gc was 0.713, 1.944 and 1.620 respectively, compared with the values 1.330, 3.627 and 6.045 appropriate to the cone-sphere join.

The measured data for the portions of the cone-sphere up to and just beyond the spacer is shown in Figs. 3-9 through 3-12. Where available, the corresponding data for the pure cone-sphere is included, and is shown as a dashed line. The complete curve for the nose-tip antenna model with ka= 7.999 is presented in Fig. 3-13, and since no comparison curve for the pure cone-sphere with this value of ka was available from the earlier studies, the required measurements were made and the results are given in Fig. 3-14.

Comparison of Figs. 3-13 and 3-14 reveals that at distances beyond a wavelength (approx.) from the spacer, the curves are almost identical with one another. This is also apparent from Fig. 3-12 and indicates that beyond the spacer the surface field rapidly reverts to the values that it would have had if the spacer had not been present. In particular, the surface fields in the vicinity of the join and shadow boundary are unaffected by the spacer, and in consequence, the join and creeping wave contributions to the scattering are identical to those appropriate to a pure cone-sphere with this value of ka. Ahead of the spacer a significant oscillation of the surface field occurs, and this is clearly attributable to a backward-travelling wave originating at the spacer. The separation of adjacent maxima and minima in the oscillation shows that the interfering wave are travelling with velocities indistinguishable from that of light, with the amplitude of the backward-travelling wave decreasing somewhat with distance away from the spacer. Allowing for an apparent 5 per cent discrepancy in calibration evident from Figs. 3-13 and 3-14, the mean curve through the oscillations is close to the curve for the pure cone-sphere.

At the next smaller value of ka, ka=5, the conclusions are similar and, indeed, an examination of Fig. 3-11 shows that the field has reverted to its values for a pure cone-sphere within a small fraction of a wavelength past the spacer. Accordingly, the contributions to the backscattered field produced by the join and shadow boundary are again unaffected by the spacer. Whereas for ka=8 the field was at a minimum within the spacer, it now is at a maximum, and it is possible that this change may be due to the different electrical lengths of the spacer at the two wavelengths.

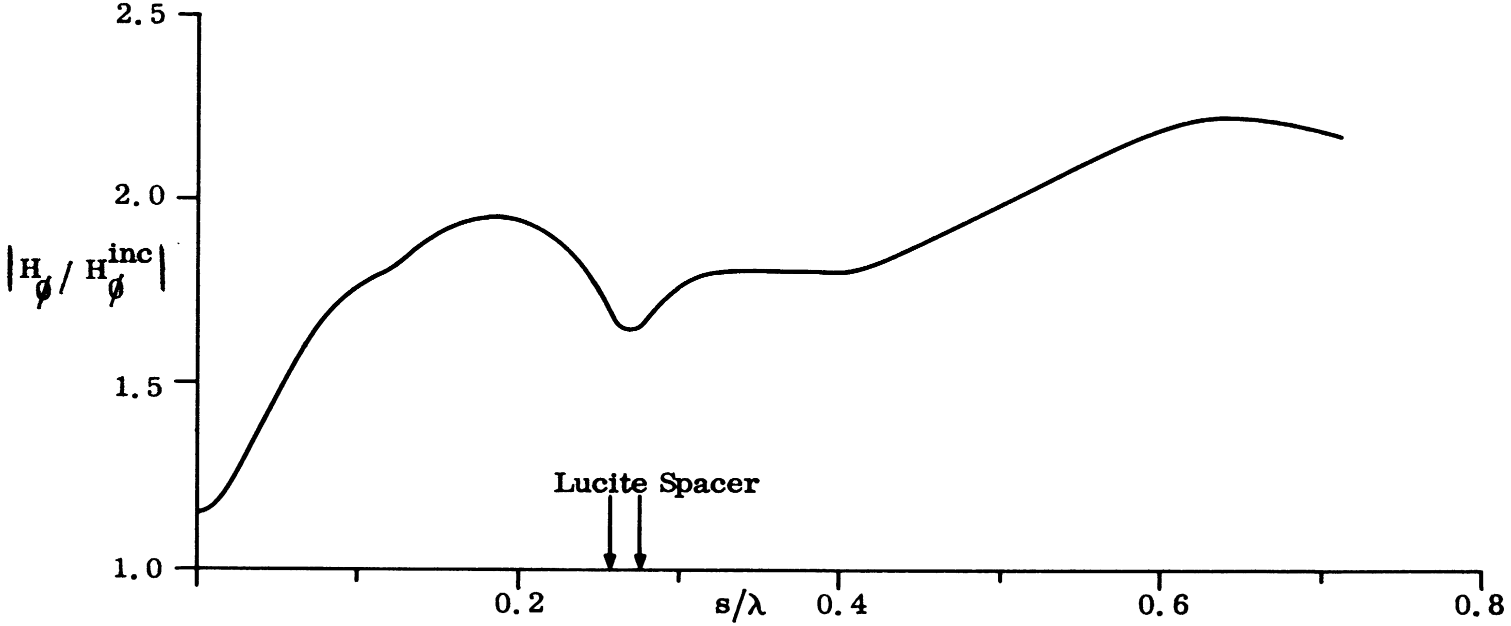

FIG. 3-9: SURFACE CURRENT FOR NOSE-TIP ANTENNA MODEL (ka=1.10).

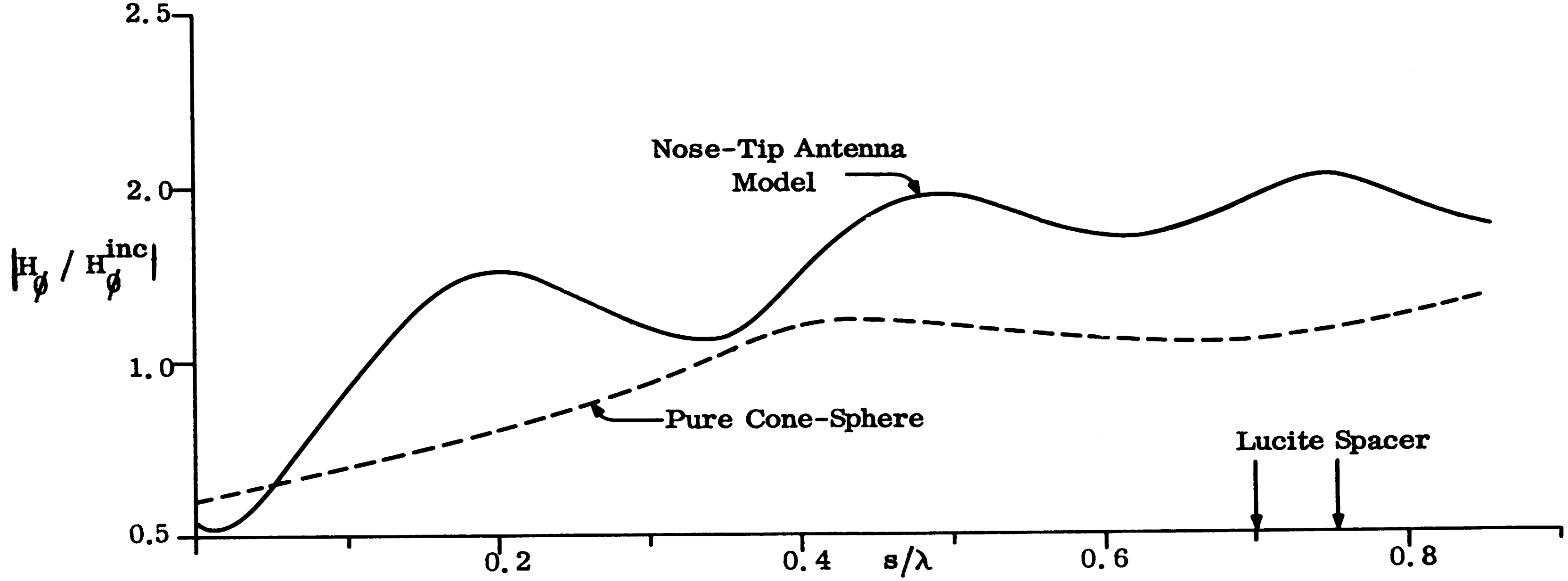

FIG. 3-10: COMPARISON OF SURFACE CURRENTS ON CONE-SPHERE MODEL WITH AND WITHOUT NOSE-TIP ANTENNA (ka=3.0).

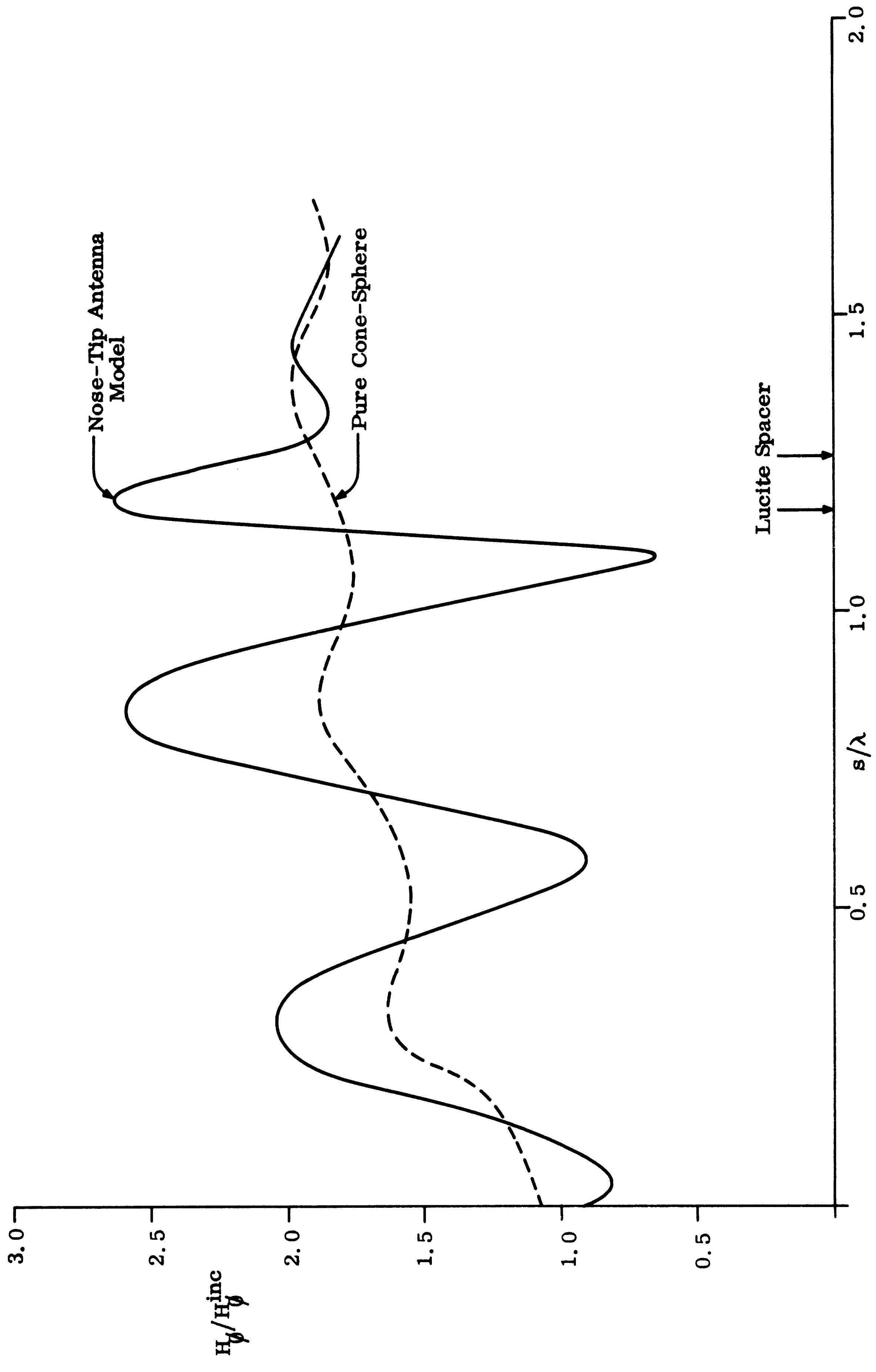

FIG. 3-11: COMPARISON OF SURFACE CURRENTS ON CONE-SPHERE MODEL WITH AND WITHOUT NOSE-TIP ANTENNA (ka=5.0).

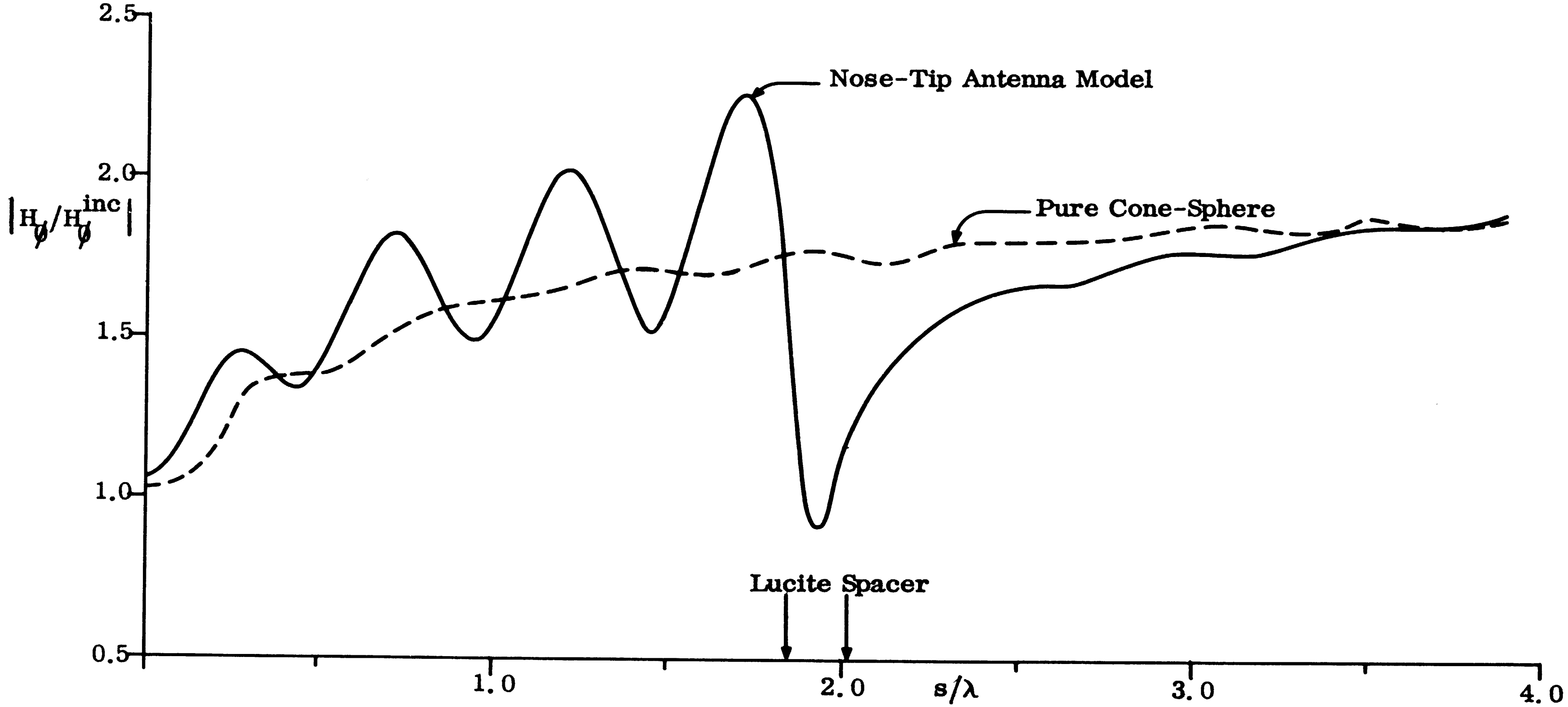

FIG. 3-12: COMPARISON OF SURFACE CURRENTS ON CONE-SPHERE MODEL WITH AND WITHOUT NOSE-TIP ANTENNA (ka=7.99).

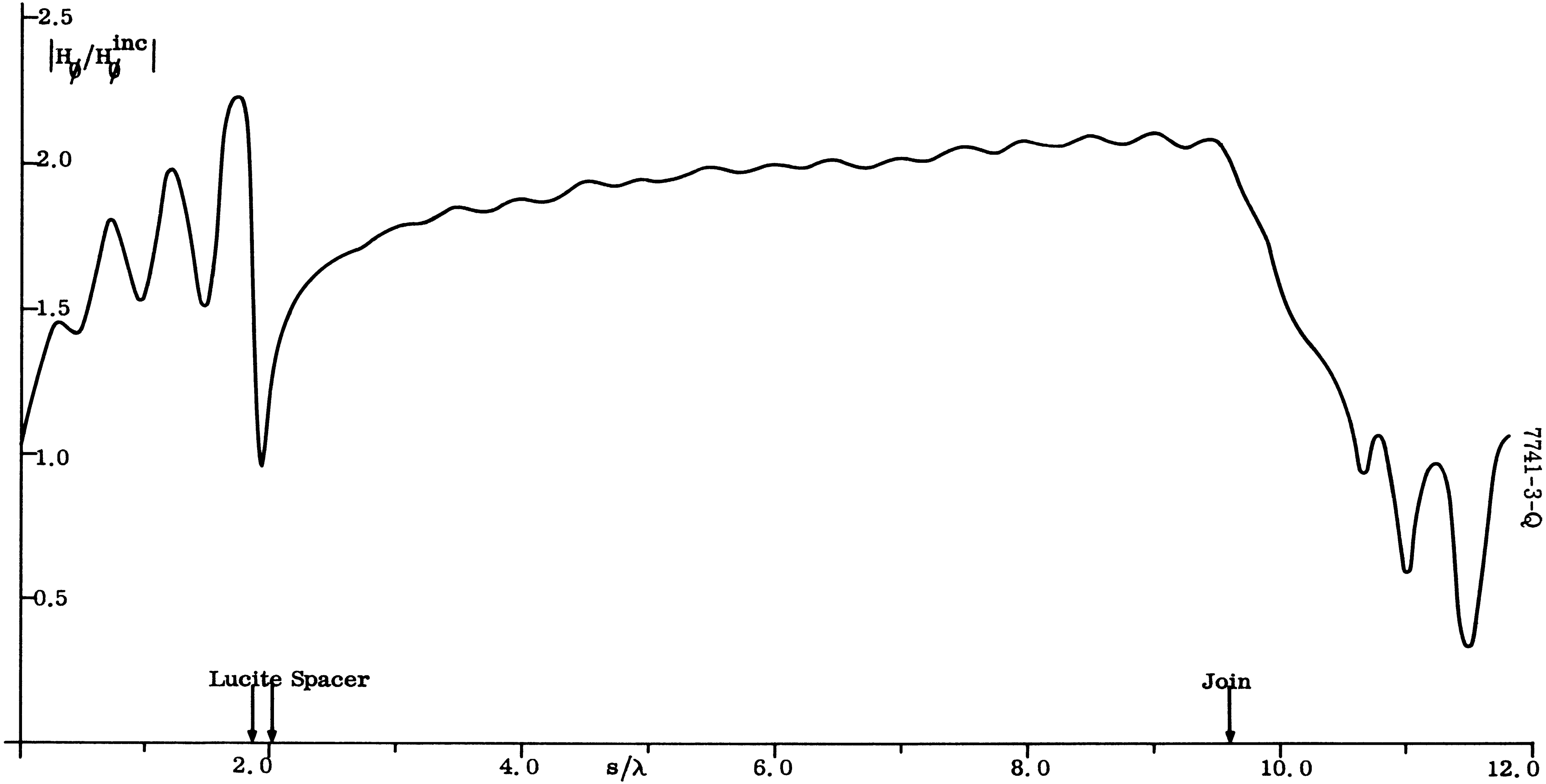

FIG. 3-13: SURFACE CURRENTS ON NOSE-TIP ANTENNA MODEL (ka=7.99).

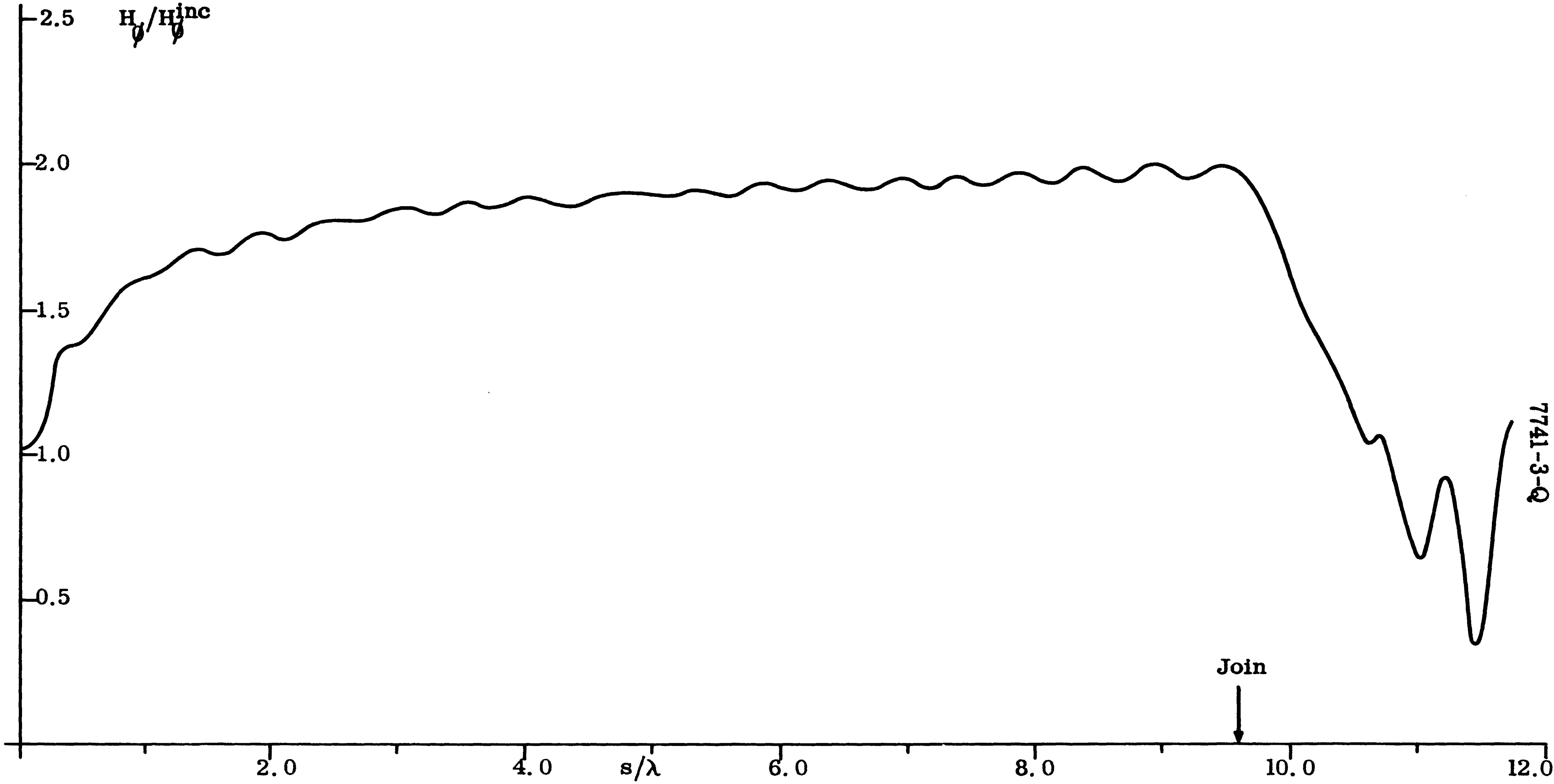

FIG. 3-14: SURFACE CURRENTS ON CONE-SPHERE WITHOUT NOSE-TIP ANTENNA MODEL (ka=7.99)

Thus, at the highest frequency (6.799 Gc) the circumferential length at the midpoint of the spacer (the lengths of the two edges of the spacer are less and greater by 3.7 per cent) is 1.595 λ, whereas at the next lower frequency (corresponding to ka = 5.0) the length is 0.997λ. We note in passing that at the other two frequencies the lengths are 0.598 λ and 0.219 λ. Thus, when ka = 5.0, the ring singularities formed by the edges of the spacer are almost precisely at resonance, and this fact is almost certainly responsible for the greater amplitude of oscillation forward of the join. Apart from this increase in amplitude, however, the characteristics of the oscillation are the same as they were for ka = 7.999.

At the two lower frequencies the situation is somewhat different. Taking first Fig. 3-10 in which the data for ka = 3.0 is shown, it is seen that there is no marked change in the surface field at the spacer itself, and ahead of the spacer the field is oscillating with a relatively small amplitude which is no longer consistent with an interference between forward- and backward-travelling waves. This is not surprising in view of the fact that the center of the spacer is only a distance 0.729λ along the surface from the tip. The mean level of the field is somewhat greater than for the pure cone-sphere; although the reason for this is not precisely known, it will be recalled that the level of the pure cone-sphere field was unexpectedly low in the near vicinity of the tip values of ka in this range.

At the lowest frequency, corresponding to ka = 1.100, the situation is different again (Fig. 3-9). There is now a slight dip in the amplitude at the position of the join, otherwise the sort of build-up away from the tip is that characteristic of a pure cone-sphere. This is true for the whole range of s/λ for which data was obtained. No comparison data for a pure cone-sphere is available for this ka, but if the curves for ka = 1.0 and 1.2 (Figs. 23 and 24 of Technical Report 7030-6-T) are superimposed, it is seen that there is an apparent increase in the mean level of the field as a consequence of the presence of the spacer. The increase is, however, small and is not believed to be significant. Even at these lower frequencies where the cone sides are only one or two wavelengths in extent, it is concluded that at the join and shadow boundary the surface fields are not affected by spacers to any sensible degree.

This being so, the back scattering from the nose-tip antenna model at nose-on incidence differs from that of the pure cone-sphere only by the addition of a contribution from the vicinity of the spacer itself, and any coupling between the spacer and base regions of the body is negligible in its effect. We can therefore compute the scattering from the spacer by ignoring the presence of the cone termination (i.e. by regarding the cone as infinite in extent) except insfar as, at the lowest frequencies, the residual creeping wave on the cone sides is still significant, in which case a proportionality factor could be introduced into the infinite cone analysis to account for the modified amplitude of the surface field at the position of the spacer. In practice, however, such a modification may be unnecessary when the spacer is near to the tip since its scattering is then negligible for all ka for which the residual creeping wave effect is measurable.

To estimate the back scattering produced by the spacer, there are several possible methods of attack open to us. We could , for example, seek to solve the boundary value problem for an infinite cone with a small dielectric insert, but this would be prohibitively difficult. It becomes possible, however, if we represent the spacer by a ring source and determine the strength of the source by comparing the induced field on the surface of the cone between the tip and the spacer with that attributable to the spacer in the measured data; but even this would be a major analysis of considerable difficulty. A third approach stems from the observation that as regards the portion of the cone ahead of the spacer, the spacer itself resembles the flat back of a right-circular cone. We might then use the wedge approximation with the effective strength of the singularity (or, equivalently, the assumed incident field strength) determined by a comparison of the amplitude of the observed oscillations in surface field strength with those of the surface field on a generator of a wedge immediately ahead of the edge. This is a relatively straightforward procedure, and should yield results of adequate accuracy except for cases in which the radius of the spacer is extremely small (when the scattering is negligible anyhow).

Both of the last two procedures make use of the observed amplitude of the surface field oscillations on the nose-tip antenna model immediately ahead of the spacer. This amplitude is directly related to the strength of the backward-travelling wave and, hence, to the back scattering. It would therefore seem that we could resort to an analysis in which we insert the measured form of the backward-travelling wave into the standard integral expression for the scattering amplitude in terms of the current component on a body of revolution at nose-on incidence. The reader is referred to Task 3.1.1 for a discussion of the backscatter from a nose-tip antenna.

3.1.3 Spheroidal Surfaces and

3.1.4 Creeping Wave Theory

The investigation of the contribution to the radar cross section attributable to creeping waves and the effect of surfaces of non-constant curvature as so related that it is most convenient to discuss them under one heading and that is done in this section.

There are two important theoretical problems that we need solve in order to predict the scattering from coated re-entry shapes. The first is the problem of determining the creeping waves on a coated surface of non-constant curvature. The second is that of determining the surface fields on a coated cone. We describe these problems and our approach to them below.

A. Creeping Waves on Coated Surfaces of Non-constant Curvature.

If we suppose that the electrical properties of the coating on a convex surface are such that an impedance boundary condition is a valid approximation, we have, after Fock (1946), an asymptotic formalism for surfaces of constant curvature. The Fock result is that the dominant surface field is given by an "impedance" Fock function of the form

$$\psi(\xi) = \frac{1}{\sqrt{\pi}} \int_{-\infty}^{\infty} \frac{e^{i\xi t}}{w'(t) - q\,w(t)}\, dt \tag{3.38}$$

where for a circular cylinder of radius a

$$\xi = \left(\frac{ka}{2}\right)^{1/3} \theta$$

$$w(t) = \sqrt{\pi}\left\{Bi(t) + i Ai(t)\right\}$$

$$q = i\left(\frac{ka}{2}\right)^{1/3} \eta$$

where η is the surface impedance,

$$\eta = \sqrt{\frac{\mu}{\epsilon}} \quad .$$

For the perfectly conducting case, $|\epsilon| = \infty$ and $q=0$, this expression (3.38) can be generalized to non-constant curvature by writing

$$\xi = \int_0^s \left(\frac{kR(s)}{2}\right)^{1/3} \frac{ds}{R(s)}$$

where s is the path length measured from the shadow boundary and R(s) is the radius of curvature at s. On the other hand, if $q \neq 0$, we have no obvious generalization (3.38) to non-constant curvature. For this reason, we have turned to the integral equation analysis of Hong (1966), which was performed for the $q=0$ case, and made a parallel analysis for the impedance boundary condition.

In order to generalize the Hong development to coated objects it is necessary to start with the appropriate integral equation for a solution of the Helmholtz equation which satisfies a mixed (impedance) boundary condition. We suppose a boundary B and wish to determine a function ψ such that

$$\begin{aligned} &(\nabla^2 + k^2)\psi = 0 \\ &\frac{\partial\psi}{\partial n} + ik\eta\psi = 0 \text{ on B} \end{aligned} \qquad (3.39)$$

and ψ satisfies the radiation condition. If the incident field is given by

$$\psi_o = e^{i\vec{k}\cdot\vec{r}}$$

then the boundary value, ψ on B, must satisfy the integral equation

$$\psi = \frac{2\gamma}{\gamma - \eta}\,\psi_o + \frac{2\gamma^2}{\gamma^2 - \eta^2}\, P\!\int_B \left(\frac{\partial G}{\partial n^1} + ik\eta G\right)\psi\, ds' - \frac{2\eta i}{\gamma^2 - \eta^2}\,\frac{1}{k}\,\frac{\partial}{\partial n}\, P\!\int_B \left(\frac{\partial G}{\partial n^1} + ik\eta G\right)\psi\, ds' \qquad (3.40)$$

where $\hat{n}$ and $\hat{n}'$ are unit normals to B,

$$\gamma = \hat{n}\cdot\hat{k}, \quad G = \frac{1}{4\pi}\,\frac{e^{ik|\vec{r}-\vec{r}'|}}{|\vec{r}-\vec{r}'|} \qquad ,$$

and the integrals over the surface B are defined as principal values.

In the limit $\eta \rightarrow 0$ (3.40) reduces to the equation considered by Hong; namely,

$$\psi = 2\psi_o + 2\, P\!\int_B \frac{\partial G}{\partial n^1} \;;\quad \frac{\partial \psi}{\partial n} = 0 \quad \text{on B} \qquad . \qquad (3.41)$$

Similarly, if we let $\eta \rightarrow \infty$, (3.40) and the boundary condition give

$$\frac{\partial \psi}{\partial n} = 2\gamma\,\frac{\partial \psi_o}{\partial n} - 2\, P\!\int_B G\,\frac{\partial \psi}{\partial n}\, ds' \;;\quad \psi = 0 \quad \text{on B} \qquad (3.42)$$

We have then both the Neumann and Dirichlet boundary conditions as special cases of the mixed boundary condition problem.

To carry out a parallel asymptotic analysis we need now to describe the boundary in geodesic coordinates and use the same asymptotic order analysis as for (3.41) using the much more complicated Eq. (3.40). At this point, we have shown that for a constant curvature along the geodesic we do obtain the classic result of Fock. We expect to obtain the higher order terms involving a non-constant curvature very shortly.

B. Surface Fields on Coated Cones.

Certain experimental measurements of the surface field on the conical portion of a coated cone-sphere have given unexpected results in that the field starting from the tip increases very like the conducting case to a value considerably above the predicted geometrical optics value and then decreases to the geometrical optics value as we move back from the tip. The experimental results are shown in Fig. 3-15.

Provided the cone is terminated with a sphere past the point at which the surface field reaches its geometric optics value there will be no additional effect on the creeping waves on the spherical portion. However, if the cone is terminated in the region in which the field is greater than the geometric optics field, we have a new enhancement problem. To solve this enhancement problem we need a description of the field on the coated cone.

We are approaching this problem in two ways, both based on a locally cylindrical approximation to the cone. The first approach is to suppose the field on the cone is a result of Goubau waves excited by the incident field. We are now computing the Goubau waves set up on a circular cylinder as a function of the cylinder radius. The computation has not yet reached the point that we can ascertain the validity of this model.

The second approach was suggested by an examination of the circular cylinder surface field satisfying an impedance boundary condition. This field is of the form

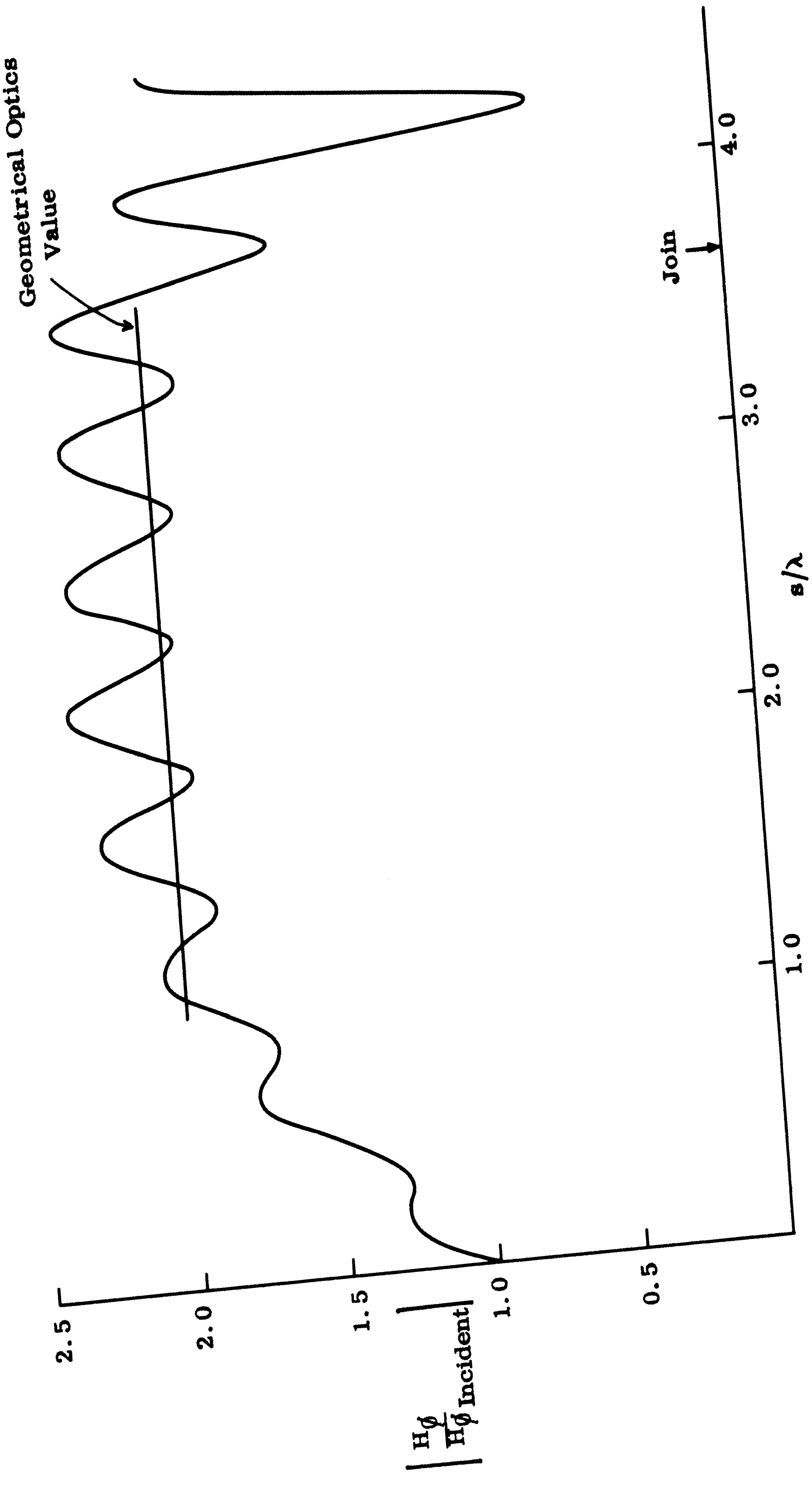

FIG. 3-15: SURFACE FIELDS ON A CONE-SPHERE COATED WITH RS-X.

$$H_{cyl} \sim \sum \frac{e^{ik\psi}}{H_n^{(1)'}(ka) + i\eta H_n^{(1)}(ka)}$$

We suggest that the behavior of the field on the cone can be predicted from the field induced on a circular cylinder where, for the radius a, we take the transverse radius of curvature of the cone at each point

$$a = r \sin\alpha$$

as in Fig. 3-16

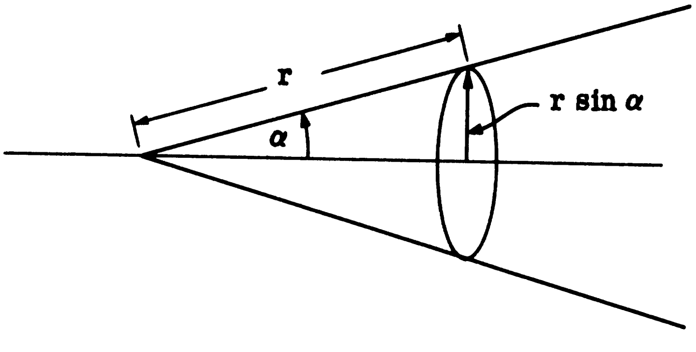

FIG. 3-16: THE CONE GEOMETRY.

In fact, if we consider the Rayleigh approximation to the cylinder, we deal with a term

$$\frac{1}{ka}\,\frac{1}{H_o^{(1)'}(ka)+i\eta H_o^{(1)}(ka)} \quad ; \quad ka \ll 1$$

and we see that the $H_o^{(1)'}(ka)$ term is clearly dominant, the effect of the impedance is not felt until the two terms $H_o^{(1)'}$ and $H_o^{(1)}$ are comparable in magnitude.

Given the field on an impedance cylinder as a function of ka, $H_{cyl}(ka, \eta)$ we suggest the field on the cone is given by

$$H_{cone}(r, \eta) = H_{cyl}(kr \sin\alpha,\ \eta) \quad .$$

In order to check this we need to compute $H_{cyl}(ka, z)$ for an η of interest and for $0 \leqslant ka < 1$. This computation is now under way.

3.1.5 Concave Re-entry Vehicle Terminations

An investigation is being made of the effect on radar cross section of re-entry bodies due to concavities at the rear of the vehicle. A series of models are being studied. They have rear indentations of varying depth but are modelled generally on the Mark 12 re-entry vehicle. The models are illustrated in Fig. 2-5. This section reports on the study of the surface fields measured on one of the three models.

The amplitudes of the surface field component H_ϕ have been measured for plane wave excitation at nose-on incidence on a cone-sphere whose half angle is 7 1/2° and whose rear spherical cap has a concave indentation. The base radius a of the original spherical cap was 2.210". However, one effect of the concave spherical indentation and the requirement of a continuous tangent is to reduce the rear cap to a portion of a torus whose inner radius is 0.553" bounded on one side by its join with the cone and on the other side by a smooth join with a concave spherical surface of radius 4.558" with center on the cone axis. The resulting model is called Model ID-1.

Measurements were made at four frequencies (0.935, 2.55, 4.2499 and 6.799 Gc) corresponding to ka = 1.100, 3.000, 5.000 and 7.999, respectively. The distance between the join and the antipode along the the rear spherical cap of a cone-sphere of 2.210" base radius is 3.761" while the measured distance between the join and the rear-most point for Model ID-1 is 2.625". Thus, the path length on Model ID-1 is 0.090, 0.245, 0.409 and 0.654 λ shorter from the join to rear than on the spherical cap of the cone-sphere for the above four frequencies.

The data is illustrated in Figs. 3-17 through 3-20 and, except for the lowest frequency (corresponding to a measurement at ka = 1.100), a comparison curve from Technical Report 7030-6-T for the measured value of H_ϕ on a pure metallic cone-sphere of the same ka is available, and is shown in Figs. 3-18 through 3-20 by the dotted curve.

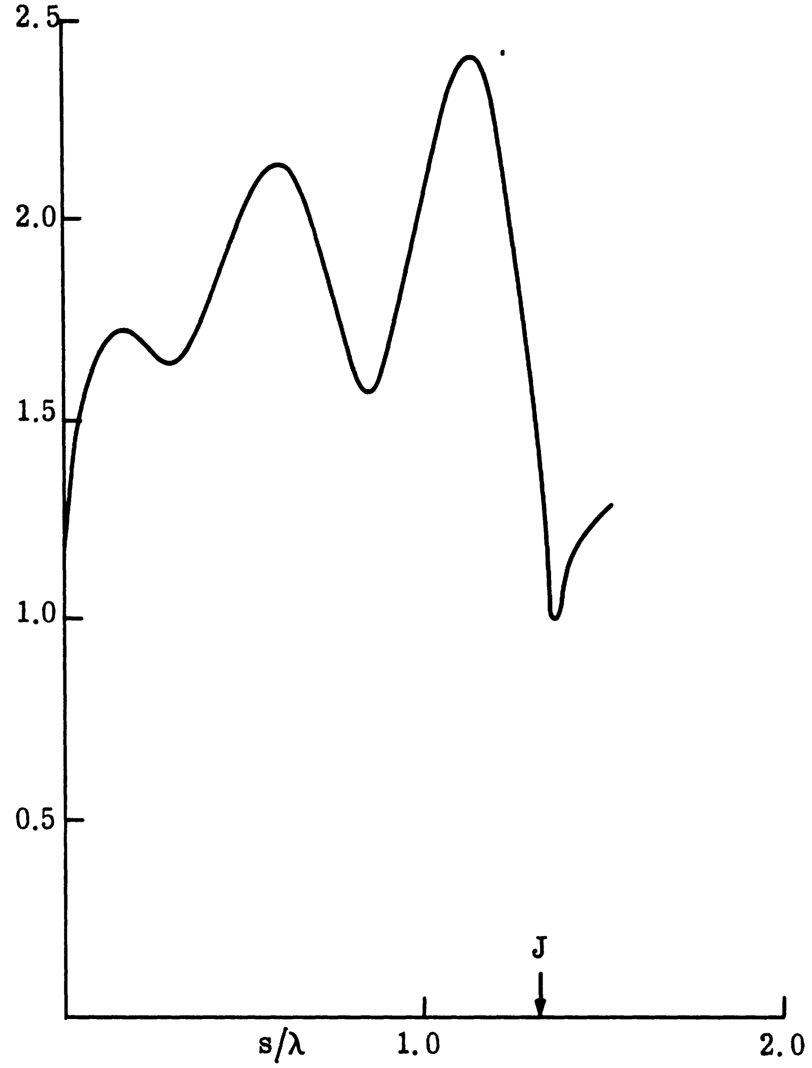

FIG. 3-17: MODEL ID-1, INDENTED BACK (ka=1.1, 0.935 Gc.)

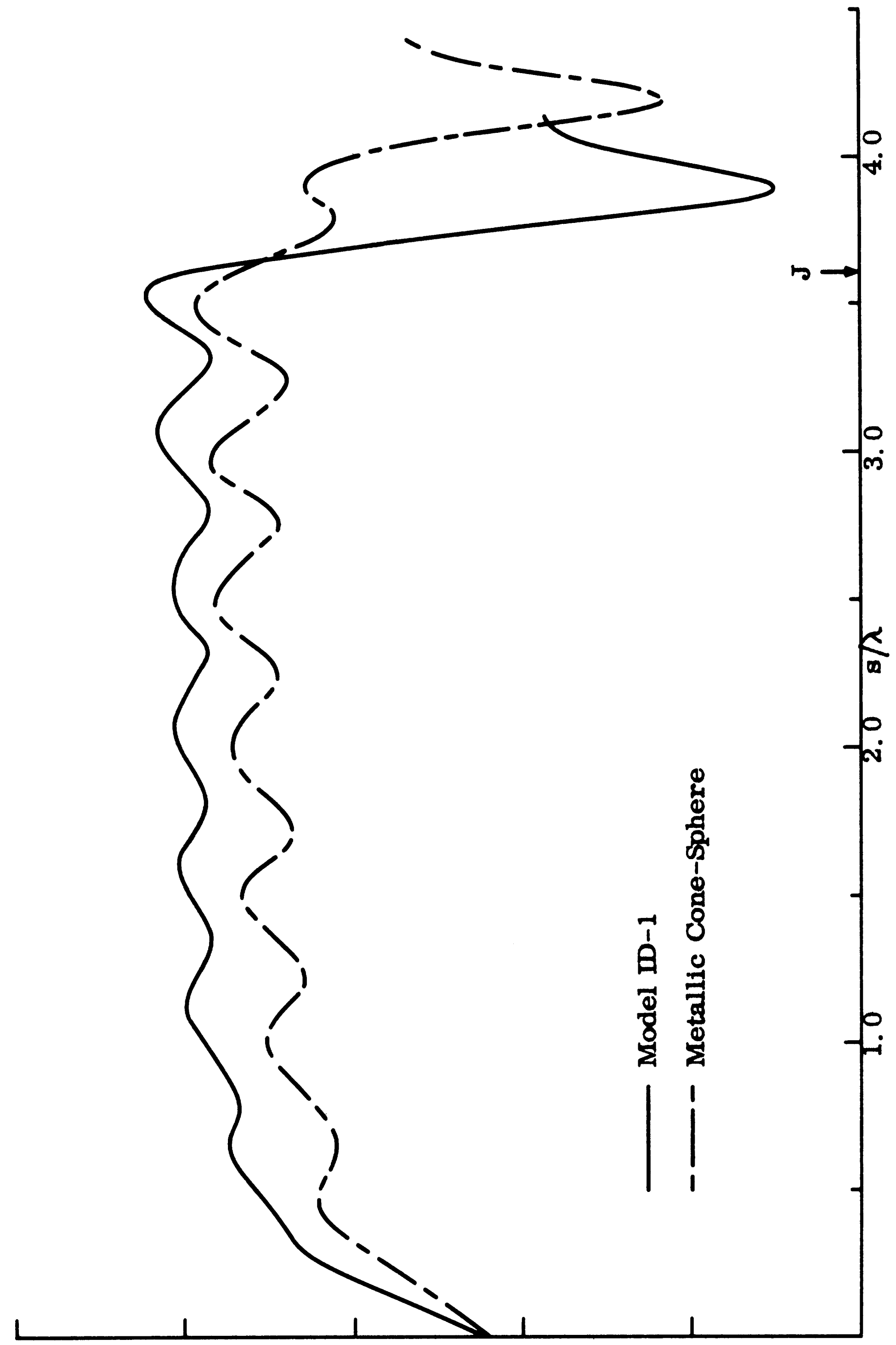

FIG. 3-18: MODEL ID-1, INDENTED BACK (ka=3.0, 2.55 Gc.)

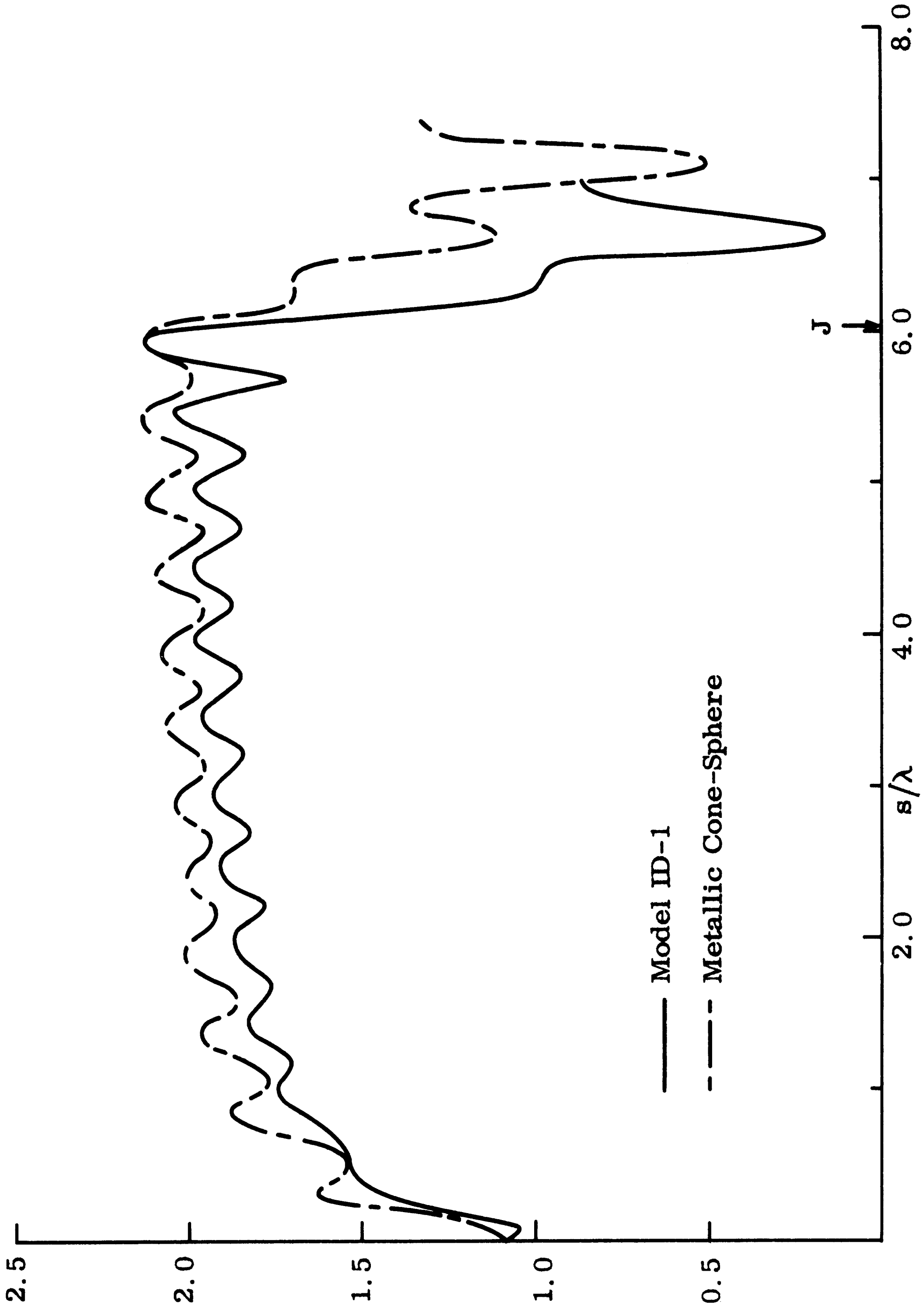

FIG. 3-19: MODEL ID-1, INDENTED BACK (ka=5.0, 4.2499 Gc.)

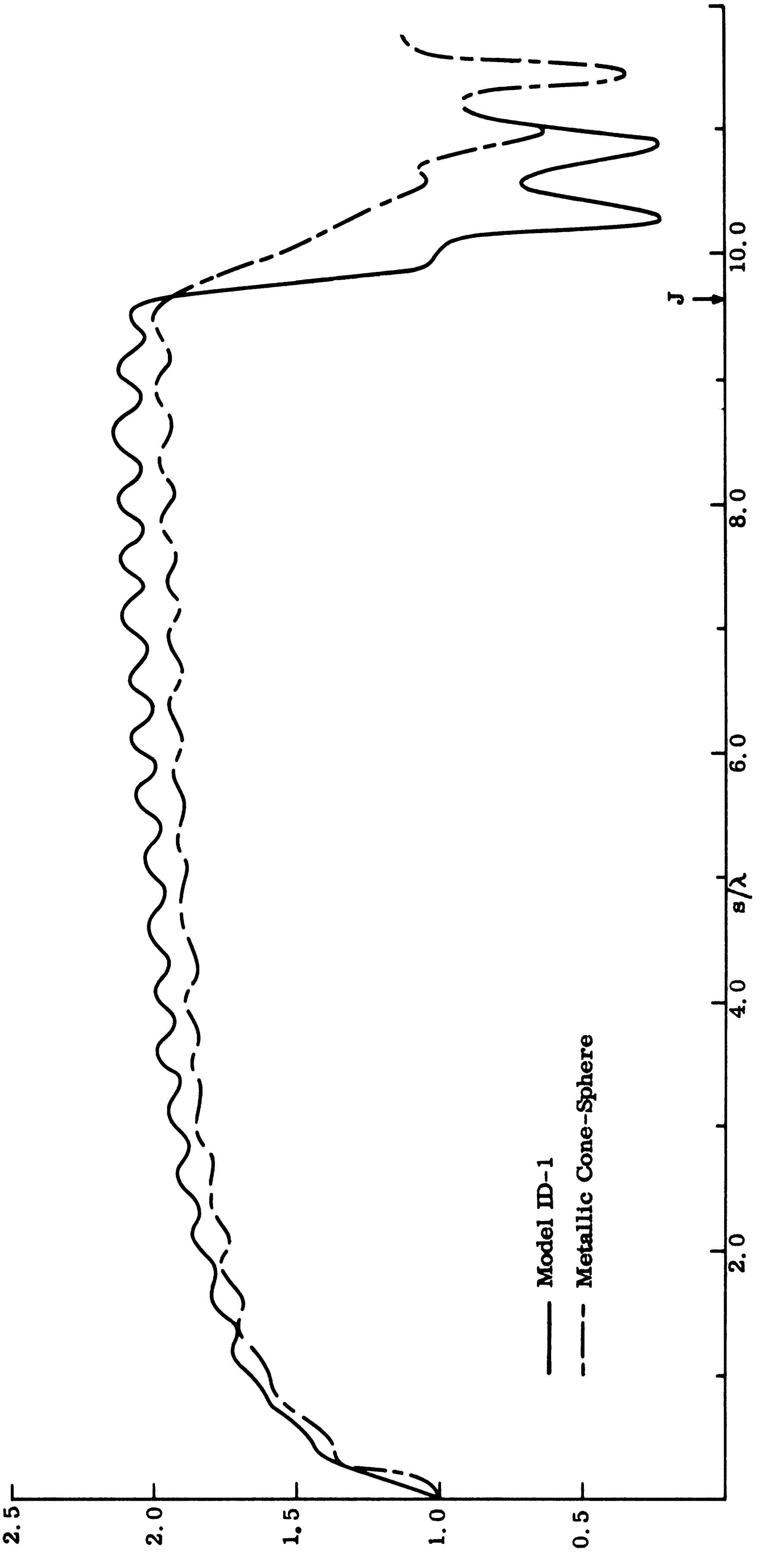

FIG. 3-20: MODEL ID-1, INDENTED BACK (ka=8.0, 6.799 Gc.)

For the lowest frequency (0.935 Gc) the solid curve of Fig 3-17 shows the measured value of H_{ϕ} on Model ID-1; near the cone-cap join the mean level of surface field is 0.98. For the pure cone-sphere it is 1.88 for ka=1.0 and 1.90 for ka=1.2 suggesting that the mean surface field for Model ID-1 is about 5 per cent greater than its value on a pure cone-sphere. This ratio is (approx.) maintained over the entire lateral portion of the model and holds even near the tip. The theoretical amplitude of the creeping wave at the join of a pure cone-sphere appropriate to ka=1.1 is about 0.4. By associating half the difference between successive minima and maxima as the strength of this travelling wave component one finds that these magnitudes for Model ID-1 are 0.3 and 0.4 for the two oscillations nearest the join and this would suggest little or no increase in the strength of the creeping wave for the model. However, these amplitudes increase as the join is approached and an interpolation to the value at the join itself yields 0.5 for the approximate creeping wave strength.

Figure 3-18 illustrates the surface field for Model ID-1 and for a cone-sphere at a frequency of 2.55 Gc corresponding to ka=3.0. The general patterns are similar. The tip value of H_{ϕ} is very nearly 1.10 for both models but within 2λ of the tip the surface field for Model ID-1 rises to a mean value of (approx.) 2, and remains there until the rear cap is approached. On the other hand, for the cone-sphere the surface field also rises quickly near the tip and even thereafter there is a slow, perceptible rise in the mean level until the join is reached,where it achieves a value of about 1.84. Over the cap portion the surface field amplitude for Model ID-1 drops sharply between the join and shadow boundary and then rises to about 0.64 of its value at the nearmost position on a pure cone-sphere. The surface field oscillations along the lateral portion of the model have an amplitude near the join which is only about 0.69 of its strength for the pure cone-sphere.

Since the measured mean surface field amplitude is anomalously low for the cone-sphere with ka=3.0 near the join, if it is assumed that this is merely due to a calibration difficulty and for Model ID-1 and the cone-sphere they should, in fact, be substantially the same, the effect of the indented back on the backscattering cross sections should be due to the reduced creeping wave amplitudes on Model ID-1 compared with their strength on a pure cone-sphere. The reduction in the nose-on backscattering cross section is (see Task 3.1.1 "Estimating Scattering from Surface Field Data") proportional to the square of the ratio of the creeping wave amplitudes if the mean surface amplitudes at the join are the same.

$$\frac{\sigma_{\text{ID-1}}}{\sigma_{\text{c.s.}}} = \left| \frac{|J|_{\text{c.w. ID-1}}}{|J|_{\text{c.w. c.s.}}} \right|^2 = |1.69|^2 = 0.48 \quad .$$

This compares with (see Task 3.1.1, 'Preliminary Analysis of Radar Backscattering from ID-1") measured ratios of 0.59 and 0.25 and the prediction is not only qualitatively correct, but also of the correct order of magnitude.

Figure 3-19 compares the surface fields for Model ID-1 and a pure cone-sphere at 4.2499 Gc corresponding to ka=5.0. Inspection of the graph shows that over the lateral portion, the surface fields behave very similarly. At the tip H_ϕ is about 10 per cent greater than unity for both models and rises rapidly in the first half wavelength from the tip. Thereafter the oscillations have fairly regular periods and amplitudes for both models, although the velocity of propagation of the backward travelling wave on Model ID-1 seems altered since near the tip the oscillations for the two models appear to be 180° out of phase, while near the join they appear to be in phase. For Model ID-1 the mean level of H_ϕ near the join is about 0.94 of its value for the cone-sphere (1.93 compared with 2.05) while the ratio of the amplitudes of the backward travelling wave is very nearly unity. From this it would appear that the nose-on backscattering cross section at this frequency for Model ID-1 would be only slightly smaller than for a pure cone-sphere.

In Fig. 3-20 the surface fields for model ID-1 and a pure cone-sphere are compared at a frequency of 6.799 Gc corresponding to ka=8.0. Both curves are again similar in many respects: both build up rapidly within the first wavelength and subsequently exhibit fairly regular oscillations about a mean level which, near the join, for Model ID-1 is (about) 2.08, while for the cone-sphere is approximately 1.96.

Over the indented cap the surface field drops more sharply near the shadow boundary. The oscillations along the lateral portion are reasonably regular, but are 180° out of phase for this entire distance. For Model ID-1, the amplitude of the backward travelling wave is about 1.5 its value on a pure cone-sphere. Both factors indicate that the nose-on backscattering cross section should be greater for Model ID-1 than for a cone-sphere by a factor of 2 to 3.

3.1.6 Effect of Coating Materials

The effect of coating materials was studied by examining the surface fields measured on a simple coated cylinder and then on a coated cone-sphere. In both cases it was possible to compare the fields induced on the coated model with the field induced on a bare metallic model of the same shape and at the same frequency and draw conclusions as to the effect produced by the coating.

A. Surface Field Measurements on a Coated Cylinder

A metal cylinder of length 24 in. and radius a=1.500 in. was coated with an S-band absorber of nominal thickness 0.14 in. No information about the properties (e.g. normal incidence reflection coefficient, or material constants) at the relevant frequencies is yet available.

With the cylinder mounted vertically on the support pedestal, the amplitudes of the associated magnetic and electric surface field components were measured at the frequencies 3.381 and 6.262 Gc at points approximately 0.25 in. apart around a circumferential trajectory mid-way between the ends. Since the incident magnetic vector was along the axis of the cylinder, the components measured were, in fact, H_z and E_θ, where (r, θ, z) are cylindrical polar coordinates. The measured length of the circumference was 10.273 in., corresponding to an outer radius b=1.635 in. The average thickness of the coating was therefore 0.135 in., and whereas the values of ka for which the measurements were made were 2.700 and 5.000, the values of kb were 2.943 and 5.451.

The field strength data in db versus circumferential distance was converted to linear readings of the field component relative to its free space value versus angular distance θ, where θ was measured from the center of the illuminated face of the cylinder. Smooth curves were then drawn through the data points associated with the left- and right-hand sides of the cylinder, and these are shown in Figs. 3-21 and 3-22. Also shown are the theoretical curves for H_z for a completely metal cylinder of the same outer radius, the curves being computed using the exact eigenfunction

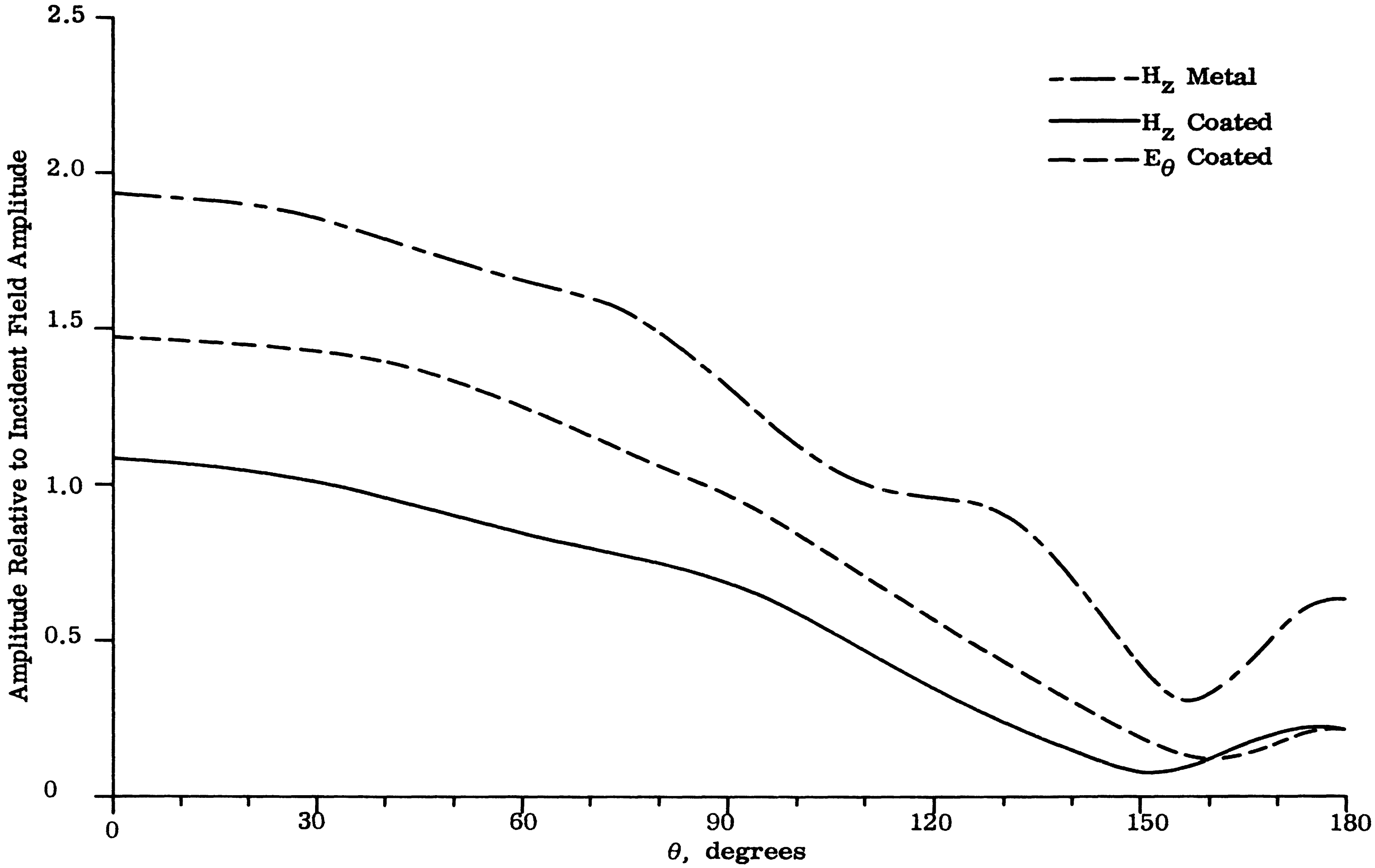

FIG. 3-22: SURFACE FIELDS ON COATED CYLINDER (kb=2. 943).

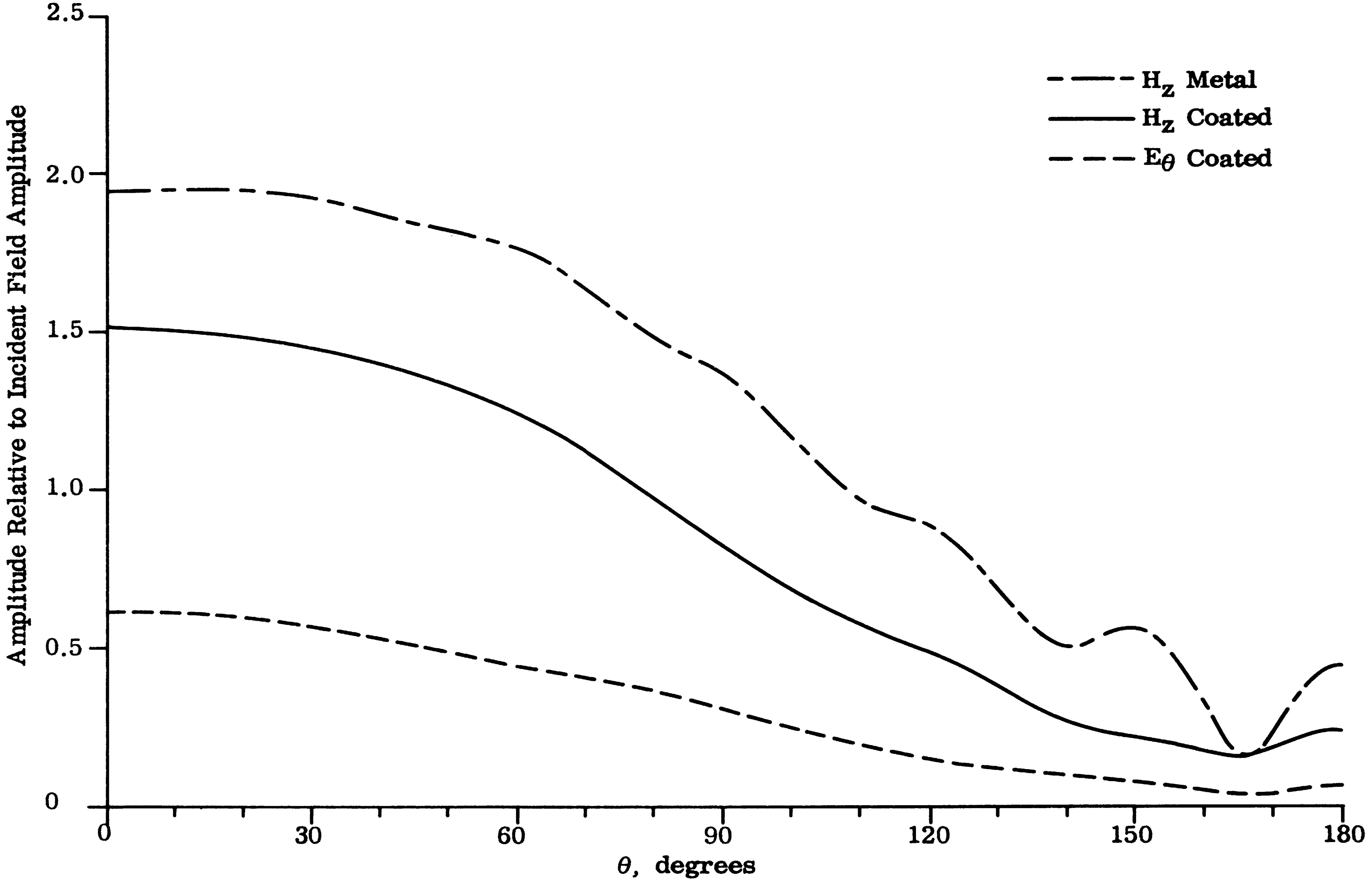

FIG. 3-22: SURFACE FIELDS ON COATED CYLINDER (kb = 5.451).

expansion. It will be observed that the effect of having the outer layer of the cylinder not perfectly conducting is to reduce $|H_z|$ by an amount which is somewhat greater at the lower frequency. On the other hand, $|E_\theta|$ (which is zero on a metal cylinder) is greater than H_z at the lower frequency, but a good deal less at the higher one.

If an impedance boundary condition holds at the surface, then

$$E_\theta = -\eta Z H_z$$

where Z is the intrinsic impedance of free space, and η is the effective surface impedance of the coating relative to Z. If the thickness is large compared with the skin depth in the coating, η is a function of the material parameters only; if the thickness is not large compared with the skin depth, the actual thickness also plays a role in η and if, in either case, the radius of curvature of the surface is not large compared with the wavelength, a dependence on this radius theoretically occurs.

By virtue of the normalization of the measured data, the ratio $\left|E_\theta/H_z\right|$ should be equal to $|\eta|$ if an impedance boundary condition holds, where η must be independent of θ, but may (and almost certainly will) vary with frequency. The ratios of the field components at the two frequencies are shown in Fig. 3-23 . At the lower frequency, the ratio is reasonably constant at about 3 db (= 1.4) out to $\theta = 105^\circ$ (approx.), and then rises rapidly to a maximum of about 8 db near $\theta = 150^\circ$, before falling to almost unity. It would therefore appear that at this frequency an impedance boundary condition is reasonably fulfilled over the illuminated region, but not in the deep shadow. At the higher frequency the region of fulfillment embraces almost the whole cylinder, and out to $\theta = 160^\circ$ the ratio differs from -8 db (= 0.40) by no more than $\pm$ 1 db. Inexplicably, however, there is a marked change within the next 20°, with the ratio dropping almost to -16 db at $\theta = 166^\circ$, but because of the minima in the field components occurring near this angle, the effect could be due to experimental error. In short, it is believed that Fig. 3-23 provides adequate confirmation

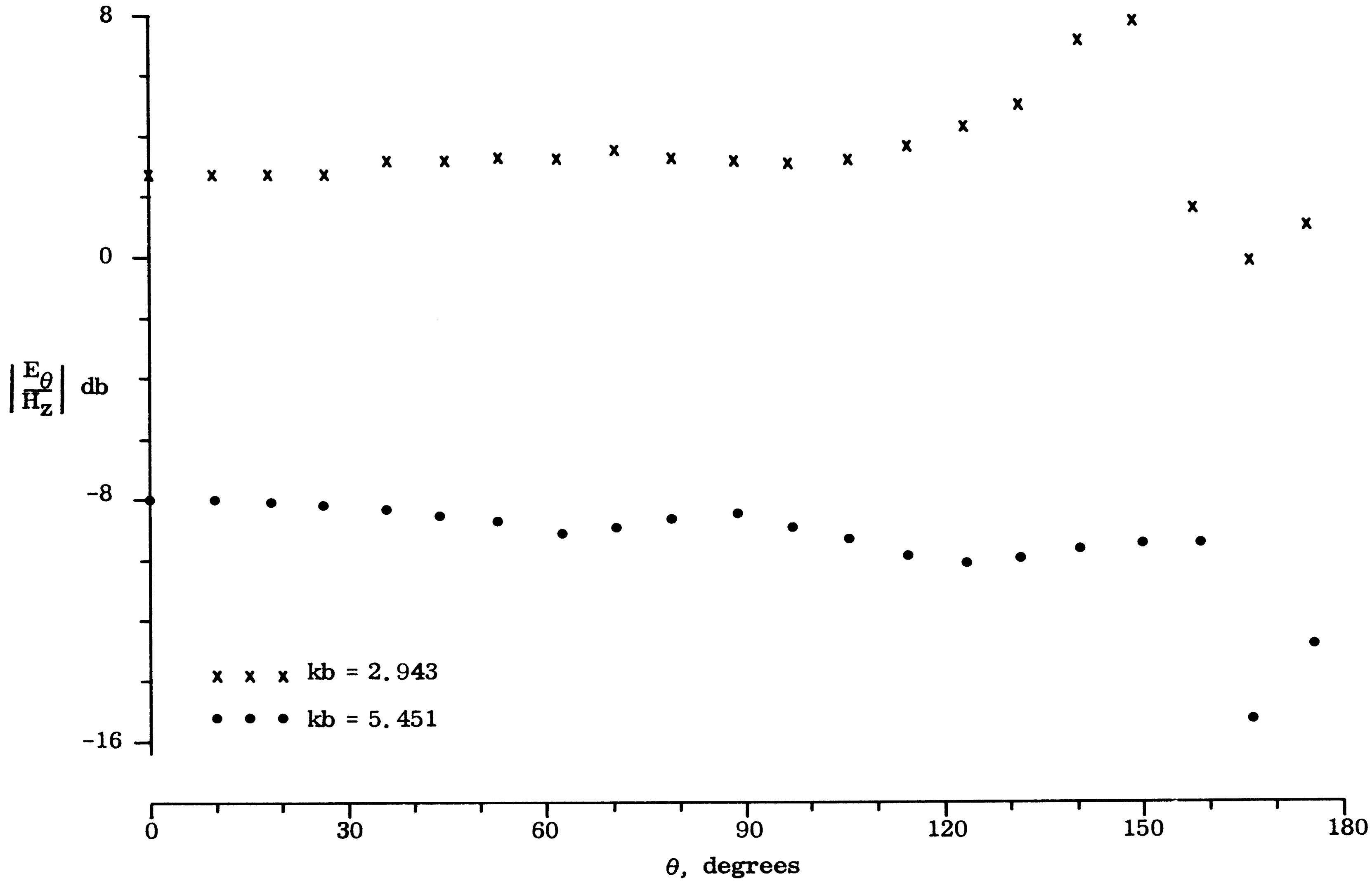

FIG. 3-23: RATIO OF FIELD STRENGTHS AT TWO FREQUENCIES.

of the general validity of an impedance boundary condition at the higher frequency at least, and the drastic modification to the effective value of $|\eta|$ as the frequency changes from 3.381 Gc to 6.262 Gc is probably due more to the change in the electrical thickness of the coating than to a variation in the material constants of the coating per se.

Insofar as an impedance boundary condition can be assumed to hold uniformly over the whole surface, the reduction in the backscattering cross section produced by the coating can be determined by the direct computation of the appropriate eigenfunction series, using a value for the effective surface impedance deduced from the preceding graphs. This is a straightforward, though tedious, computational task. Some more direct information about the backscattering is, however, obtainable from the surface field data. At the higher frequency, $|E_\theta|$ is small compared with $|H_z|$ over the entire surface and, consequently, the latter field component is the major source of the scattering. At the front of the cylinder the coating has reduced $|H_z|$ by 2.2 db relative to what it was on a metal cylinder of the same outer radius. The optics contribution P^o to the far field amplitude P for a cylinder of infinite length and, hence, for a long cylinder of finite length, will therefore be reduced by the same amount. Moreover, to the leading term in the high frequency expansion, the creeping wave contribution to P is

$$P^c = \frac{-i}{4} kb \left\{ H_z(\pi) \right\}^2 ,$$

where $H_z(\pi)$ is the surface field at $\theta = \pi$. From Fig. 3-22 we observe that the coating has reduced H_z by 7.2 db at this point. The far field component P^c has therefore been reduced by 14.4 db relative to what it would have been for a metal cylinder of the same outer radius. The coating has therefore suppressed the creeping waves to a much greater extent than it has reduced the specular return, and this fact is evident in the almost complete absence of any major oscillations in the curve for H_z on the coated body.

When used in conjunction with the known magnitudes of P^o and P^c as functions of the electrical size of a metal cylinder, the above factors enable the cross sections of the coated cylinder to be obtained immediately. Unfortunately, at the lower frequency such a trivial analysis is not possible since E_θ is not the dominant surface field component on the coated cylinder, although a comparable analysis might be feasible by using as the basis of comparison the surface field component E_θ on a cylinder of 'perfect' ferrite (for which the boundary condition is $\hat{n} \wedge \underline{H} = 0$ at the surface).

B. Surface Field Measurements on an RS-X Coated Cone-Sphere

The amplitudes of the surface field components H_ϕ ($\equiv J_s$) and E_ϕ have been measured for a plane wave at nose-on incidence on a cone-sphere uniformly coated with a layer of RS-X absorber. The half angle and base radius of the metal substrate were $7\frac{1}{2}^\circ$ and 2.210 in. respectively. The nominal thickness of the coating material was 1/16 in., but from the measured length of the probe trajectory from join to join on the surface, a value for the thickness equal to 0.031 in. can be deduced. It is probable that the discrepancy is due more to a slight error in the location of the join between the conical and curved portions of the coated body than to a shrinkage in the thickness of the coating.

The measurements were carried out at the three frequencies, 2.55, 4.25 and 6.80 Gc, for which the corresponding values of ka are 3.00, 5.00 and 8.00. To two significant figures, kb and ka are identical, where b is the outer radius of the base. In the following three figures, the measured amplitude data for H_ϕ and E_ϕ is presented, and for each value of ka the appropriate curve for H_ϕ for a pure metallic cone-sphere is included (see Report 7030-6-T).

Taking first the data for the lowest frequency for which ka = 3.00 (Fig. 3-24) we note that the mean of the H_ϕ curve for the coated body is comparable to the mean for the uncoated one when $s/\lambda \lesssim 0.5$, with both curves starting at a value near unity when $s = 0$. For $s/\lambda > 0.5$, the mean curve for the coated body lies somewhat above the uncoated mean, with both means levelling out as functions of s for $s/\lambda \gtrsim 2.0$. Between here and the join the mean curve for the coated body is about 1.2 db above that for the uncoated one, and since this ratio holds also at the join, it is concluded that the join contribution to the far field amplitude is increased by the same amount as a result of the coating. The oscillations of both H_ϕ curves are very regular in period and reasonably constant in amplitude as functions of s. There is, however, a slight slippage in the locations of the maxima and minima of one curve relative to the other. Noting the coincidence of the minima at $s/\lambda = 3.8$, the slippage indicates a difference in the relative phase of the forward- and backward-travelling waves on the two bodies. The effect is, however, small. In the immediate vicinity of the join, the mean amplitude of oscillation of the curve for H_ϕ on the uncoated body is approximately 1.4 times the mean amplitude on the uncoated body. The ratio of the surface field amplitudes at the rearmost points on the two bodies is similarly 1.4.

The values for E_ϕ on the coated body (E_ϕ is, of course, zero on the uncoated one) start near unity for $s \simeq 0$ and fall rapidly with increasing s. For $s/\lambda \geqslant 0.75$, the mean curve is almost constant at around 0.3 out to well beyond the join. The oscillations are small in magnitude, and the maxima and minima tend to be out-of-phase with those of H_ϕ. Although there is a slight increase in E_ϕ deep in the shadow, the component E_ϕ is negligible compared with H_ϕ except at the tip itself.

As the frequency increases there is a marked change in the behavior of the dominant surface field component H_ϕ on the coated body. This is apparent on comparing Fig. 3-25, for which ka=5.0, with Fig. 3-24. Though the mean of the curve for H_ϕ on the coated body is similar to that for the uncoated one when $s/\lambda \lesssim 1.0$, it levels out at around 1.75 and, for $s/\lambda \gtrsim 2.0$, falls rapidly. From here out to beyond the join, the average decrease is about 2 db per half wavelength. In the vicinity of the join, the mean is approximately 8.7 db below that for the uncoated body, which reduction should also apply to the join contribution to the far field amplitude. The amplitude of oscillation of the component H_ϕ on the coated body is less than for the uncoated one and, moreover,

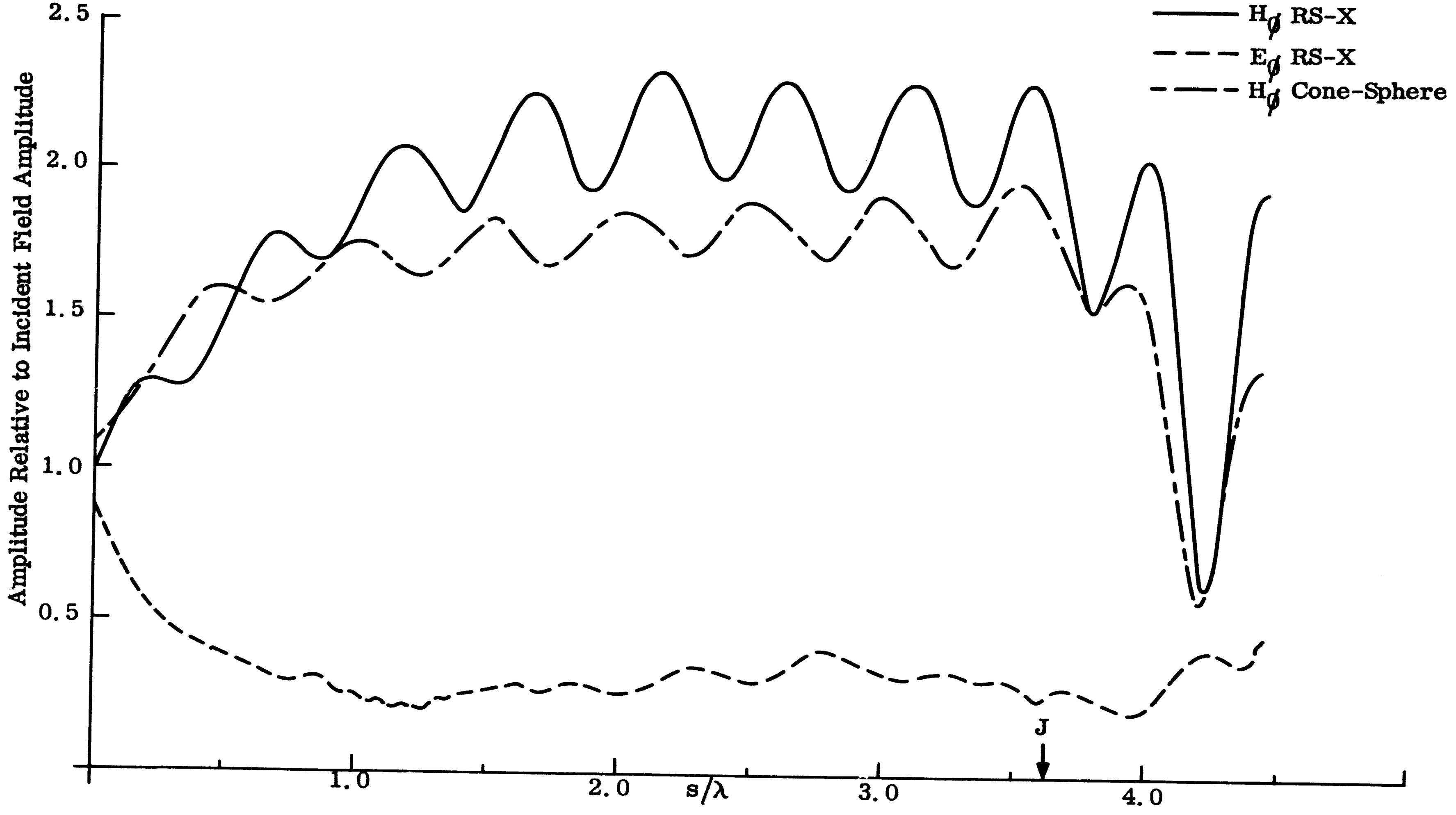

FIG. 3-24: SURFACE FIELDS ON COATED CONE-SPHERE (ka = 3.0).

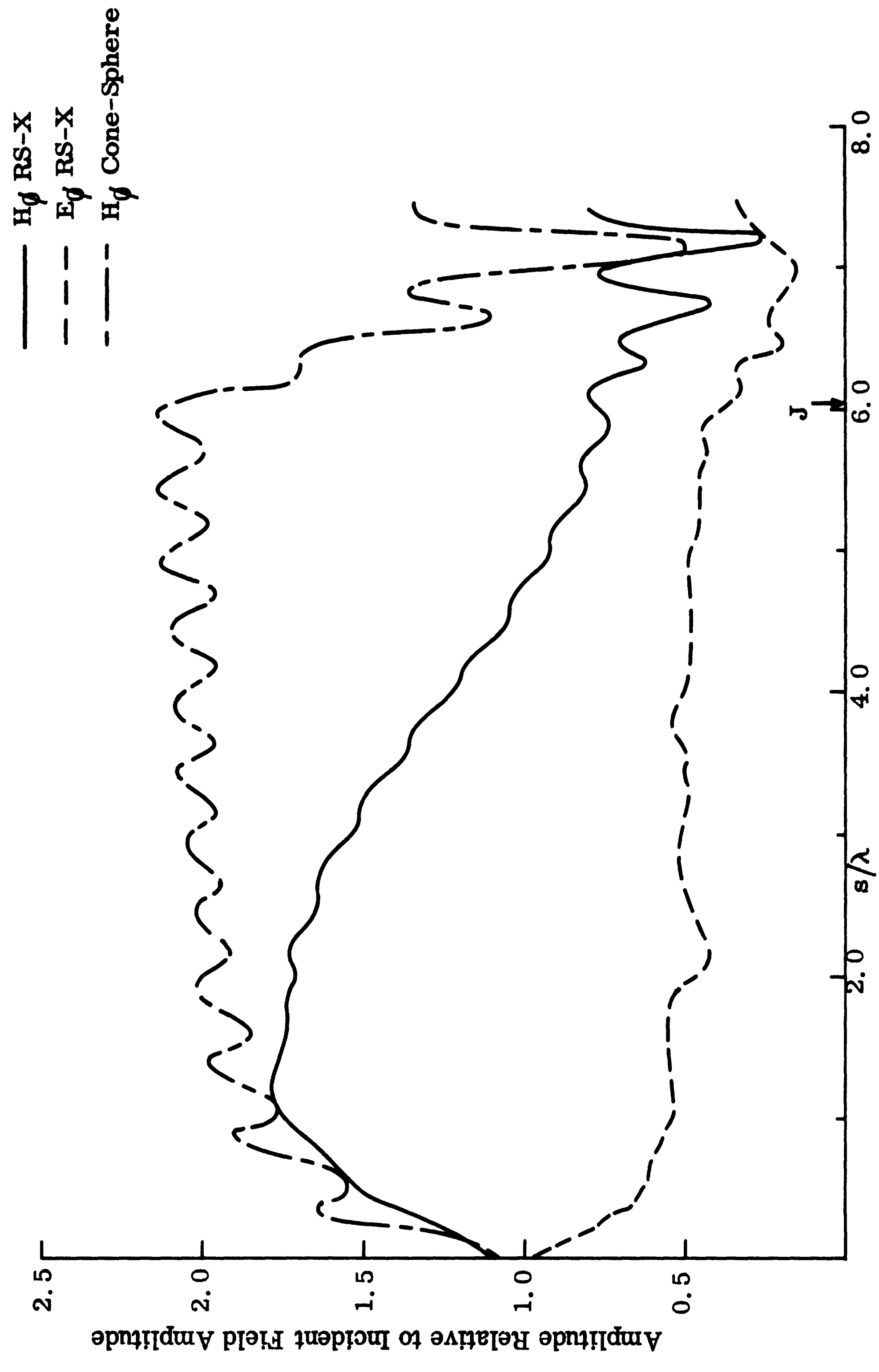

FIG. 3-25: SURFACE FIELDS ON COATED CONE-SPHERE (ka=5.0).

decreases with increasing distance forward of the join. This is compatible with the absorption provided by the coating. Near the join, the amplitude of oscillation is approximately 0.5 times that for the uncoated one. The ratio of the surface field amplitudes at the rearmost points on the two bodies is 0.60.

The values of E_ϕ are somewhat greater than those in Fig. 3-24. After the initial rapid fall as s increases from zero, the component levels out at a value of about 0.50, and maintains this value out to the join. There is a general decrease in magnitude beyond the join, and we again note a tendency for the oscillations of H_ϕ and E_ϕ to be out of phase. In comparison with H_ϕ, the component is still small over almost all the surface, but not quite so negligible as at the lower frequency. Indeed, at the join and beyond it is within about a factor 2 of H_ϕ.

At the highest frequency, 6.80 Gc, for which ka = 8.00, the field component H_ϕ on the coated body is even more suppressed (Fig. 3-26). Though the component starts with a value in excess of that on the uncoated body at the tip, it rises more slowly with increasing s, and its magnitude is comparable to that on the uncoated body for $s/\lambda = 0.4$. Thereafter, it decreases rapidly, falling at an average rate of 1.8 db per half wavelength relative to the metallic-body field out to a distance of 3 wavelengths from the tip. Beyond this value of s, the rate of fall-off is somewhat less, and for $s/\lambda \gtrsim 5$, the field component H_ϕ is almost constant even to the shadow boundary. In the region about the join, the mean value of H_ϕ on the coated body is 15 db below the mean for the uncoated one, and this should represent the amount by which the join contribution to the far field amplitude is reduced by the coating. Forward of the join, the field component H_ϕ on the uncoated body shows quite regular oscillations which are attributable to the residual effect of the creeping waves, but in contrast the component H_ϕ on the coated body is almost devoid of any oscillation. No estimate of the reduction in the creeping wave contribution to the far field amplitude is therefore possible on this basis, but we note that at the rearmost point on the two bodies the ratio of the surface field amplitudes on the two bodies is 0.20.

The values for the field component E_ϕ have decreased somewhat compared with those in Fig. 3-25, and are more akin to the values at the lowest frequency, 2.55 Gc.

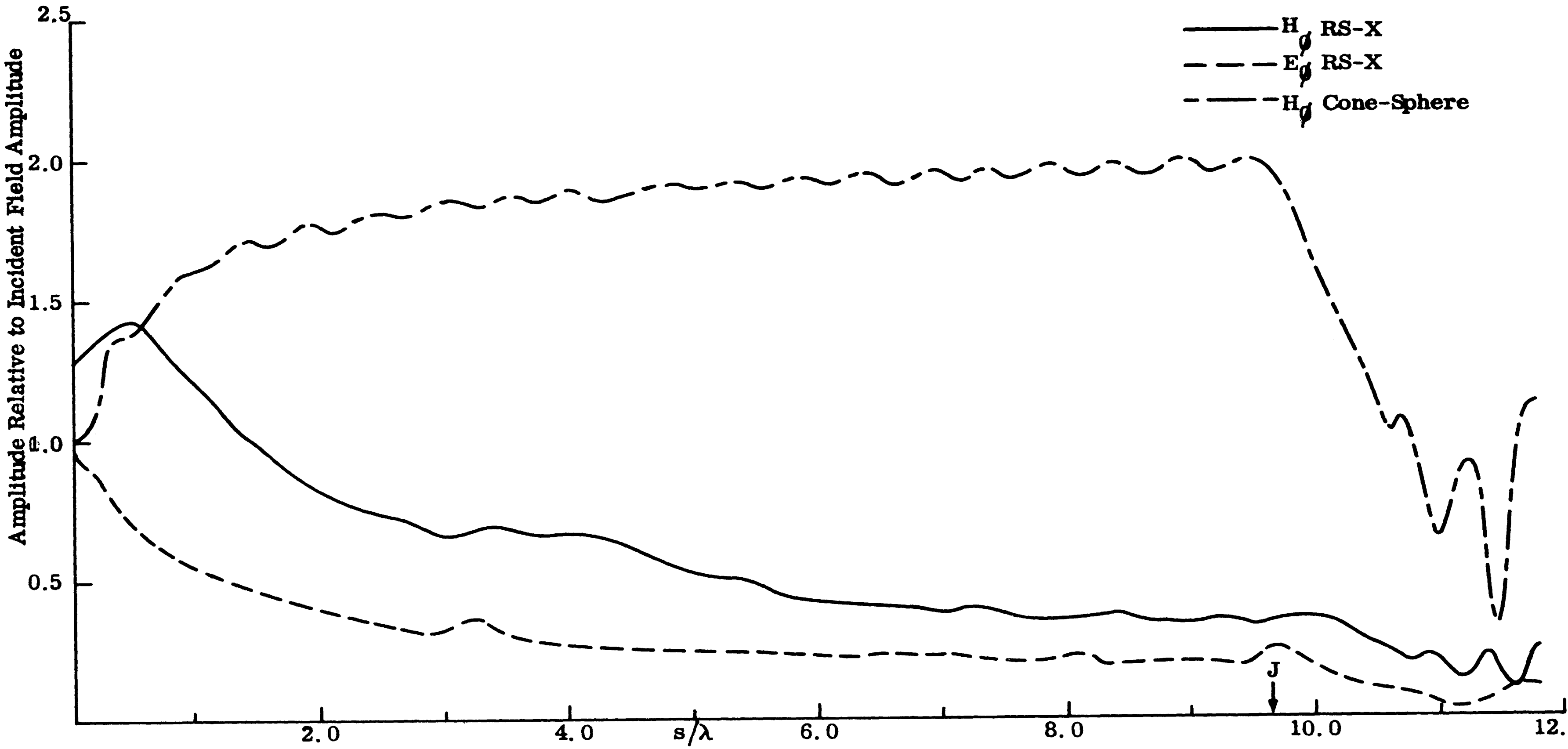

FIG. 3-26: SURFACE FIELDS ON COATED CONE-SPHERE (ka=8.0).

The component decreases rapidly from near unity as s increases from zero, and is almost constant at around 0.2 for $4 < s/\lambda < 10$. Here, as well as within the shadow, there is no evidence of any oscillation, and except at points close to the rearmost point of the body, the component is always smaller than H_ϕ by a factor 2 or more.

The marked changes in the surface field components H_ϕ and E_ϕ on the coated and uncoated bodies in the vicinity of the join provides a measure of the reduction in the join contribution to the far field amplitude in the back scattering direction providing the additional field component E_ϕ is not itself so large as to generate a significant contribution to the scattering. This appears true in the cases considered here. Unfortunately, estimates of the reduction in the magnitude of the creeping wave contribution to the scattering are not so easily arrived at, but some feel for the reduction can be obtained by examining the reduction in the surface field amplitude $T_2(\pi)$ at the rearmost point, and from the decrease in the observed amplitude of the oscillation of H_ϕ in the vicinity of the join. If the ratio of launch-to-birth weights of the creeping waves were independent of the presence of the coating, the reduction in the magnitude of the creeping wave contribution to the far field amplitude would be equal to the square of the reduction in $T_2(\pi)$, leading to the following estimates for the creeping wave effect.

Frequency (Gc)	Reduction (in db) in $S^{cw}(0)$
2.55	-6
4.25	9
6.80	28

If, on the other hand, the launch weight were independent of the coating, the reduction in $S^{cw}(0)$ would be equal to the decrease in the amplitude of the surface field oscillations at the join, giving:

Frequency (Gc)	Reduction (in db) in $S^{cw}(0)$
2.55	-3
4.25	6
6.80	large

Which method (if either) of estimation is substantially correct is still to be determined, but on either basis the decrease in the creeping wave contribution to the far field produced by the coating is quite large. For comparison purposes, the reductions in the join contribution $S^{j}(0)$ are as follows:

Frequency (Gc)	Reduction (in db) in $S^{j}(0)$
2.55	-1
4.25	9
6.80	15

Note that without a knowledge of the change in phasing of the contributions $S^{cw}(0)$ and $S^{j}(0)$ resulting from the presence of the coating, the above estimates give only the maximum and minimum nose-on cross sections over the frequency range considered.

3.1.7 Radar Cross Section of the Cone-Sphere in a Re-entry Environment.

The objective of this Task is to compute the back scattered fields produced by a plane electromagnetic wave incident upon a plasma coated re-entry vehicle. The approach being followed was discussed in some detail in the Second Quarterly Report. In this quarter, we discuss the computation of the reflection coefficient for various stations along the surface of the vehicle and conclusions to be drawn from the computations, which is an intermediate step in the end process.

Calculations of the local reflection coefficient $R_{\perp}$ (electric field polarized perpendicular to the plane of incidence) have been carried out for Profiles 4, 5, 6, and 7. Profiles 4, 5, 6, and 7 are for altitudes of 100, 80, 60 and 30 thousand feet, respectively, and for turbulent flow. The coefficient $R_{\perp}$ was computed for the five frequencies 10^8, 5×10^8, 10^9, 5×10^9 and 10^{10} Hz, and two angles of incidence 0 and 79° measured from the normal to surface. The former angle of incidence is applicable to the nose-on case, whereas the latter is applicable to the broadside case. In addition, three different boundary conditions were specified on the inner surface of the sheath, corresponding to the case of the sheath enclosing a perfectly conducting surface, an absorbing surface (represented by an impedance boundary condition), and free space. The calculations were carried out for a set of stations along the conical surface measured from the tip. The results pertaining to the magnitude of R are given in Figs. 3-27 to 3-34.

From Figs. 3-27 to 3-29, it is seen that the magnitude of the reflection coefficient R is approximately independent of the electrical properties of the inner surface (be it a perfect conductor, absorber, etc.) for stations along the surface a distance greater than 13" from the tip. This means that for nose-on incidence to the body, the sheath completely shields the body except for the immediate region of the tip. From Figs. 3-30(a) to 3-30(e), corresponding to Profile 7 (30 K ft.),

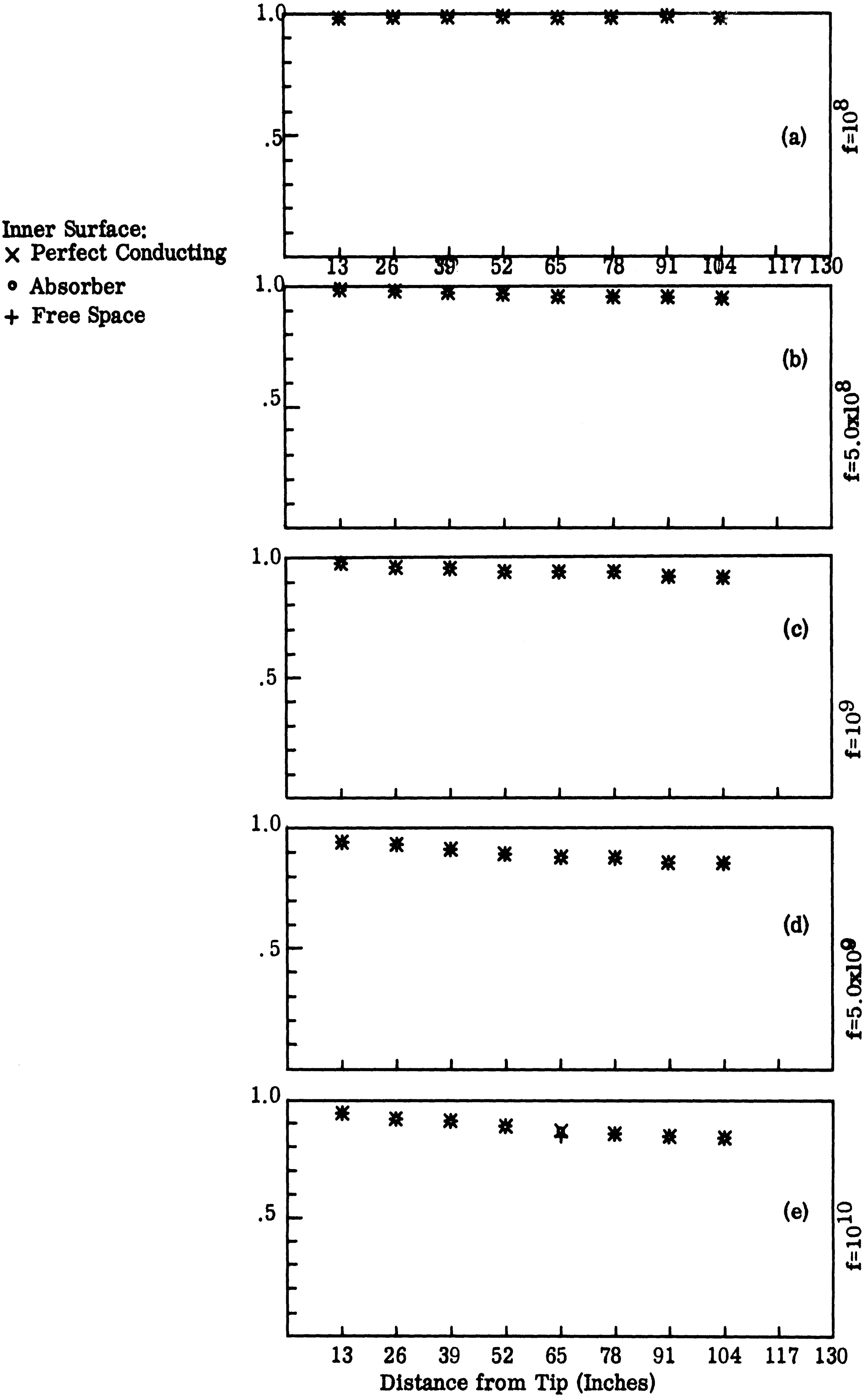

FIG. 3-27 (a-e): $|R_\perp|$ FOR PROFILE 4 (θ=79°).

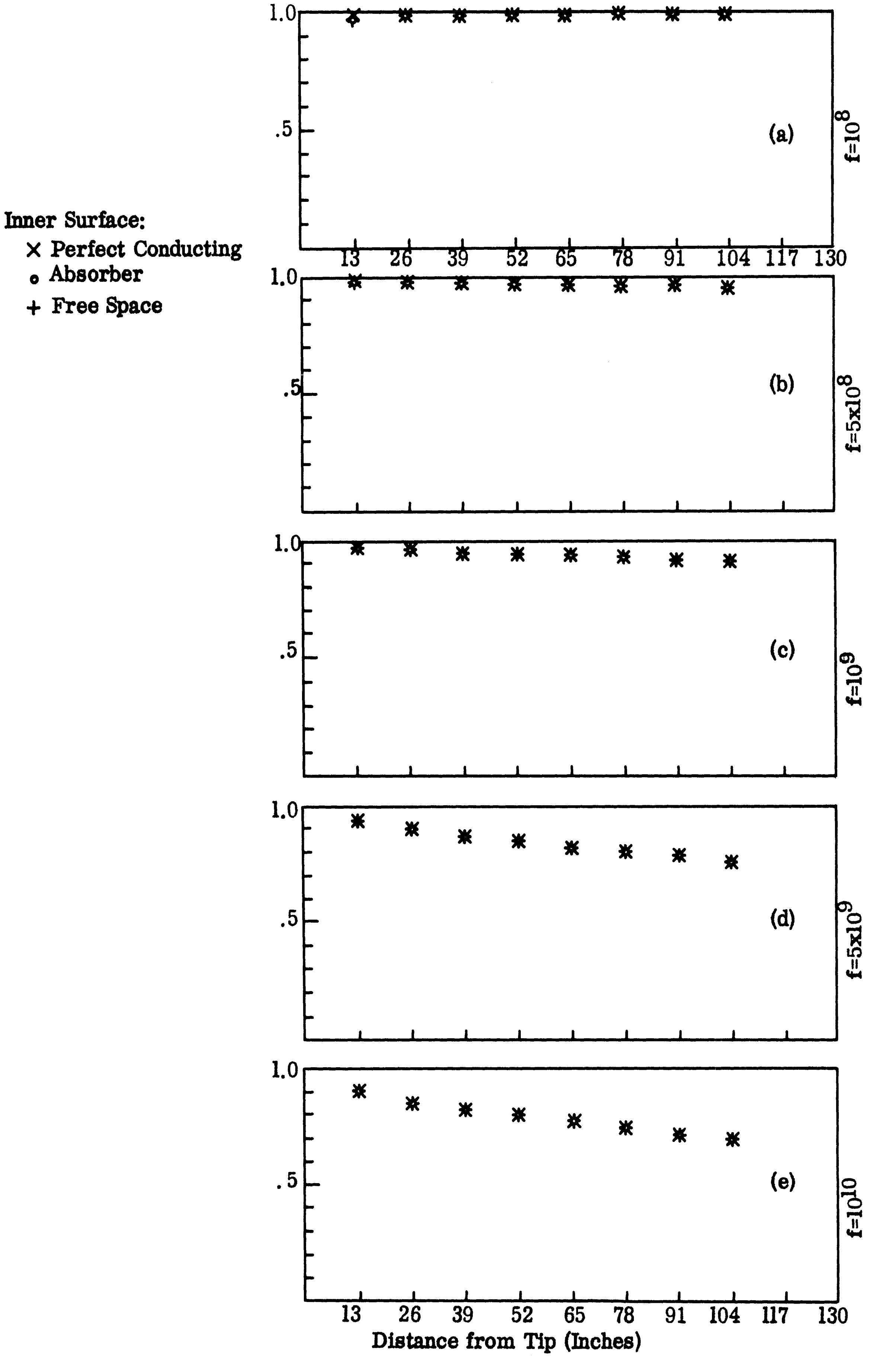

FIG. 3-28 (a-e): $|R|$ FOR PROFILE 5 (θ=79°).

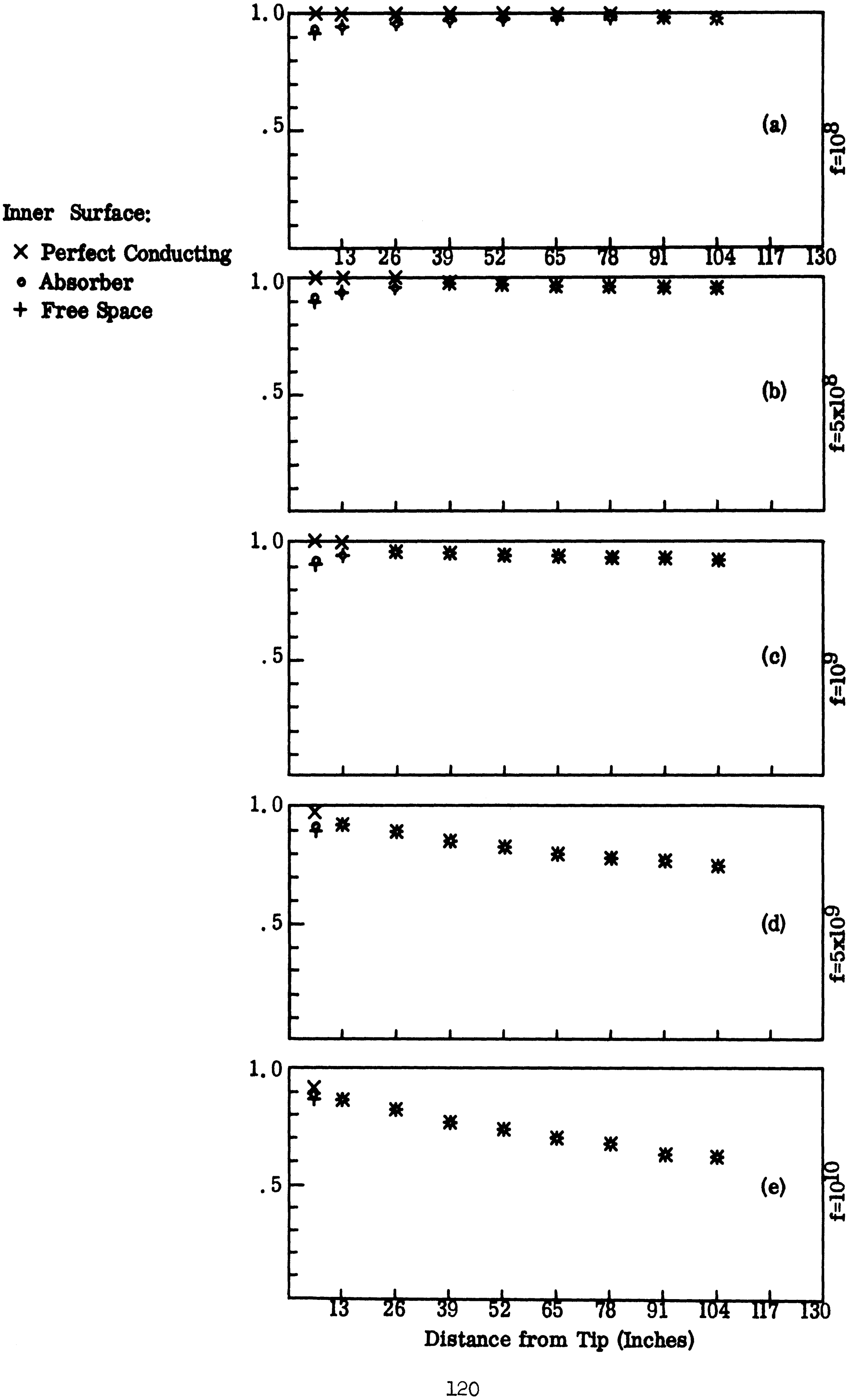

FIG. 3-29 (a-e): $|R_{\perp}|$ FOR PROFILE 6 ($\theta=79^{\circ}$).

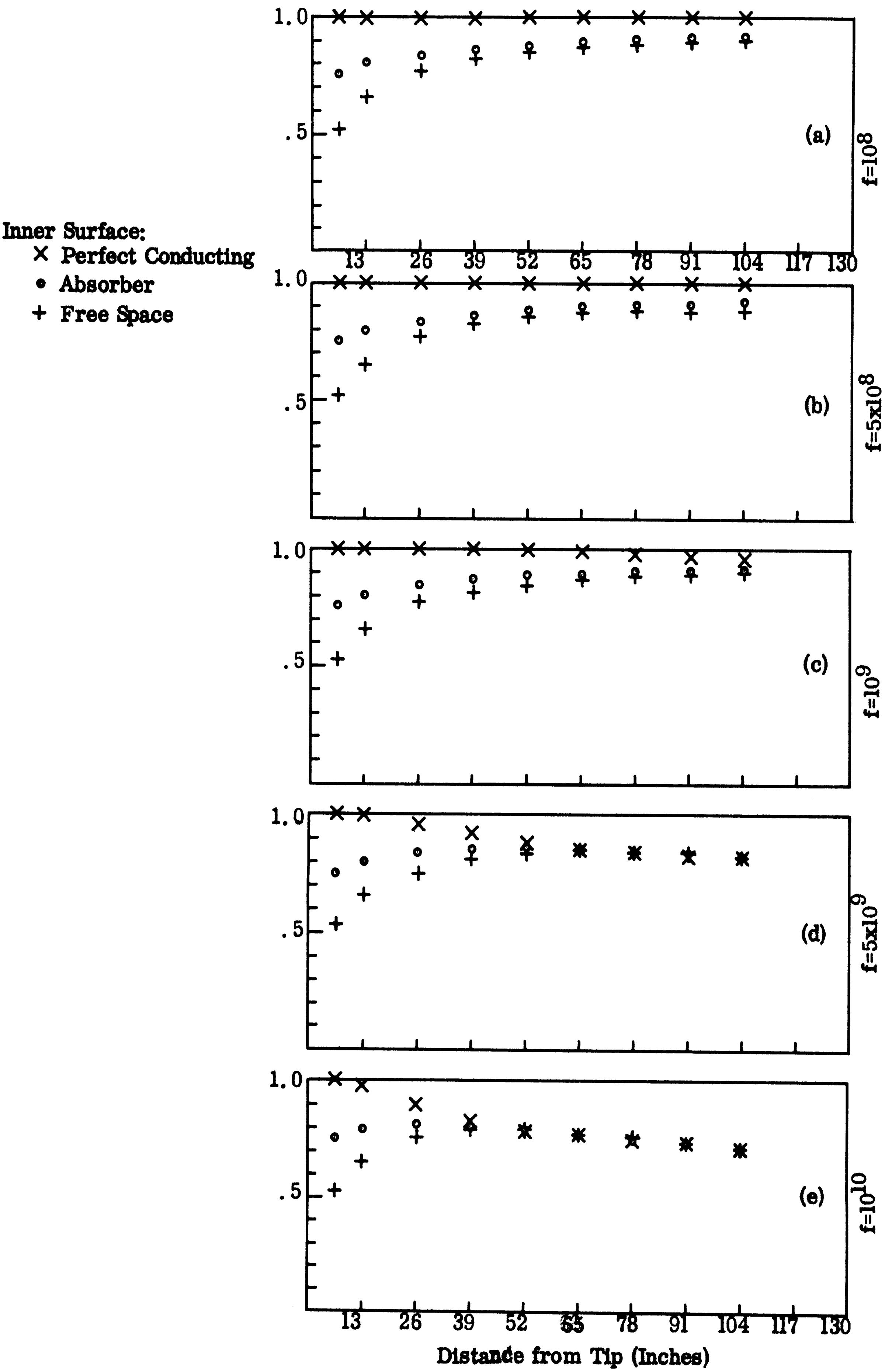

FIG. 3-30 (a-e): | $R_\perp$ | FOR PROFILE 7 (θ=79°).

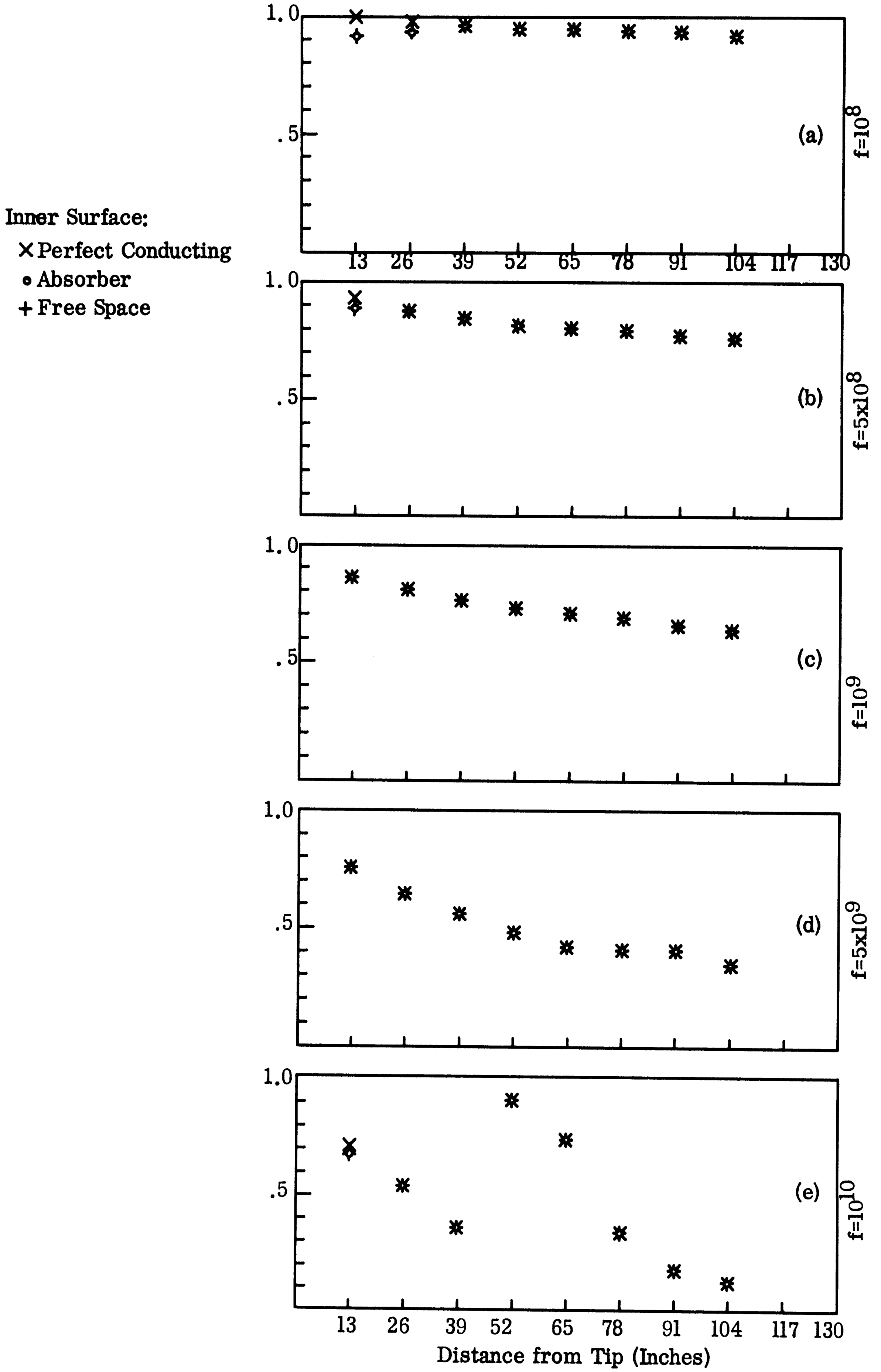

FIG. 3-31 (a-e): $|R_\perp|$ FOR PROFILE 4 (θ=0°).

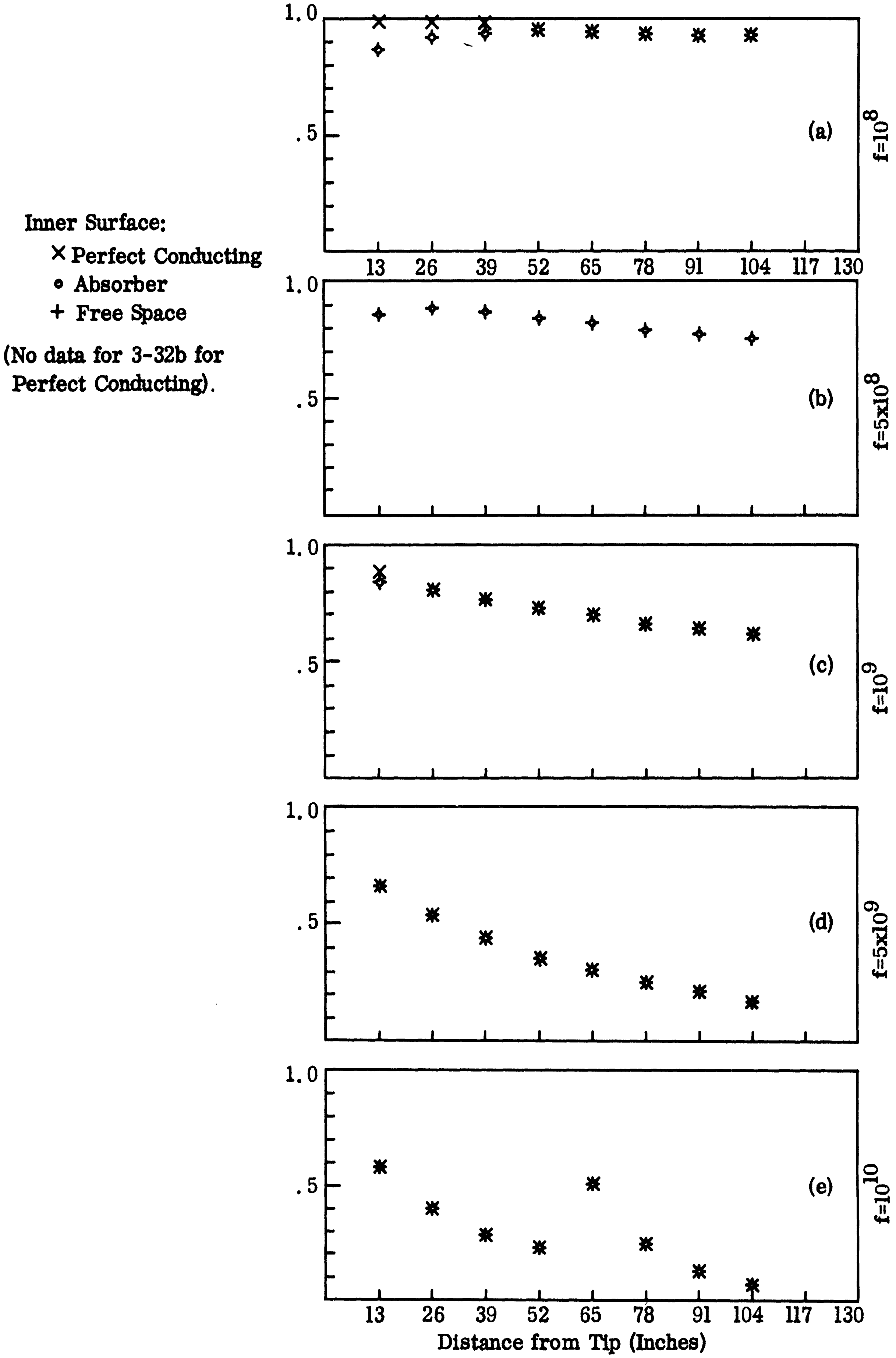

(No data for 3-32b for Perfect Conducting).

FIG. 3-32 (a-e): $|R_\perp|$ FOR PROFILE 5 ($\theta=0^\circ$).

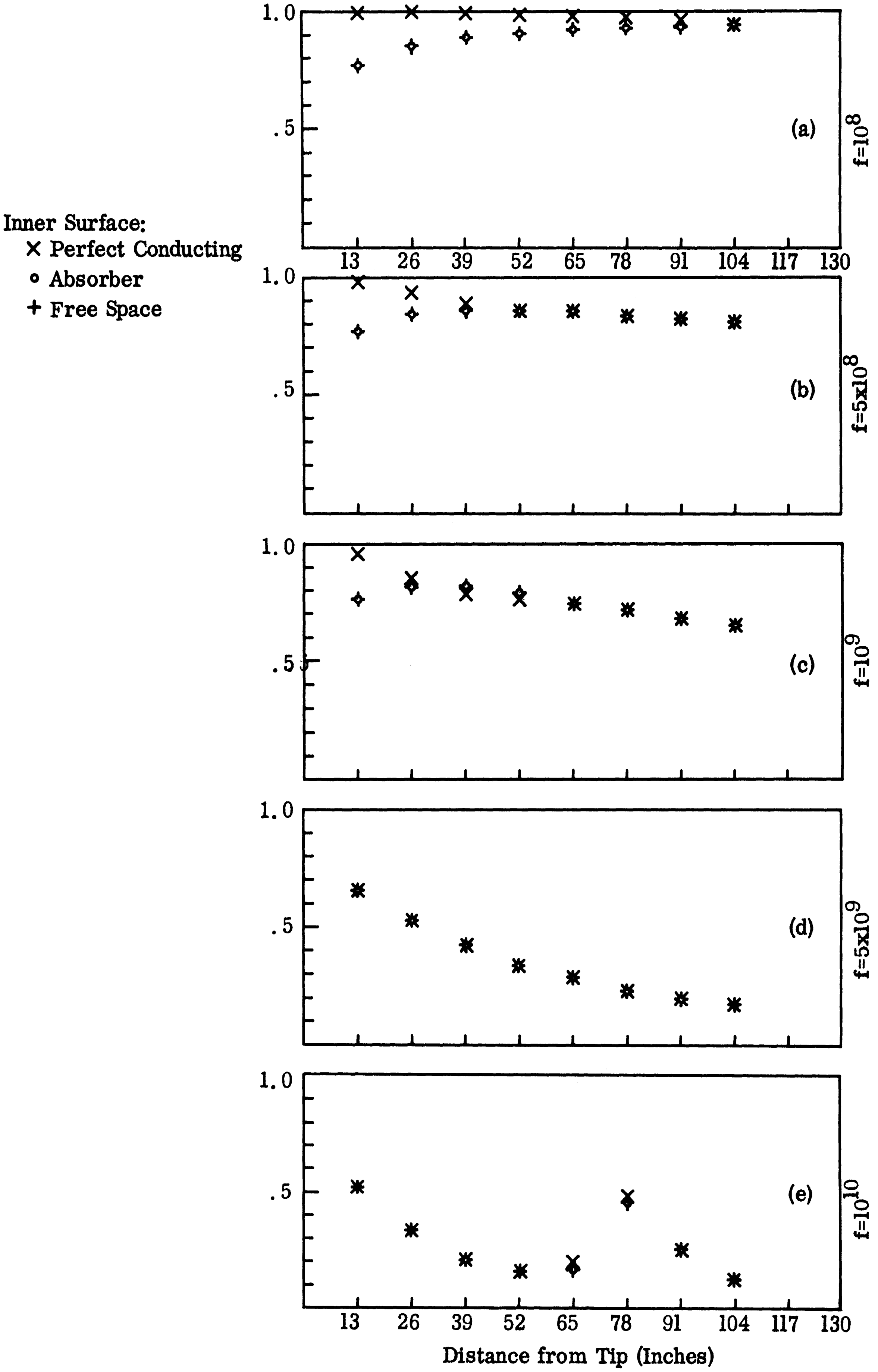

FIG. 3-33 (a-e): $|R_\perp|$ FOR PROFILE 6 ($\theta=0^\circ$)

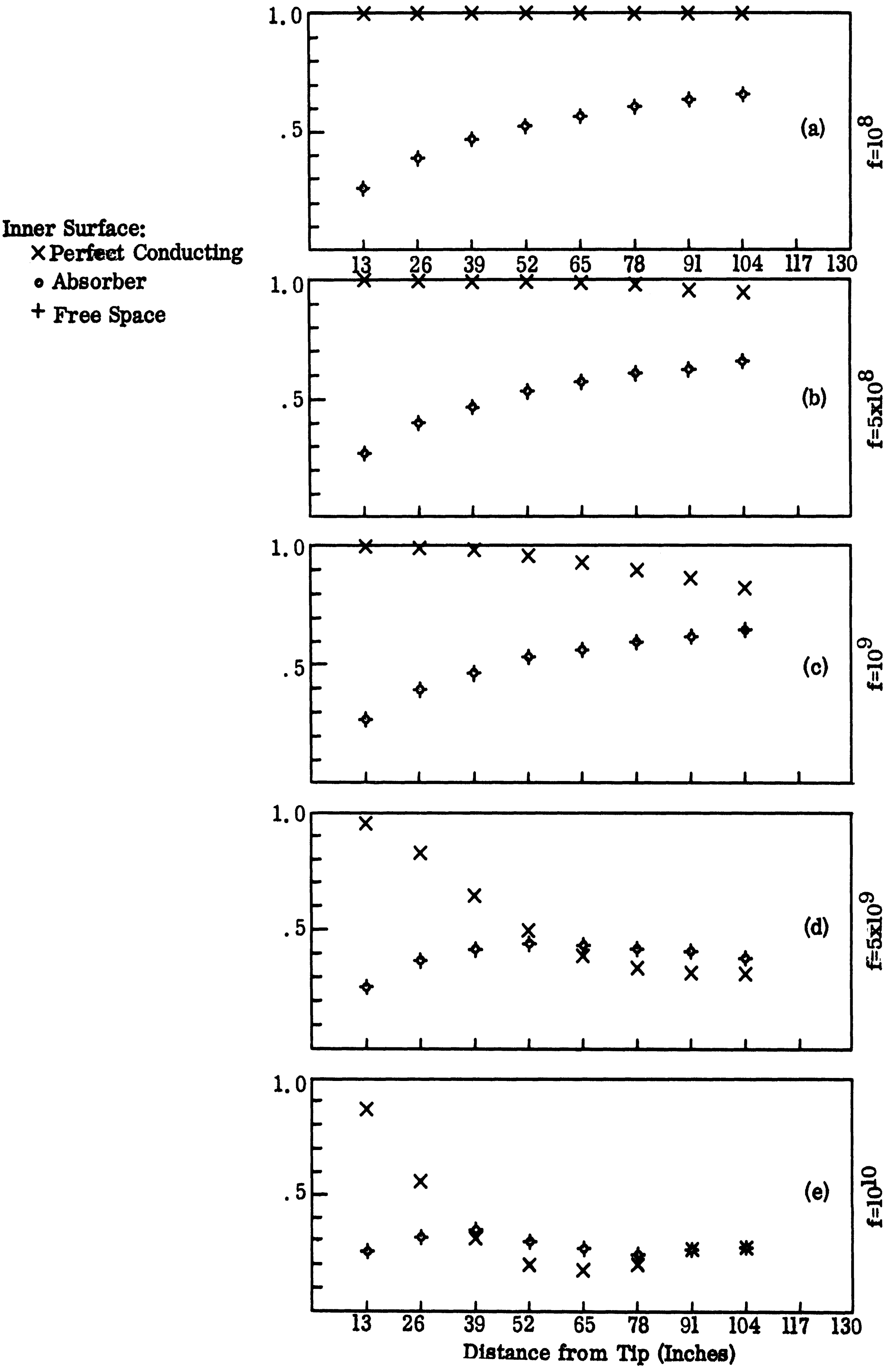

FIG. 3-34 (a-e): $|R_\perp|$ FOR PROFILE 7 ($\theta=0^\circ$).

the sheath shields the portion of the body beyond roughly 39", from the tip at an operating frequency of 10 GHz but this effect decreases with decrease in frequency.

For broadside incidence ($\theta = 0$) the remaining figures indicate the general trend that the magnitude of R decreases with increasing frequency and decreases with increasing distance from the tip. An exception to this occurs at 10 GHz where a resonance appears in Figs. 3-31(e), 3-32(e) and 3-33(e) corresponding to Profiles 4, 5, and 6. Apart from the latter cases, the general trend is expected since the sheath is collision dominated and behaves like a gradient dielectric absorber.

At the present time, calculations are being carried out for the reflection coefficient R corresponding to the other polarization. When these are obtained, the appropriate cross-sections will be calculated.

In the technique presently being employed to obtain an estimate of the cross-section, the principal of local analysis and the tangent plane approximation is used. Future efforts will be devoted to considering more accurate techniques. As a prelude, it is worthwhile to consider whether "ray tracing" can be used for oblique incidence in which case the variation of the properties of the sheath along the surfaces can appreciably effect results.

Thus, we will consider a plane wave incident upon a slab whose electrical properties vary in the direction across the slab only.

The local slab geometry is given in Fig. 3-35, with the yz plane being the plane of incidence, and the angle of incidence given by θ. The sheath is contained in the slab z=0 and z=-h.

When the radiation is polarized perpendicular to the plane of incidence, the electric intensity in the sheath is given by (see the Second Quarterly),

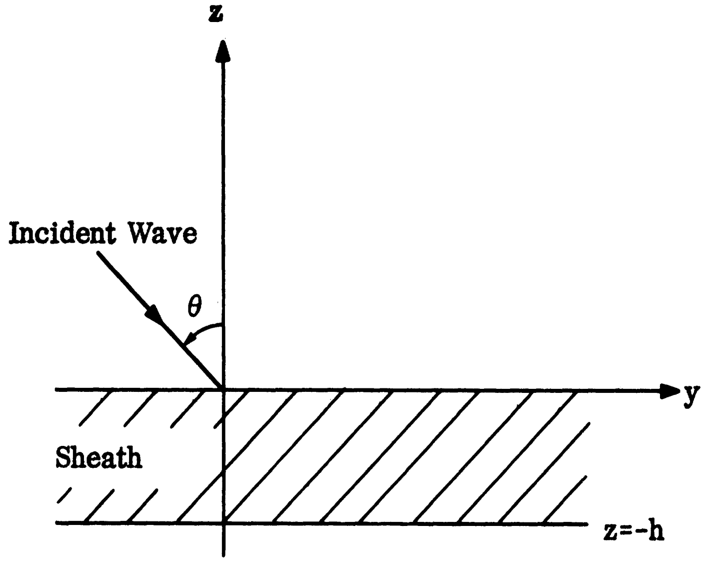

FIG. 3-35: SLAB GEOMETRY.

$$\underline{E} = \hat{\underline{i}}_x \; u(z) \, e^{iky \sin\theta} \tag{3.43}$$

where u(z) is the appropriate solution of the equation

$$\frac{d^2u}{dz^2} + k^2 \left(\epsilon(z) - \sin^2\theta \right) u = 0 \; , \tag{3.44}$$

with $\epsilon(z)$ being the relative dielectric constant of the sheath. For the other polarization, the magnetic field is given by

$$\underline{H} = \hat{\underline{i}}_x \; v(z)\, e^{iky\sin\theta} \tag{3.45}$$

where

$$\frac{d^2v}{dz^2} - \frac{d\epsilon}{\epsilon\, dz}\frac{dv}{dz} + k^2\left(\epsilon(z) - \sin^2\theta\right) v = 0 \; . \tag{3.46}$$

Setting $\phi^2(z) = k^2\left(\epsilon(z) - \sin^2\theta\right)$, (3.47)

$$u(z) = \phi^{-1/2}\, U(\zeta) \quad , \tag{3.48}$$

and

$$\zeta = \int^{z} \phi(z)\, dz \quad , \tag{3.49}$$

Eq. (3.44) can be transformed into the following equation

$$\frac{d^2U}{d\zeta^2} + U(1 + \chi) = 0 \tag{3.50}$$

where

$$\chi = \frac{1}{\phi^2}\left[-\frac{1}{2}\frac{\phi''}{\phi} + \frac{3}{4}\left(\frac{\phi'}{\phi}\right)^2\right] \tag{3.51}$$

and the prime indicates differentiation with respect to z. When $|\chi| \ll 1$, Eq. (3.50) has the approximate solution

$$U \sim \exp \pm i\zeta \tag{3.52}$$

Thus, provided that the following inequality holds

$$|\chi| \ll 1 , \tag{3.53}$$

$$u(z) \sim \left[\epsilon(z) - \sin^2\theta\right]^{-1/4} \exp\left\{\pm ik \int_z^0 \left(\epsilon(z) - \sin^2\theta\right)^{1/2} dz\right\} . \tag{3.54}$$

If the sheath is sufficiently lossy so that a negligible amount of energy reaches the interior surface $z = -h$, the solution in the sheath region can then be characterized by just the wave travelling in the negative z direction, given by the upper sign in expression (3.54). In this case, the reflection coefficient $R_\perp$ is given by (see Task 3.1.7 in the Second Quarterly)

$$R_\perp \simeq \frac{-\epsilon'(0)}{i8k\cos^3\theta + \epsilon'(0)} \tag{3.55}$$

provided that $\epsilon(0) \simeq 1$.

A similar treatment holds for the other polarization. In this case, Eq. (3.46) is reduced to the following

$$\frac{d^2V}{d\zeta^2} + V\left[1 + \tilde{\chi}\right] = 0 \tag{3.56}$$

using the relation

$$v(z) = \epsilon^{1/2}(z)\, \phi^{-1/2}\, V(\zeta) \tag{3.57}$$

together with Eqs. (3.47) and (3.49). The remainder $\tilde{\chi}$ is given by

$$\tilde{\chi} = \chi + \frac{1}{\phi^2}\left[\frac{1}{2}\frac{\epsilon''}{\epsilon} - \frac{3}{4}\left(\frac{\epsilon'}{\epsilon}\right)^2\right] \quad . \tag{3.58}$$

Thus, when $|\tilde{\chi}| \ll 1$, Eq. (3.56) has the approximate solution

$$V \sim \exp(\pm i \zeta) \quad , \tag{3.59}$$

in which case

$$v(z) = \left[\frac{\epsilon^2(z)}{\epsilon(z) - \sin^2\theta}\right]^{1/4} \exp\left\{\pm ik \int_z^0 \left(\epsilon(z) - \sin^2\theta\right)^{1/2} dz\right\} \tag{3.60}$$

Proceeding as before, the reflection coefficient for this polarization is given by

$$R_{\parallel} \sim \frac{-\epsilon'(0)\left[1 - 2\cos^2\theta\right]}{i\,8k\cos^3\theta + \epsilon'(0)\left[1 - 2\cos^2\theta\right]} \quad . \tag{3.61}$$

However, in order for the above results to hold, it is necessary to investigate the conditions $|\chi| \ll 1$ and $|\tilde{\chi}| \ll 1$. The relative permittivity of the outer portion of the sheath corresponding to Profiles 4, 5, 6, and 7 can be approximated by the form

$$\epsilon(z) = 1 + (-\omega + i\nu)\, A\, e^{-bz} \tag{3.62}$$

where A and b are real positive numbers, ω and ν are the operating frequency (radians per second) and collision frequency. In this case, expression (3.51) can be placed in the form

$$\chi = \frac{b^2(1-\epsilon)}{4k^2(\epsilon - \sin^2\theta)^2}\left[1 + \frac{5}{4}\,\frac{(1-\epsilon)}{(\epsilon - \sin^2\theta)}\right] \tag{3.63}$$

To consider the conditions for which $|\chi| \ll 1$, it is important to consider the factor

$$f = \left|\frac{b^2(1-\epsilon)}{4k^2(\epsilon - \sin^2\theta)^2}\right| \tag{3.64}$$

which vanishes at $z = \pm\infty$, and has a maximum at a particular value of z. It can be shown that this maximum occurs at $z = z_0$ given by

$$\cos^2\theta = A(\omega^2 + \nu^2)^{1/2} \exp(-bz_0) \quad . \tag{3.65}$$

Thus, the maximum value of f is given by

$$\frac{b^2}{8k^2\cos^2\theta}\left[1 - \frac{\omega}{\sqrt{\omega^2 + \nu^2}}\right]^{-1} \quad . \tag{3.66}$$

At $z = z_0$, the remaining factor in (3.63) reduces to

$$-\frac{1}{4} + \frac{5}{4}\sqrt{\omega^2 + \nu^2}\left[\sqrt{\omega^2 + \nu^2} - \omega + i\nu\right]^{-1} \quad . \tag{3.67}$$

Combining this with expression (3.66), it is seen that

$$|\chi| \sim \frac{b^2}{8k^2\cos^2\theta} \qquad \nu >> \omega \tag{3.68}$$

$$\sim \frac{5b^2}{8k^2\cos^2\theta} \qquad \nu \quad \omega \tag{3.69}$$

$$\sim \frac{5}{64}\frac{b^2}{k^2\cos^2\theta}\left(\frac{\omega}{\nu}\right)^3 \qquad \omega >> \nu \tag{3.70}$$

The collision frequencies for the sheaths corresponding to Profiles 4, 5, 6, and 7 are 1.9×10^{10}, 4.7×10^{10}, 1.16×10^{11} and 3.5×10^{11}, respectively. The latter two profiles are collision dominated over the frequencies of interest, whereas $\nu \sim \omega$ for Profile 5 at 10^{10} Hz, and $\omega > \nu$ for Profile 4 at 10^{10} and 5×10^9 Hz. The value of b decreases with increasing distance from the tip of the cone since the sheath becomes thicker. In units of cm.$^{-1}$, b is approximately 1 for Profiles 4, 5, and 6, and 4 for Profile 7 at a distance of 104" from the tip. Of particular interest is the nose-on case, for which $\theta \sim 79^{\circ}$. The factor $(k\cos\theta)^{-1}$ then becomes approximately λ. It is easily seen that with the values of λ ranging from 3 cm. to 3 m., and the values of b given above, that $|\chi|$ will be greater or equal to unity. Thus for nose-on incidence to the plasma coated cone, the concept of "ray-tracing" cannot be used.

REFERENCES

Chen, K. M. and V. V. Liepa (1964), "The Minimization of the Back Scattering of a Cylinder by Central Loading," *IEEE Trans.*, *AP-12*, 576-582

Fock, V. A. (1946), "The Distribution of Currents Induced by a Plane Wave on the Surface of a Conductor," *J. Physics, USSR*, *10*, 130-136.

Harrison, C. W. Jr. (1962), "On The Receiving Characteristics of a Dipole in Proximity to Two Intersecting Conducting Surfaces," *IRE Trans.*, *AP-10*, 543-547.

Harrison, C. W. Jr. and R. O. Heinz (1963), "On the Radar Cross Section of Rods, Tubes, and Strips of Finite Conductivity," *IEEE Trans.*, *AP-11*, 459-468.

Hong, S. (1966), "Asymptotic Theory of Diffraction by Smooth Convex Surfaces of Nonconstant Curvature," The University of Michigan Radiation Laboratory Technical Report 7741-2-T. UNCLASSIFIED

King, R. W. P. (1956), *The Theory of Linear Antennas*, Harvard University Press.

King, R. W. P. and T. T. Wu (1956), "Currents, Charges and Near Fields of Cylindrical Antennas," *Radio Science*, *69D*, 429-446.

Kleinman, R. E. and T. B. A. Senior (1963), "Studies in Radar Cross Sections XLVIII: Diffraction and Scattering by Regular Bodies-II: The Cone," The University of Michigan Radiation Laboratory Report 3648-2-T, AD 407557 UNCLASSIFIED

Mack, C. L. and B. Reiffen (1964), "RF Characteristics of Thin Dipoles," *Proc. IEEE*, *52*, 533-542.

Senior, T. B. A. (1966), "Physical Optics Applied to Cone-Sphere-Like Objects," (unpublished notes).

Tai, C. T. (1952), "Electromagnetic Backscattering from Cylindrical Wires," *J. Appl. Phys.* *23*, 909-916

Ufimtsev, P. Ya. (1962), "Diffraction of Plane Electromagnetic Waves by a Thin Cylindrical Conductor," *Radiotekhnikai, Electronika*, *7*, 241-249.

Vainshtein, L. A. (1959), "Waves of Current in a Thin Cylindrical Conductor," *Soviet Phys., Tech. Phys.*, *4*, 601-615 and 616-626.

Van Vleck, J. H., F. Bloch and M. Hamermesh (1947), "Theory of Radar Reflection from Wires or Thin Metallic Strips," *J. Appl. Phys.*, *18*, 274-294.

Zukowski, L. P. and T. B. A. Senior (1965), "Surface Field Data for Cone-Sphere-Like Objects," The University of Michigan Radiation Laboratory Technical Report 7030-6-T. UNCLASSIFIED.

DOCUMENT CONTROL DATA - R&D

(Security classification of title, body of abstract and indexing annotation must be entered when the overall report is classified)

1. ORIGINATING ACTIVITY *(Corporate author)* The University of Michigan Radiation Laboratory Department of Electrical Engineering Ann Arbor, Michigan 48108	2a. REPORT SECURITY CLASSIFICATION SECRET 2b. GROUP 4

3. REPORT TITLE
Investigation of Re-entry Vehicle Surface Fields (U)

4. DESCRIPTIVE NOTES *(Type of report and inclusive dates)*
Quarterly Report No. 3 18 June - 18 September 1966

5. AUTHOR(S) *(Last name, first name, initial)*
Goodrich, Raymond F., Harrison, Burton A., Knott, Eugene F., Senior, Thomas B. A., and Weston, Vaughan H.

6. REPORT DATE September 1966	7a. TOTAL NO. OF PAGES 133	7b. NO. OF REFS 15

8a. CONTRACT OR GRANT NO. AF 04(694)-834	9a. ORIGINATOR'S REPORT NUMBER(S) 7741-3-Q
b. PROJECT NO.	
c.	9b. OTHER REPORT NO(S) *(Any other numbers that may be assigned this report)*
d.	BSD-TR-66-355

10. AVAILABILITY/LIMITATION NOTICES In addition to security requirements which apply to this document and must be met, this document is subject to special export controls and each transmission to foreign governments or foreign nationals may be made only with prior approval of BSD(BSYDF), Norton AFB, Calif. 92409.

11. SUPPLEMENTARY NOTES	12. SPONSORING MILITARY ACTIVITY Ballistic Systems Division Deputy for Ballistic Missile Re-entry Systems AFSC, Norton AFB, California 92409

13. ABSTRACT

(Secret)

This is the Third Quarterly Report on Contract AF04(694)834 and covers the period 18 June to 18 September 1966. Progress on the SURF program is discussed. This program has as its objective the determination of the radar cross section of cone-sphere shaped re-entry vehicles by means of a study of the fields induced on the surface of vehicle models by incident radar energy. During this reporting period, surface field measurements were made on metallic cone-spheres, cone-spheres covered with various coating materials and perturbed cone-sphere shapes. The perturbations included a study of the effect of a nose-tip antenna, a concave rear termination similar to the Mark 12 re-entry vehicle and by representations of flush mounted slot antennas. Radar backscattering measurements were made of models with the nose-tip antenna and the concave termination. The investigation of the radar cross section of the re-entry vehicle in the plasma environment concentrated on determining which cases would be of practical importance so that they might be analyzed in depth. (S)

DD FORM 1 JAN 64 1473

14. KEY WORDS	LINK A		LINK B		LINK C	
	ROLE	WT	ROLE	WT	ROLE	WT
Radar Cross Sections Re-entry Vehicles Cone-Sphere Shapes Coated and Metallic Bodies Flush Mounted Slot Antennas Surface Field Measurements Backscatter Measurements Theoretical Analysis						

INSTRUCTIONS

1. ORIGINATING ACTIVITY: Enter the name and address of the contractor, subcontractor, grantee, Department of Defense activity or other organization *(corporate author)* issuing the report.

2*a*. REPORT SECURITY CLASSIFICATION: Enter the overall security classification of the report. Indicate whether "Restricted Data" is included. Marking is to be in accordance with appropriate security regulations.

2*b*. GROUP: Automatic downgrading is specified in DoD Directive 5200.10 and Armed Forces Industrial Manual. Enter the group number. Also, when applicable, show that optional markings have been used for Group 3 and Group 4 as authorized.

3. REPORT TITLE: Enter the complete report title in all capital letters. Titles in all cases should be unclassified. If a meaningful title cannot be selected without classification, show title classification in all capitals in parenthesis immediately following the title.

4. DESCRIPTIVE NOTES: If appropriate, enter the type of report, e.g., interim, progress, summary, annual, or final. Give the inclusive dates when a specific reporting period is covered.

5. AUTHOR(S): Enter the name(s) of author(s) as shown on or in the report. Enter last name, first name, middle initial. If military, show rank and branch of service. The name of the principal author is an absolute minimum requirement.

6. REPORT DATE: Enter the date of the report as day, month, year; or month, year. If more than one date appears on the report, use date of publication.

7*a*. TOTAL NUMBER OF PAGES: The total page count should follow normal pagination procedures, i.e., enter the number of pages containing information.

7*b*. NUMBER OF REFERENCES: Enter the total number of references cited in the report.

8*a*. CONTRACT OR GRANT NUMBER: If appropriate, enter the applicable number of the contract or grant under which the report was written.

8*b*, 8*c*, & 8*d*. PROJECT NUMBER: Enter the appropriate military department identification, such as project number, subproject number, system numbers, task number, etc.

9*a*. ORIGINATOR'S REPORT NUMBER(S): Enter the official report number by which the document will be identified and controlled by the originating activity. This number must be unique to this report.

9*b*. OTHER REPORT NUMBER(S): If the report has been assigned any other report numbers *(either by the originator or by the sponsor)*, also enter this number(s).

10. AVAILABILITY/LIMITATION NOTICES: Enter any limitations on further dissemination of the report, other than those imposed by security classification, using standard statements such as:

(1) "Qualified requesters may obtain copies of this report from DDC."

(2) "Foreign announcement and dissemination of this report by DDC is not authorized."

(3) "U. S. Government agencies may obtain copies of this report directly from DDC. Other qualified DDC users shall request through

____ ."

(4) "U. S. military agencies may obtain copies of this report directly from DDC. Other qualified users shall request through

____ ."

(5) "All distribution of this report is controlled. Qualified DDC users shall request through

____ ."

If the report has been furnished to the Office of Technical Services, Department of Commerce, for sale to the public, indicate this fact and enter the price, if known.

11. SUPPLEMENTARY NOTES: Use for additional explanatory notes.

12. SPONSORING MILITARY ACTIVITY: Enter the name of the departmental project office or laboratory sponsoring *(paying for)* the research and development. Include address.

13. ABSTRACT: Enter an abstract giving a brief and factual summary of the document indicative of the report, even though it may also appear elsewhere in the body of the technical report. If additional space is required, a continuation sheet shall be attached.

It is highly desirable that the abstract of classified reports be unclassified. Each paragraph of the abstract shall end with an indication of the military security classification of the information in the paragraph, represented as *(TS)*, *(S)*, *(C)*, or *(U)*.

There is no limitation on the length of the abstract. However, the suggested length is from 150 to 225 words.

14. KEY WORDS: Key words are technically meaningful terms or short phrases that characterize a report and may be used as index entries for cataloging the report. Key words must be selected so that no security classification is required. Identifiers, such as equipment model designation, trade name, military project code name, geographic location, may be used as key words but will be followed by an indication of technical context. The assignment of links, rules, and weights is optional.

07741 QUARTERLY DISTRIBUTION LIST

	No of Copies
Aerospace Corporation Attn: H. J. Katzman , Building 537, Room 1007 P. O. Box 1308 San Bernardino, California 92402	10
Air Force Cambridge Research Laboratories Attn: R. Mack CRDG Laurence G. Hanscom Field Bedford, Massachusetts 01731	2
Advanced Research Projects Agency Attn: W. VanZeeland The Pentagon Washington, D. C. 20301	2
Air Force Avionics Laboratory Attn: Wm. F. Bahret AVWE-2 Wright-Patterson AFB, Ohio 45433	1
Ballistic Systems Division Attn: Major Aharonian BSYDF Norton AFB, California 92409	2
Director of Defense Research and Engineering (Strategic Weapons) Attn: Dr. Richard Montgomery The Pentagon Washington, D. C. 20301	1
Institute for Defense Analyses Attn: Dr. Nils Muench 1666 Connecticut Avenue, NW Washington, D. C. 20009	1
MIT-Lincoln Laboratory Attn: Lincoln Laboratory Representative P. O. Box 4188 Norton AFB, California 92409	1

(continued)

07741 QUARTERLY DISTRIBUTION LIST
(continued)

MIT-Lincoln Laboratory Attn: BMRS Project Office P. O. Box 73 Lexington, Massachusetts 02173	3
Special Projects Office Bureau of Weapons Attn: Cmdr. A. Julian Washington, D. C. 20360	3
P. C. Waterman MITRE Corporation Room E 161 Bedford, Massachusetts 01730	1
Defense Documentation Center Cameron Station Alexandria, Virginia 23314	20 + cards
Total	47